Shulman, Jan Edward

ELUCIDATION OF LIQUID FORCE FIELDS IN METHYL FLUORIDE BY MEANS OF VAPOR PRESSURE ISOTOPE EFFECTS

City University of New York PH.D. 1982

ELUCIDATION OF LIQUID FORCE FIELDS IN METHYL FLUORIDE BY MEANS OF VAPOR PRESSURE ISOTOPE EFFECTS

by

JAN SHULMAN

A dissertation submitted to the Graduate Faculty in Chemistry in partial fulfillment of the requirements for the degree of Doctor of Philosophy, The City University of New York.

1981

This manuscript has been read and accepted for the Graduate Faculty in Engineering in satisfaction of the dissertation requirement for the degree of Doctor of Philosophy.

Dec. 21, 1981
date

Chairman of Examining Committee

21 December 1981
date

David C. Locke
Executive Officer

Supervisory Committee

The City University of New York

Abstract

ELUCIDATION OF LIQUID FORCE FIELDS
IN METHYL FLUORIDE BY MEANS OF
VAPOR PRESSURE ISOTOPE EFFECTS

BY

JAN E. SHULMAN

Advisor: Professor Takanobu Ishida

The vapor pressure isotope effects (VPIE) of the three isotopic methyl fluorides: $^{12}CH_3F$, $^{13}CH_3F$, and $^{12}CD_3F$, were studied using differential manometry and a precision cryostat. Absolute pressures were measured using a spiral quartz gauge, and differential pressures were obtained by use of capacitance gauges. The gases were purified to better than 99.995% by preparative gas chromatography and a gas-solid adsorption system. Vapor pressures were measured between 132.52°K and 213.12°K which correspond to the pressures of 3.712 and 1887.1 torr.

Analysis of the vapor pressure data revealed an inverse isotope effect ($\ln(f_c/f_g)<0$) for the $^{12}CH_3F/^{13}CH_3F$ isotopic pairs and a normal effect ($\ln(f_c/f_g)>0$) for the $^{12}CH_3F/^{12}CD_3F$ isotopic pairs. A series of calculations using Wilson's FG-matrix method and a modified Schachtschneider-Snyder program resulted in a temperature-dependent internal-external interaction in the condensed phase: A strongly temperature-dependent internal-external interaction between the C-F

stretching motion and a translational motion in the direction of its figure axis is necessary to explain the observed isotopic vapor pressures.

ACKNOWLEDGEMENT

I wish to extend my sincerest gratitude to:

* Professor T. Ishida for his outstanding patience and guidance during my thesis research.

* Professors V. Fried, L. Massa, and A. Ronn for their help and assistance as thesis committee members.

* Professor D. Locke for his guidance during my association with the Graduate School of C.U.N.Y.

* Dr. A. Popowicz for his construction of the cryostat and friendship.

* Mr. M. Prencipe for all his help in reconstructing our laboratory at Stony Brook and friendship.

* Dr. T. Oi for all his time spent working on the cryostat.

* Mr. Ottmar Safferling for his construction and repair of the glass vacuum systems used in this study and friendship.

* The graduate and undergraduate students of Professor T. Ishida for their assistance and friendship.

* Dr. C. Iden for the work on his mass spectrometry equipment.

* The computer squad at Brooklyn College; Janet, Barry, and Mark, for their help in completing my theoretical work and calculations.

* My wife, Ilene, whose patience, love, and devotion has kept me going strong for five years and enabled me to achieve all my goals and ambitions.

TABLE OF CONTENTS

LIST OF TABLES

LIST OF FIGURES

I. INTRODUCTION

The study of vapor pressure isotope effects (VPIE) has revealed a great deal of information relating to molecular structure, intermolecular forces, and molecular motions in the condensed phase. Continued exploration of these effects will enhance our understanding of the liquid state. The goal of this research is to apply the method of VPIE study and existing spectroscopic and thermodynamic data towards elucidation of the liquid force field of methyl fluoride (CH_3F).

The most precise technique for measuring VPIE is the use of differential manometry. In this study, a spiral quartz gauge (SQG) was used to measure the absolute pressure in the range 0 - 1500 torr with a resolution of ±0.001%. The difference in the vapor pressures of isotopically substituted molecules were obtained using a capacitance gauge. The gauge used is capable of measuring pressure differences with a precision of $\pm 10^{-5}$ torr at its most sensitive scale. The strong dependence of the vapor pressure upon temperature necessitates a very high level of thermal stability for sample specimen. This was accomplished by means of a BBIR[1]-type cryostat, the design of which has recently been modified.[2] This cryostat has a temperature stability which

is better than 10^{-3}°K.

The modified BBIR cryostat has a sample holder with four separate ports capable of holding four different isotopic samples. The sample holder cylinder is composed of 99.9999% copper to assure high thermal conductivity and uniformity. The use of efficient, low temperature heat switches allows for independent cooling of the sample container. The regulated radiation shield will diminish heat loss from the thermal shield around the sample holder to the liquid nitrogen cooled surface of the container wall. These features, as well as several other additional components (which will be discussed in Chapter III), enable the cryostat to attain the high degree of temperature stability. The isotopic samples; $^{12}CH_3F$, $^{13}CH_3F$, and $^{12}CD_3F$ were introduced into the cryostat through high-vacuum service lines constructed of Type 316 stainless steel.

Isotopically enriched (^{13}C) methyl fluoride was synthesized from methanol, tosyl chloride, and potassium fluoride in a two-step reaction. The enriched (^{13}C) methanol was purchased from Prochem, Ltd., as was the deuterated compound ($^{12}CD_3F$). Natural abundance methyl fluoride was supplied by Linde.

Differential manometry requires samples of high chemical and isotopic purity. Therefore, the samples were purified to better than 99.995% by bulb-to-bulb distillation and successive passes through columns of silica gel, ascarite and chromosorb. Isotopic purities for the three species; $^{12}CH_3F$, $^{13}CH_3F$, and $^{12}CD_3F$, were analyzed using mass spectrometry and calculated to be 98.5%,

83.3%, and 97.4%, respectively.

After the samples were loaded into the sample holder ports, the condensed gases were allowed to attain thermal equilibrium. Platinum resistance thermometers (PRT) and thermocouples (TC) are located at pivotal positions inside the cryostat to monitor the temperature stability as well as the absolute temperature. The pressure of $^{12}CH_3F$ was measured on the SQG, and the differential pressures of $^{13}CH_3F$ and $^{12}CD_3F$, each relative to $^{12}CH_3F$, were measured on the capacitance gauges. At the same time, the temperature of the sample holder was measured using a high precision PRT located in the center of the sample holder block. The measurements have been carried out between 132.52°K (P = 3.712 torr) and 213.12°K (P = 1887.1 torr).

The experimental vapor pressures are directly related to the ratio of the reduced partition function ratios, f_c/f_g, where "c" and "g" are the condensed and gaseous phases, respectively. Using a best force constant matrix ($\underset{\sim}{F}$-matrix) constructed for the gaseous molecule, the reduced partition function ratio for the gas, f_g, was calculated, and the "experimental" reduced partition function ratio for the condensed phase, f_c, was subsequently obtained from the experimental f_c/f_g and the calculated f_g. The gaseous $\underset{\sim}{F}$-matrix was obtained by an improvement of the matrix published by Aldous and Mills.[3] Only a limited amount of spectroscopic information was found relating to the condensed phase of methyl fluoride: Chao and Eggers[4] on natural abundance and deuterated CH_3F and Griffiths[5] on $^{12}CH_3F$. A tentative $\underset{\sim}{F}$-matrix

was set up based upon the best $\underset{\sim}{F}$-matrix of the gas, and the corresponding values of reduced partition function ratio of the liquid was calculated at several temperatures and the results compared to the experimental values of f_c. A series of adjustments in the liquid $\underset{\sim}{F}$-matrix were made until the magnitudes of the calculated and experimental f_c coincided fairly well. The refinement of the calculated liquid $\underset{\sim}{F}$-matrix was also constrained by the requirement that it had to reproduce experimental frequencies within a reasonable range and use interaction force constants constrained to feasible, physical limits.

The most significant aspect of the theoretical study was the implementation of temperature-dependent internal-external force constants which was found essential for reproduction of the experimental VPIE data. The arguments leading up to this conclusion will be discussed in detail. The possibility of molecular association in the condensed phase will also be reviewed.

In Chapter II, the theory of VPIE and its application to a variety of molecular systems will be reviewed. The experimental apparatus for purification and analysis of the gases, as well as the cryostat and its sub-assemblies, will be discussed in Chapter III. Experimental procedures will be described in Chapter IV, and results, including data reduction, will be presented in Chapter V. Chapter VI will discuss the significance of the experimental results obtained, Chapter VII will briefly summarize the facts elucidated by this study, and Chapter VIII will list recommendations for future studies on methyl fluoride.

II. REVIEW OF THEORY AND PRACTICE OF VAPOR PRESSURE ISOTOPE EFFECT

IIA. VPIE Theory

The equilibrium established between molecules in the liquid and vapor phases directly determines the vapor pressure of a chemical species. At constant temperature, the equilibrium state is characterized by a unique gas-phase pressure. By exchanging the isotopic species, a shift is observed in the vapor pressure. This effect is referred to as the vapor pressure isotope effect (VPIE). Use of VPIE measurements offer a means of examining intermolecular forces and molecular motions in the condensed phase.

Upon transition from the gas to the condensed state, two major effects must be considered. The first is due to the perturbation of the internal energy levels by intermolecular forces. Individual vibrational energy levels may be raised or lowered in comparison to the gas phase values although the total zero-point energy of the molecule is lowered upon condensation.[6] The second effect originates from the external motions of the molecule. In the gas phase, the molecule is considered to be "free", and exhibits no rotational or translational motions. As the molecule

condenses, the molecular motion becomes more or less hindered and confined in an attractive potential well. The six external modes for the condensed phase are shifted to higher, non-zero values (blue-shifted). The intramolecular motions can shift towards the red or blue, and the net result of the two major effects can be either positive or negative. A positive effect leads to the lighter isotopic species having the higher vapor pressure; and hence a normal VPIE. When the heavier isotope possesses the higher vapor pressure, an inverse VPIE is witnessed.

In 1961, Bigeleisen[7] formulated a fundamental theory of VPIE, and its simplest form, based on the simple cell model of liquid, was first applied to deuteroethylenes by Stern, Van Hook, and Wolfsberg.[6] The simple cell model assumes that each molecule is encased in an isotropic and time-independent potential cage as a result of interactions with its nearest neighbors. The expression for VPIE as presented by Bigeleisen was:

$$\ln\left(\frac{P'}{P}\right) = \ln\left(\frac{s}{s'}\right) f_c - \ln\left(\frac{s}{s'}\right) f_g + (RT)^{-1}(P'V'-PV)_c$$
$$-(B_o P+\tfrac{1}{2}C_o P^2)'_g+(B_o P+\tfrac{1}{2}C_o P^2)_g-(RT)^{-1}\int_V^{V'} P'dV, \qquad (1)$$

where the primed and unprimed quantities refer to the lighter and heavier isotopic species, respectively, $(s/s')f_c$ and $(s/s')f_g$ are the reduced partition function ratios (RPFR) for the condensed and gas phases, respectively, and B_o and C_o are the second and third virial coefficients of the gas phase. The correction terms originate from the difference between the Gibbs and Helmholtz free

energies and from gas imperfections. The last term, $(RT)^{-1} \int_V^{V'} P'dV$, arises from the difference in the condensed phase molar volumes of the isotopic molecules.

In most cases, $\ln(P'/P)$ is small (on the order of 0.01). Equation (1) can be simplified by assuming $B_o' = B_o$, $V' = V$, and neglecting $(RT)^{-1} \int_V^{V'} P'dV$ and higher order terms such as $C_o P^2$, and rewriting the expression as

$$\ln\left(\frac{f_c}{f_g}\right) = \ln\left(\frac{P'}{P}\right)\left[1+P\left(B_o - \frac{V}{RT}\right)\right] \qquad (2)$$

In this manner, experimental vapor pressure data, $\ln(P'/P)$, can be substituted into Equation (2) to determine the ratio of the reduced partition functions ratios, f_c/f_g.

The reduced partition functions ratio, $(s/s')f$, is defined as[8]

$$\frac{s}{s'} f = \frac{(Q_{qm}/Q_{cl})}{(Q'_{qm}/Q'_{cl})} \qquad (3)$$

where Q_{qm} and Q_{cl} are the quantum mechanical and classical partition functions, respectively. The partition function is considered reduced because it is the partition function relative to its classical limit. Within the guidelines of the Born-Oppenheimer and Harmonic Oscillator approximations, and assuming no vibrational-rotational interactions, the reduced partition function ratio (RPFR) for the N-atomic gas molecule can be expressed as[6,8,9]

$$\frac{s}{s'} f_g = \frac{Q_{vib}}{Q'_{vib\ qm}} \frac{Q_{vib}}{Q'_{vib\ cl}} = \prod_{i=1}^{3N-6} \frac{u_i e^{-u_i/2}(1-e^{-u_i'})}{u_i' e^{-u_i'/2}(1-e^{-u_i})} \qquad (4)$$

where the quantum mechanical vibration partition function is

$$(Q_{vib})_{qm} = \prod_{i=1}^{3N-6} \frac{e^{-u_i/2}}{1-e^{-u_i}}, \qquad (5)$$

the classical vibration partition function is

$$(Q_{vib})_{cl} = \prod_{i=1}^{3N-6} \frac{1}{u_i}, \qquad (6)$$

and $u_i = hc\nu_i/kT$. ν_i is the ith normal frequency in cm^{-1}, h Planck's constant, c the velocity of light, k the Boltzmann constant, and T the absolute temperature. Equation (4) utilizes the assumption that the translational and rotational partition functions are considered classical, and can be treated independently from the internal motions.

In the liquid phase, the 3N-6 vibrational modes were treated in the same fashion as in the gas, with the remaining six external (three translational and three rotational) modes being subject to a harmonic restoring force. The expression for the condensed phase partition function is

$$\frac{s}{s'} f_c = \prod_{i=1}^{3N} \frac{u_i e^{-u_i/2}(1-e^{-u_i'})}{u_i' e^{-u_i'/2}(1-e^{-u_i})}, \qquad (7)$$

and the ratio of the reduced partition function of the gas phase to that of the condensed phase is

$$\frac{f_c}{f_g} = \prod_{\substack{\text{INT.}\\ \text{FREQ.}}}^{3N-6} \left[\frac{(u_i/u_i')_c}{(u_i/u_i')_g}\right] \times \left[\frac{\exp(u_i'-u_i)_c/2}{\exp(u_i'-u_i)_g/2}\right]$$

$$\times \left[\frac{(1-\exp(-u_i')_c)/(1-\exp(-u_i)_c)}{(1-\exp(-u_i')_g)/(1-\exp(-u_i)_g)}\right] \times \tag{8}$$

$$\prod_{\substack{\text{EXT.}\\ \text{FREQ.}}}^{6} \left[\frac{u_i}{u_i'} \exp\left(\frac{u_i'-u_i}{2}\right) \times \frac{1-\exp(-u_i')}{1-\exp(-u_i)}\right]_c$$

The 3N molecular frequencies consist of two distinct groups: the 3N-6 internal frequencies and the six external frequencies. The internal modes have high-frequencies (>500 cm^{-1}), while the external modes have low-frequencies (<150 cm^{-1}). At high temperature, the modes become excited, and each vibrational term in the expressions for the reduced partition function can be usually treated as a first order quantum correction which is proportional to the square of the inverse of the absolute temperature. At low temperature, high frequency vibrations are not excited at all, and consequently contribute to the reduced partition function only through isotopic differences in their zero-point energies.[6] At temperatures at which all molecular vibrations, external as well as internal, can be treated either by the first quantum correction approximation or by the zero-point energy approximation, Equation (8) becomes

$$\ln\left(\frac{P'}{P}\right) \approx \ln\left(\frac{f_c}{f_g}\right) = \frac{A}{T^2} - \frac{B}{T}\ , \tag{9}$$

where, usually,

$$A = \frac{1}{24}\left(\frac{hc}{k}\right)^2 \left[\sum^{EXT.} (\nu_i'^2 - \nu_i^2)\right] \qquad (10)$$

in which only the external and low frequencies are involved, and usually,

$$B = \left(\frac{hc}{2k}\right)\left[\left(\sum^{INT.} \nu'_{i_g} - \sum^{INT.} \nu'_{i_c}\right) - \left(\sum^{INT.} \nu_{i_g} - \sum^{INT.} \nu_{i_c}\right)\right] \qquad (11)$$

in which the summations go only over the internal and high frequencies. The A term is usually associated with the external vibrations only and is always positive. The B term is the contribution due to the isotopic difference in the zero-point energy on condensation, and is usually positive. At sufficiently low temperatures, the A/T^2 term predominates, and the isotope effect is normal ($\ln(P'/P)>0$). As the temperature is increased, the B-term begins to dominate, and an inverse isotope effect ($\ln(P'/P)<0$) may result. The temperature at which $\ln(P'/P)=0$ is called the crossover temperature.

Over the past two decades, most vapor pressure data have been interpreted on the basis of Bigeleisen's theory and the simple cell model for liquids. Studies on the experimental vapor pressure differences have unveiled significant details about molecular structure and intermolecular forces. For instance, large curvatures in the plots of $\ln(P'/P)$ against $1/T$ for the H/D substituted ethanes were interpreted by Van Hook[10] as evidence for stiffening of the hindered rotation of the CH_3 group about the C-C axis upon condensation. Bigeleisen, Cragg, and Jeevanandam[11] found large

differences in the A terms of Eq. (9) for the pair $^{12}CH_4$ - $^{12}CH_3D$ and the A-term for the pair, $^{12}CH_4$ - $^{13}CH_4$, and consequently concluded that the rotation of methane is hindered in the condensed phase. The simple cell model has also revealed cases where specific internal-external interactions in the condensed phase occur. The differences in the zero-point energy shift on condensation for the three isotopic isomers of $C_2H_2D_2$ (cis, trans, and gem) are due to the coupling of the hindered rotation with certain internal vibrations.[6,12-15] The internal frequencies involved in coupling with the rotation have been found to be symmetry dependent. The observed differences in the vapor pressure of the two isotopic isomers of nitrous oxide, $^{15}N\ ^{14}N\ ^{16}O$ and $^{14}N\ ^{15}N\ ^{16}O$, demonstrate that the rotation is hindered in the liquid.[16] An updated study using more precise measurements[17] has revealed that the two non-equivalent isotopic isomers of nitrous oxide also experience hindered translation, coupling of internal angle-bending motions with translation, and anharmonicities in the external and bond-stretching motions.

IIB. Techniques for Measurement of VPIE

Several techniques have been developed to measure the vapor pressure isotope effect. Due to the strong temperature dependence of the vapor pressure, measurements are usually performed simultaneously on both isotopic species.

Distillation studies are generally easy to set up and require

natural abundance samples for experimentation. The chemical purity of the sample being distilled must be on the order of better than 99.9%. The single stage separation factor, α, between a condensed phase and its saturated vapor is given by

$$\alpha = \left(\frac{N'}{N}\right)_{vap} \Big/ \left(\frac{N'}{N}\right)_{liq} \qquad (12)$$

where N' and N are the mole fractions of light and heavy isotopic molecules. The separation factor defined by Eq. (12) is equal to the ratio of RPFRs, f_c/f_g. The single stage separation factor is very close to unity, and the precision of the measurement of α by a single stage distillation is therefore limited by the isotopic analysis. A greater overall separation can be obtained by building a distillation column with n-theoretical plates, which increases the single-stage separation factor n-fold[18] (α^n). However, it is often very difficult to determine the number of theoretical plates. This value depends not only on the properties of the distillation column and the nature of the distillate, but also, and to an even higher extent, upon the column operational characteristics such as the flow rates, the column packing, and the degree of wetting of the packing. Distillation studies are usually characterized by large uncertainties in the experimental data.[19,20] These errors are a result of various problems associated with the temperature control of the distillation column and in measurements of the material holdup. A relatively long period of time (one to two weeks) is required to obtain one data point for the vapor pressure at a given temperature.

In contrast, differential manometry requires the use of highly enriched (90-95%) isotopic compounds with the exceptionally high (99.995%) chemical purity. Vapor pressure measurements must be performed at precisely the same temperature and compared differentially. Different types of oil, mercury, or membrane manometers[21-23] and differential capacitance gauges[24,25] have been used to precisely measure the vapor pressure differences.

A typical vapor pressure difference between isotopic molecules is of the order of one percent:

$$\frac{\delta p}{p} = \frac{p'-p}{p} = 0.01 \ , \qquad (13)$$

where p' and p denote the vapor pressures of the light and heavy isotopic species, respectively. Then, the requirement for temperature stability of a cryostat may be obtained as follows. Suppose that one requires that the above ratio is measured to a precision of one percent. Then, the uncertainty σ for $\delta p/p$ must satisfy the relation,

$$\left[\frac{\sigma(\frac{\delta p}{p})}{(\frac{\delta p}{p})}\right]^2 = \left[\frac{\sigma(\delta p)}{\delta p}\right]^2 + \left[\frac{\sigma(p)}{p}\right]^2 \leq 10^{-4} \qquad (14)$$

The relative uncertainty in the absolute pressure measurement is easily negligible in the real practice compared to the relative uncertainty in the measurements of the difference in vapor pressure due to the small magnitude of the pressure difference δp, so that the requirement becomes

$$\frac{\sigma(\delta p)}{\delta p} \leq 10^{-2} \quad . \tag{15}$$

However,

$$\frac{\sigma(\delta p)}{\delta p} \approx \frac{\delta\sigma(p)}{\delta p} \approx \frac{\sigma(p)}{\delta p} = \frac{\sigma(p)}{p}\frac{p}{\delta p} \quad , \tag{16}$$

and according to the Clausius-Clapeyron equation,

$$\frac{\sigma(p)}{p} = \frac{\Delta H_{vap}}{RT^2}\,\sigma(T) \quad , \tag{17}$$

which is on the order of 0.1 $\sigma(T)$ at 200°K and if ΔH_{vap} = 10 Kcal/mole. Thus, the requirement becomes $\sigma(T) = 10^{-3}$ °K.

In our laboratory a cryostat of a modified BBIR[1] type has been recently built by Popowicz[2] for use at temperatures below 300°K. It achieves the necessary temperature stability with ease, and one is capable of obtaining measurement of isotopic vapor pressure differences at up to fifteen temperatures per day. In the next chapter the construction and specifications of this cryostat will be briefly discussed to allow references from the latter chapters.

III. EXPERIMENTAL APPARATUS

The majority of cryostats built for low temperature thermal measurements are in accordance with the principles of the Nernst calorimeter.[26] Major improvements have been introduced over the years by Giauque[27] and Johnston[28] in an effort to minimize the heat transfer by radiation. Bigeleisen and Roth[29] measured the vapor pressures of pure isotopic species using a modification of the Johnston-type cryostat capable of high thermal stability. In 1968, Bigeleisen, Brooks, Ishida, and Ribnikar (BBIR)[1] introduced a series of improvements on the Bigeleisen-Roth cryostat. The BBIR cryostat design allows for precision measurements of the vapor pressure over a large temperature range (2-300°K) with a high degree of thermal stability ($\sim 10^{-3}$ degrees). The cryostat constructed to study VPIE in methyl fluoride was built by A. Popowicz[2] which incorporated several improvements over the BBIR design. The cryostat assembly, associated vacuum systems, instrumentation for pressure and temperature measurement, and complete controls will be discussed in Section IIIA. Although these equipment were constructed mainly by A. Popowicz, Section IIIA is included here for the sake of providing reference for the later chapters.

Differential vapor pressure measurements require isotopic samples of very high chemical purity (99.995%). The three isotopic

species of methyl fluoride: $^{12}CH_3F$, $^{13}CH_3F$, and $^{12}CD_3F$, had initial purity levels of 99.7%, 97.4%, and 99.4%, respectively. These samples were purified using preparative gas chromatography and a gas-solid adsorption system. The gases were analyzed using a Perkin-Elmer 990 analytical gas chromatograph capable of detecting impurities down to better than the parts per million (ppm) level. The techniques used for purification and analysis are described in Section IIIB.

IIIA. Modified BBIR Cryostat

IIIA-1. Cryostat Assembly

A schematic diagram of the assembled BBIR-type cryostat is shown in Figure 1. Located in the core of this structure is the sample holder (SH), which is illustrated in Figure 2. The SH is a cylinder which has four separate cavities symmetrically positioned. Four independent samples can be condensed into the individual holes of the sample container. The SH is composed of 99.9999% copper for purposes of high thermal conductivity and uniformity between the four sample ports. The lower third of each port is packed with fine platinum mesh to improve thermal contact between the sample and cell walls. The SH is loaded with lead to insure for high heat capacity. The centrally located hole at the bottom of the sample holder houses a high precision platinum resistance thermometer (PRT). At the top of the SH resides a copper-constantan thermocouple (TC),

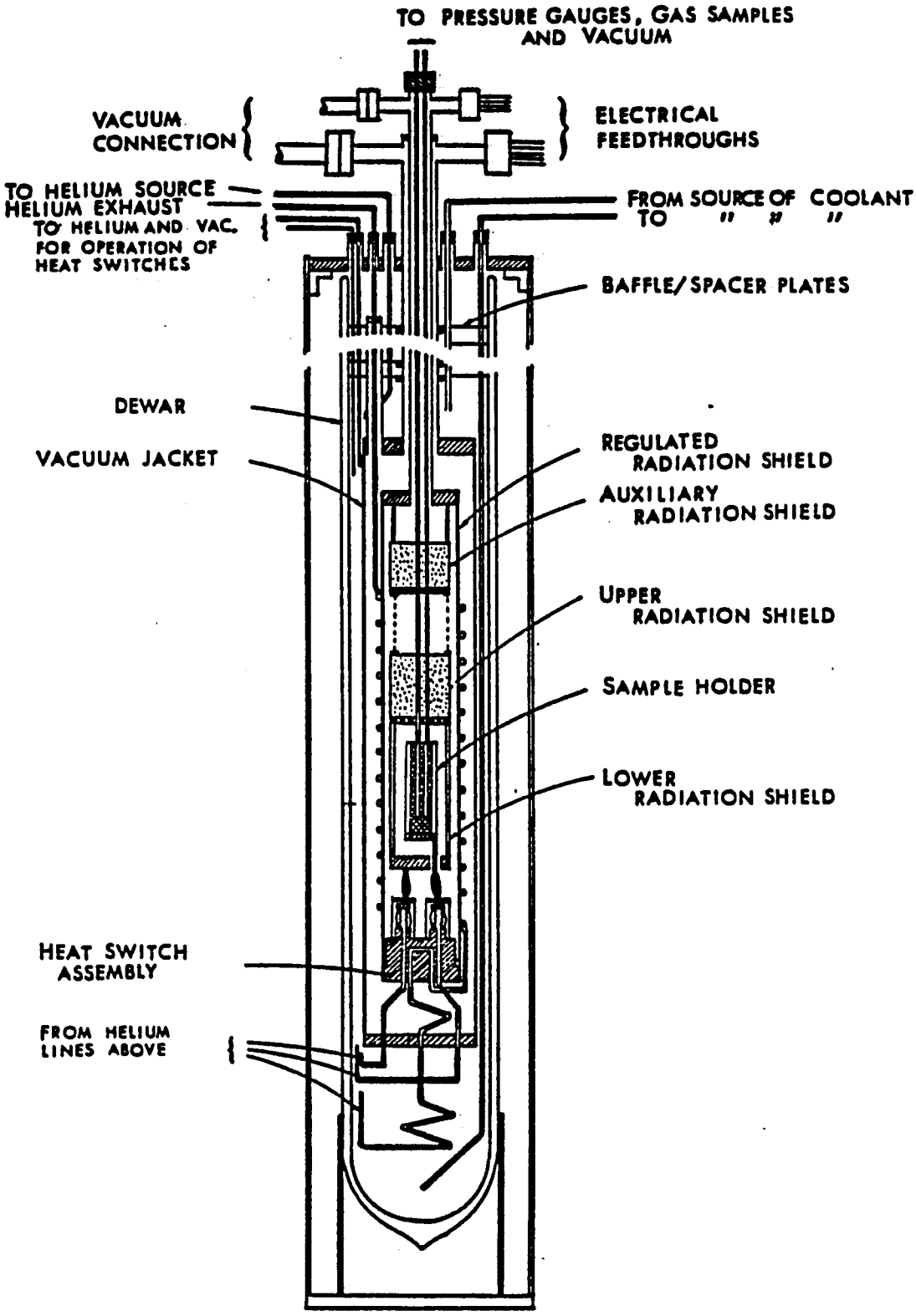

Figure 1. Assembly Drawing of Cryostat

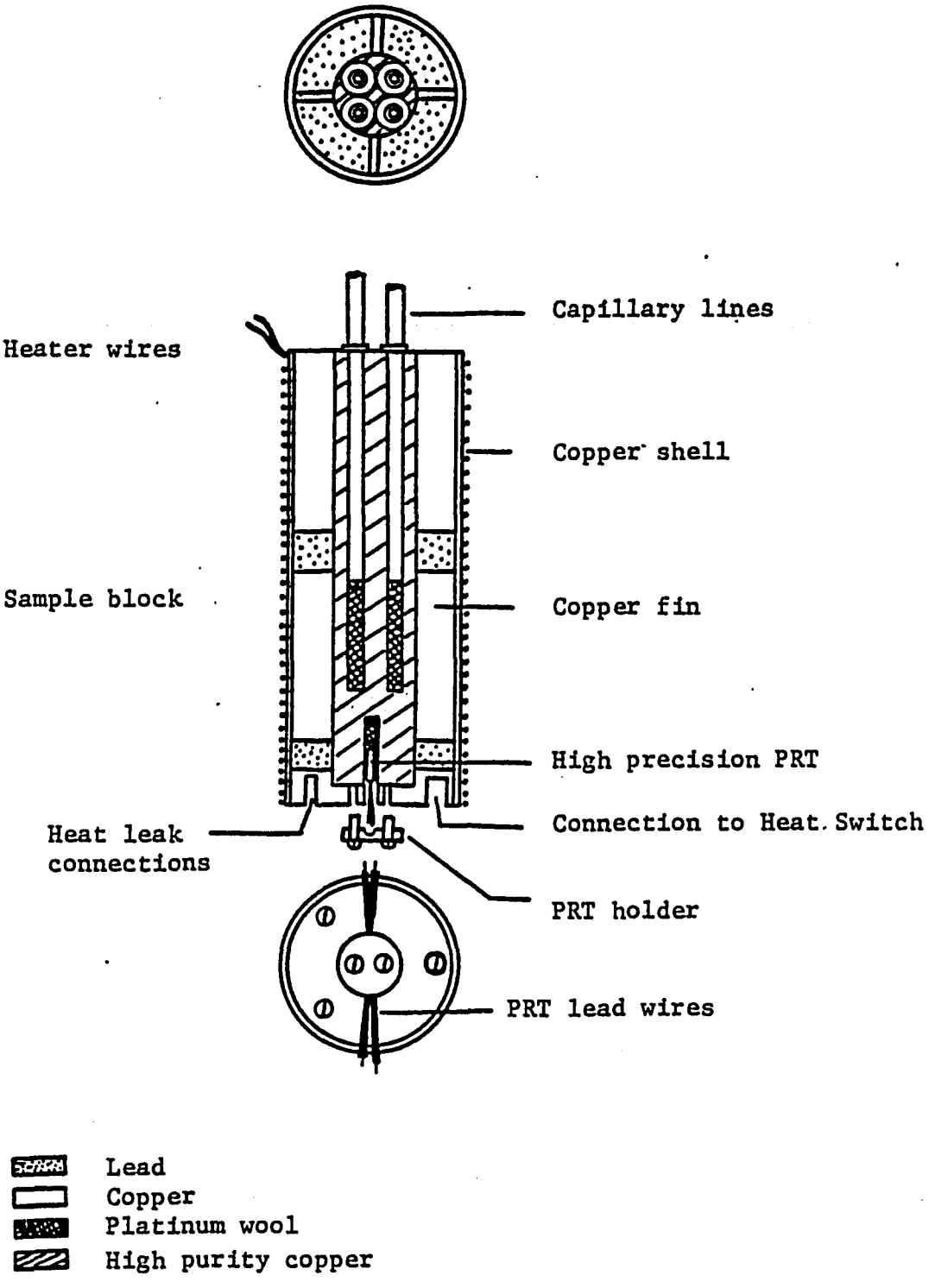

Figure 2. Sample Holder

which is in thermal contact with the copper block. The sample container is wound with constantan wire, which functions as a heater, and the temperature of the SH can be maintained independently of the other subassemblies.

To maintain temperature stability, a series of radiation shields surround the SH. The lower radiation shield (LRS) completely encases the sample holder block. The space between the LRS and the SH is completely evacuated to minimize heat loss by conduction and convection. Directly above the SH and LRS is the upper radiation shield (URS). The upper and lower radiation shields are in good thermal contact with each other, and the URS contributes in minimizing radiation effects from the upper region of the cryostat assembly. Above the URS is the auxiliary radiation shield (ARS). Its function is to minimize thermal radiation effects by acting as a buffer zone between the upper cryostat assemblies on one hand and the SH and surrounding radiation shields on the other. The radiation shields are all made of copper and loaded with lead to insure high heat capacity. Each radiation shield is wound with a constantan wire heater and incorporates a platinum resistance thermometer and a thermocouple.

The cryostat sample holder is connected to the sample inlet system and pressure measuring devices by four capillary lines (CL). Each CL is thin-walled stainless steel tubing which is silver-soldered to one of the sample holes in the SH to allow for transfer of the samples. These lines extend through the entire length of the

cryostat, and are subject to large temperature gradients. Parasitic condensation of the sample in the CL may block the flow into the sample vessel and usually results in longer equilibration times or erroneous measurements.. To prevent this situation, two heaters and two thermocouples were installed on the CL. The first heater is located between the upper and auxiliary shields, and the other lies above the auxiliary shield and immediately below the lowest of the baffle plates.

One of the most important features found in the modified-BBIR cryostat is the use of efficient, low temperature heat switches (Figure 3) which allow for independent cooling of the sample holder and lower radiation shield. The heat switch assembly (HS) is located below the SH and surrounding radiation shields. The HS is cooled by circulating liquid refrigerant through the base of the assembly. The switches are then actuated by pressurizing the bellows with helium gas. The bellows expand and make thermal contact with a plate directly above, which is connected by flexible copper braid to either the SH or the LRS, depending on the particular switch. The HS is used to perform the final phase of cooling after an exchange gas is used for an initial, rapid cool down of the cryostat.

A variable temperature radiation shield, called the regulated radiation shield (RRS), is located between the outside container wall and the radiation shields surrounding the sample container. The outside of the RRS is wrapped with a coil of copper tubing soft-soldered along its entire length. The RRS is equipped with a

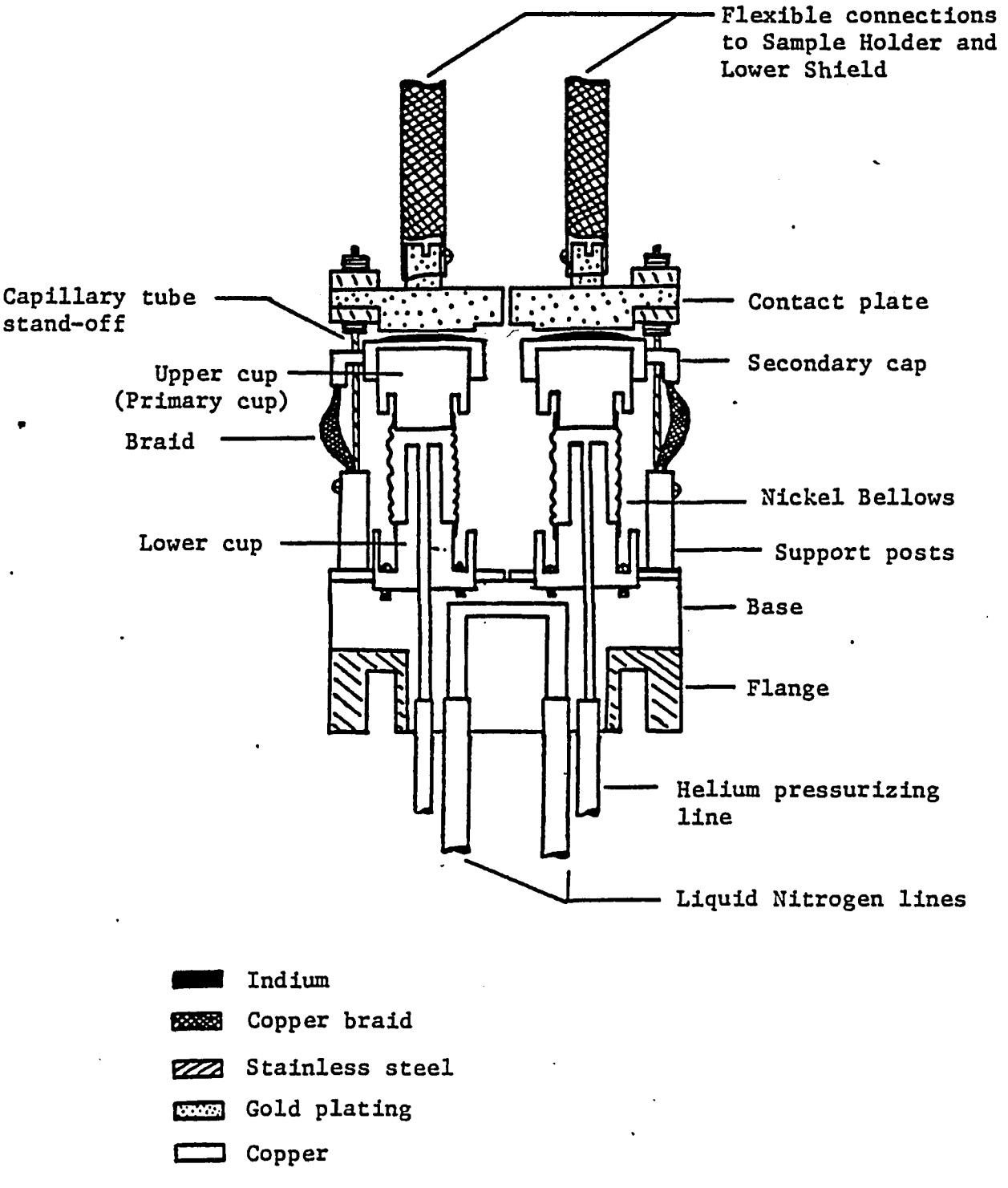

Figure 3. Heat Switch

constantan wire heater, a platinum resistance thermometer and thermocouple. The use of a cooling coil and a heater allow for independent temperature control of the RRS over a diversified temperature range. The temperature stability of the BBIR-cryostat is vastly improved by the addition of this feature into the overall design.[2]

The RRS is encased by another container, the outer can (OC). The space between the OC and RRS is evacuated, as is the area between the RRS and the inner assemblies. The tubings which supply helium gas for pressurizing the heat switch bellows and liquid nitrogen (LN_2) for cooling of the HS-base and the RRS-cooling coil are fed through three vacuum feedthroughs, located at the bottom of the OC. The top of the OC is connected directly to the outer flange, and the pair are sealed by a teflon-coated stainless steel O-ring.

The entire assembly described above is loaded into a stainless steel dewar (Janis Model #RD-2185) capable of cryogenic operation down to liquid helium temperature. For this study, a home-made LN_2 level controller has been installed to achieve a more uniform level of refrigerant in the dewar. Five sensor heads, each consisting of a pair of 1,000 ohm carbon resistors placed 1 1/4" apart vertically, have been installed in the cryostat dewar at key locations. A five-position rotary switch selects the level of refrigerant in the dewar. When the liquid level decreases, the low level sensor initiates filling by activating a three-way solenoid valve and pressurizing the refrigerant-holding tank with nitrogen. The dewar fills until

the high level sensor is activated, the nitrogen supply is cut off, and the holding tank vented to the atmosphere. This automatic operation was used overnight but the LN_2 filling was done manually during the VPIE measurement to achieve a finer control of the LN_2 level.

IIIA-2. Cryostat Vacuum Systems

The cryostat-differential manometry system incorporates three independent vacuum systems during its operation. The sample inlet system (Figure 4) utilizes four independent manifolds for storage and introduction of the isotopic samples into the four sample holder ports. Each manifold is connected to a 1-liter sample storage reservoir and a Wallace-Tiernan differential pressure gauge calibrated from 0-760 torr. The sample inlet system also services the pressure-measurement devices (quartz spiral gauge and differential capacitance gauges). An operating pressure on the order of 10^{-7} torr is maintained by an all stainless-steel, two-inch vacuum pumping station.

A second two inch, oil diffusion pumping station (Cryostat-Dewar System) is used to service the vacuum jacket and various inner vacuum spaces of the cryostat. It also provides an operating pressure on the order of 10^{-6} to 10^{-7} torr. Both vacuum pumping stations are equipped with ionization gauges and ionization gauge controls to monitor the high vacuum. Thermocouple gauges and controls are located in each system for measuring vacuum service

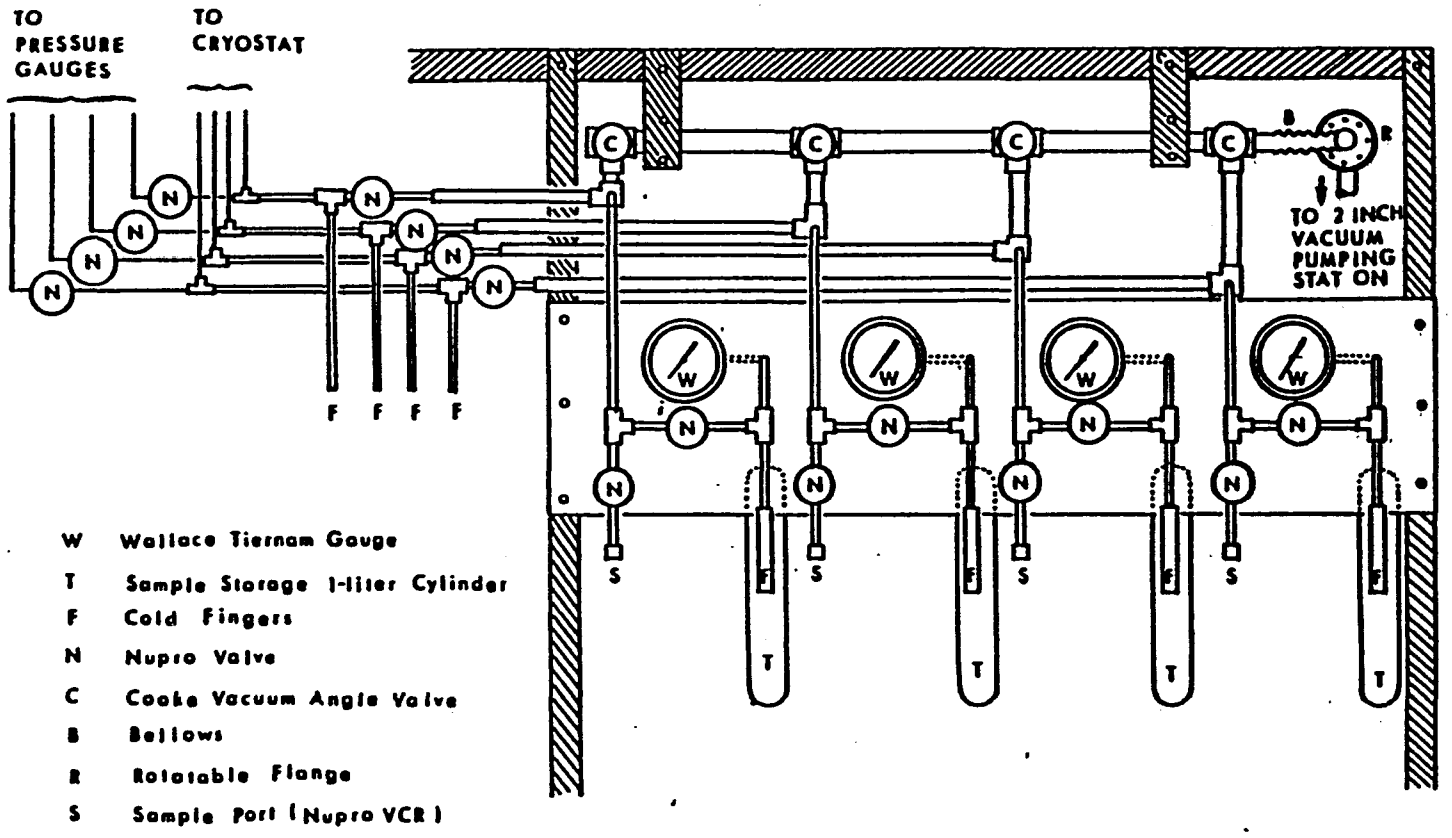

Figure 4. Cryostat Sample-Handling Vacuum Line

line pressures above 10^{-3} torr.

The third system, the service manifold, (Figure 5) is used for several key functions:

1. pressurizing and evacuating the heat switch bellows, for which the cryostat-dewar pumping station is tapped;

2. the introduction and removal of the helium transfer gas used for cryostat cool down;

3. control rate of vaporization of the liquid nitrogen coolant through the regulated radiation shield coil and the heat switch, and

4. siphoning out LN_2 from the cryostat dewar after completion of a series of data points.

For the last two operations, a large-volume air pump is used, and the rate of removal of the LN_2 coolant is controlled by a metering valve connected in line with the air pump. The air pump attains a vacuum on the order 10^{-1} to 10^{-3} torr.

IIIA-3. Temperature and Pressure Measurements

The cryostat supports twelve temperature sensors: seven copper-constantan thermocouples (TC) and five platinum resistance thermometers (PRT). The PRT's utilized have resistance values of approximately 100 ohms at 0°C with calibrations traceable to the National Bureau of Standards. The standard precision (± 0.05%), ceramic encased, PRTs are located in the LRS, URS, ARS, and RRS. The SH houses a high precision (± 0.002%), hermetically sealed PRT (Minco Model #S1059) with a high degree of stability and

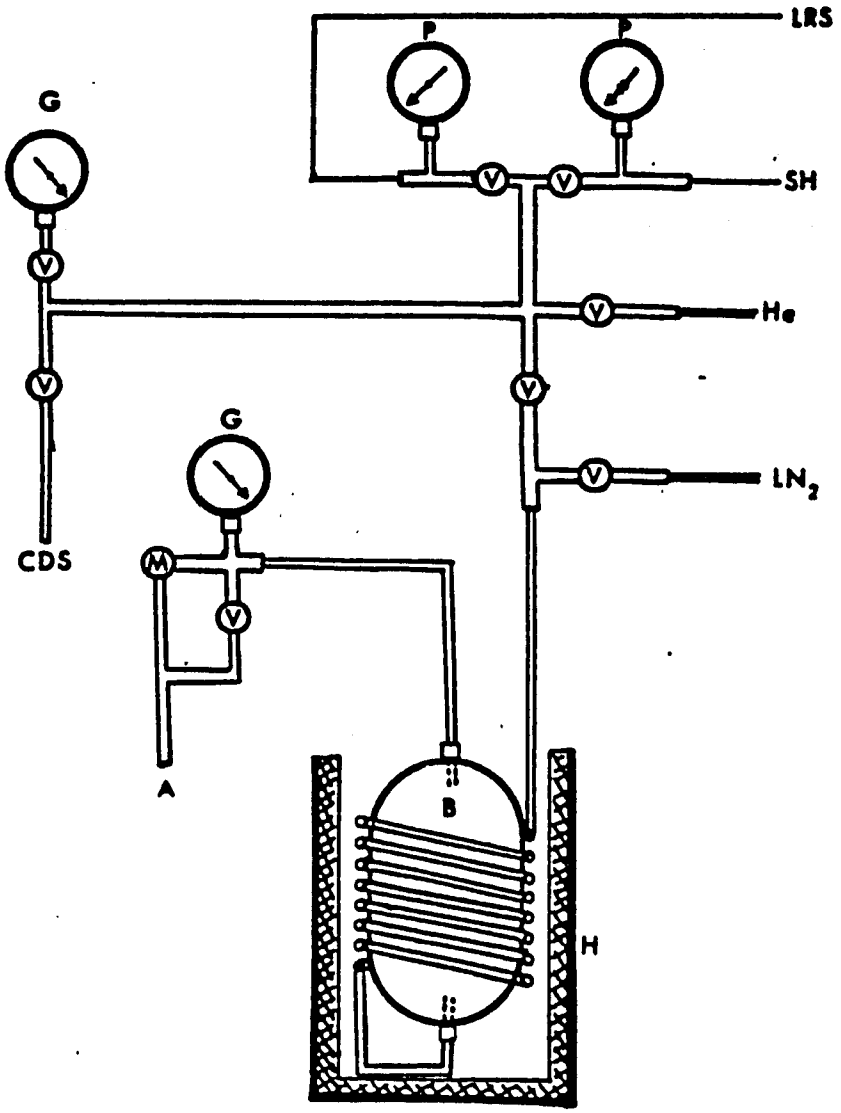

LRS	Lower Radiation Shield-Heat Switch Helium Pressurizing Line
SH	Sample Holder-Heat Switch Helium Pressurizing Line
P	0-30 inch vacuum/0-30 psi pressure gauge
G	0-30 inch vacuum gauge
He	Helium gas inlet
LN_2	Connection to Cryostat Liquid Nitrogen Siphoning Line
V	On/off valve
M	Metering valve
B	Ballast for warming up LN_2 Vapor
H	Heating Mantle
A	Connection to air pump

Figure 5. Service Manifold

repeatability. Each subassembly of the cryostat is equipped with a copper-constantan TC which provides a secondary sensor for temperature measurement. The capillary lines are equipped with two TCs to monitor the temperature and reduce the possibility of parasitic condensation in the leads.

All thermocouples had been calibrated[2] against one of the standard precision PRTs in a specially designed and constructed thermostat.[2] The calibration points had been least-square fitted to a cubic functional form and used for the control of the cryostat during VPIE-measurement runs. The TC voltages were read directly to ± 1 μV (± 0.03°C) on a Non-Linear Systems Model MX-1, and the PRT resistances were measured to ± 1 mΩ (± 0.0025°C) on a Keithley Model 5900 DVOM.

The isotopic vapor pressure differences were measured using a differential manometry system. Absolute pressures are measured using a spiral quartz gauge (SQG), and differential pressures are obtained through the use of differential capacitance gauges (CG).

The SQG (Mensor Corp.) has a range of 0-1500 torr with a readability of ± 0.015 torr. A Ruska Dead Weight Gauge (Model #2460) was used to recalibrate the SQG. The dead weight gauge utilizes standard weights calibrated by the National Bureau of Standards (Job #14662). One hundred and seventy seven points were taken over a pressure range of 0-1499 torr, using atmospheric pressure as a reference. The data was fit to a cubic polynomial of the form:

$$P = aQ^3 + bQ^2 + cQ \qquad (19)$$

where P is the absolute pressure in torr and Q is the SQG decade counter reading (100,000 counts/1500 torr). The values are as follows:

$$a = -1.8052 \times 10^{-14} \pm 3.628 \times 10^{-16}$$

$$b = 1.4810 \times 10^{-9} \pm 4.536 \times 10^{-11}$$

$$c = 1.5243 \times 10^{-2} \pm 1.300 \times 10^{-6}$$

The SQG also provides a direct indication of the temperature stability during vapor pressure measurements. An electronic signal from the SQG is fed to a Fisher recorder to monitor pressure fluctuations as a function of time. These pressure fluctuations can be related to measurable temperature fluctuations, which for the most part are less than one millidegree.

The measurement of differential pressures with respect to the reference sample was accomplished through the use of three Datametrics Capacitance Gauges (Model #572). In this study, the absolute pressure of $^{12}CH_3F$ was measured by the SQG and used as a reference. The capacitance gauges are capable of differential pressure measurements in the 0-100 torr range. They are equipped with zero and full scale calibration controls and an analog output of 0-10 volts DC (± 0.01% precision). Pressure differentials of 10^{-5} torr can be measured on the most sensitive scale.

IIIA-4. Cryostat Control and VPIE Measurement System

A schematic for the cryostat electronics interface scheme

is illustrated in Figure 6. The cryostat measurement/control system can be operated manually, automatically (computer controlled) or by a computer assisted mode. The electronics interface scheme can be subdivided into four sections:

1) temperature sensor interface
2) pressure instrumentation interface
3) heater interface and controls
4) computer controls

The temperature sensor interface scheme is composed of two distinct sections; the thermocouple and platinum resistance thermometer interfaces.

Seven cryostat TCs are accessed to a reference junction maintained at the triple point of water. The sensor lines are connected to a 12 channel thermocouple selection switch and to the first seven channels of a 12 channel 12 bit analog-digital (A/D) converter. The voltage output is read off a Non-Linear Systems MX-1 six digit Digital Volt-Ohm Meter (DVOM). The precision of the thermocouple data obtained from the A/D converter is ± 5 μV (∿± 0.15°C) and the readability obtained manually from the DVOM is ± 1 μV (∿± 0.03°C).

The PRTs are connected to the cryostat terminal board and then to a switching circuit. The resistance thermometers can be selected manually through a Leeds and Northrup low resistance switch or automatically through a system of mercury-wetted reed relays. The PRTs are wired to a Keithley Model 5900 6-digit DVOM to acquire resistance measurements to a precision of ± 0.001 ohm (∿± 0.0025°C). Automatic selection is accomplished by using two D/A converter channels to

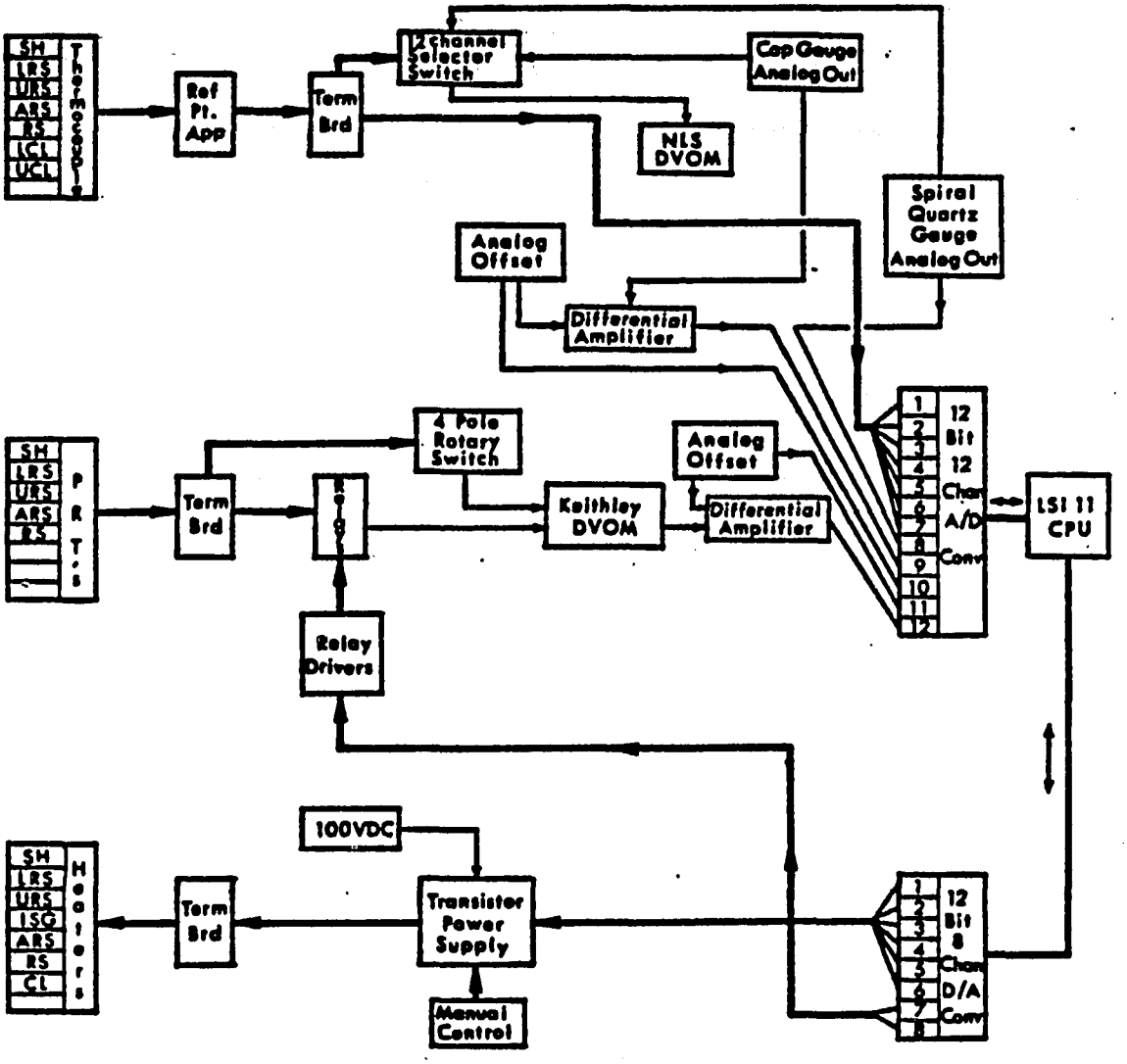

Figure 6. Cryostat Overall Electronics Interface Scheme
(Schematic courtesy Dr. A. Popowicz)

drive a set of relays. PRT precision is on the order of ± 0.025 ohms (∿± 0.0625°C) for a 12 bit conversion.

Vapor pressure data was measured on a spiral quartz gauge and a capacitance gauge system. The output of these instruments was also hardwired to the 12 channel selection switch and to channels 8 and 9 of the A/D converter. The CG signal is fed into a differential amplifier which can be balanced by a known voltage from a calibration source (Datel #DVC 8500 calibration voltage sources). Channel 10 of the A/D converter was used to monitor the voltage output from the Datel voltage source. In the manual mode, the SQG is read directly off the decade counter to ± 1 count or ± 0.015 torr. The SQG can also be read to ± 10 μV (± 0.15 torr) from the Non-Linear Systems DVOM and to ± 25 μV (± 0.375 torr) by the computer through the A/D converter. The CG signal is measurable to ± 0.01% full scale off the DVOM and to ± 0.25% full scale off the computer via the 12 bit A/D converter.

The cryostat utilizes seven constantan wire heaters for independent heating of the subassemblies. A diagram of the cryostat heater circuit[2] is provided in Figure 7. Each heater can be adjusted and controlled manually or by computer control. Automatic operation is achieved by using the output from eight independently controlled digital-analog (D/A) converter channels. Manual operation of the heaters is accomplished by ten-turn potentiometers with a common 5.7 VDC at 10 man power supply.

The cryostat-differential manometry system utilizes an LSI-11 microcomputer to facilitate data acquisition. The computer

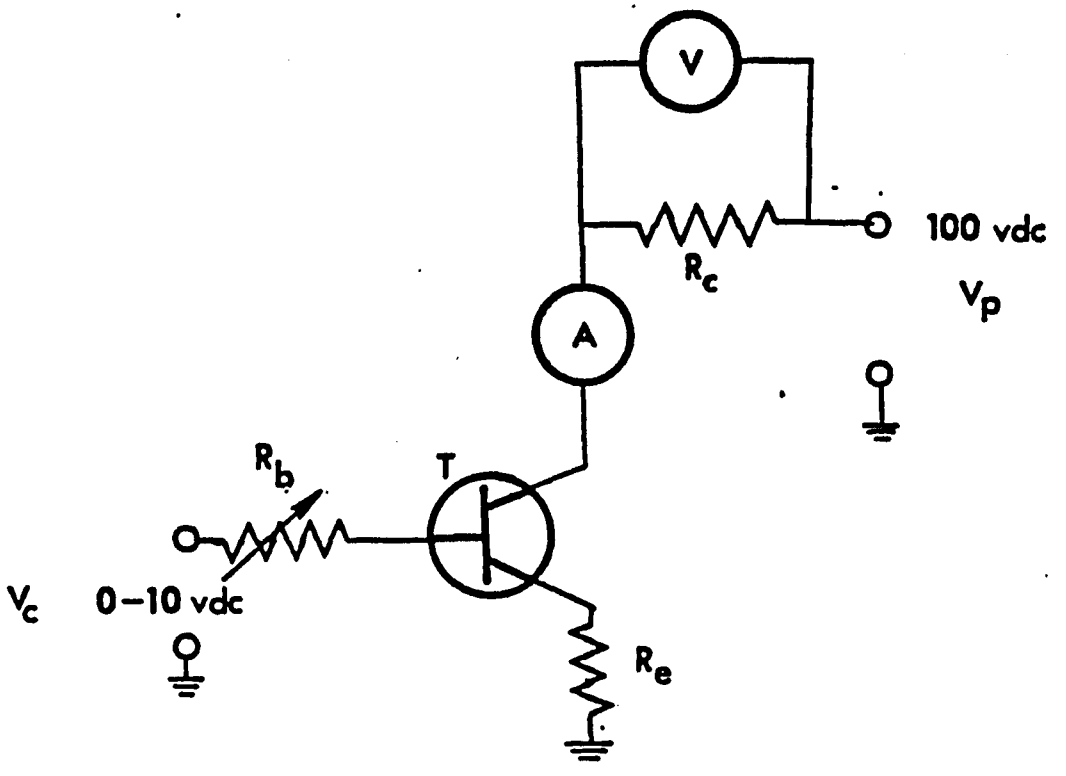

V	Voltmeter
A	Ammeter
R_c	Cryostat Heater
R_b	Base Resistor
R_e	Emiter Resistor
T	GE-251 NPN Transistor
V_p	100 VDC-3.5 Amp Regulated Power Supply
V_c	Control Voltage

Figure 7. Cryostat Heater Circuit
(Courtesy Dr. A. Popowicz)

incorporates 28K bytes of random access memory, a dual floppy disk drive (500K bytes of available soft storage), and a real time programmable clock. Software had been developed[2] for temperature control and data acquisition by using an RT-11 Fortran programming language.

The Cryostat Pressure/Temperature Interactive Control program, CRYPTIC for short, had been written[2] to give the user of the cryostat total control of the system. The operation of the system can be performed completely manually, fully automated, or to varying degrees of automatic control. Various routines or subprograms are accessed by the console operator with the main program. Requests for experimental parameters, such as temperature or pressure measurement, are acknowledged and performed by the computer. The CRYPTIC program consists of the main program and eleven subroutines. These are discussed by Popowicz[2] in great detail, including a listing of the entire program.

IIIB. Gas Purification and Analysis

IIIB-1. Introduction

The cryostat-manometry system used to measure the vapor pressures of the isotopic methyl fluorides requires samples of exceptionally high chemical purity. The introduction of a small quantity of impurity into the liquid-vapor equilibrium can result in a significant change in the experimentally observed vapor

pressure differences. The nature of the impurity determines the direction in which the observed vapor pressures and the differences between them are shifted. This can be represented by using Raoult's Law for an ideal liquid solution. If an impurity of vapor pressure, P_i, is present, the observed vapor pressure for methyl fluoride, P_{CH_3F}, is given by

$$P_{CH_3F} = P^\circ_{CH_3F} x_{CH_3F} + P_i x_i \qquad (20)$$

where $P^\circ_{CH_3F}$ is the vapor pressure of the pure liquid, and x_{CH_3F} and x_i are the mole fractions of the methyl fluoride and the impurity, respectively, in the liquid phase. For a non-volatile impurity, $P_i << P^\circ_{CH_3F}$, and the observed vapor pressure of methyl fluoride will be lowered. The opposite effect will result from a volatile impurity; where $P_i >> P^\circ_{CH_3F}$, and the experimentally observed vapor pressure will be increased. In either case, the presence of an impurity in one of the isotopic species can lead to a very large error in the measurement of the differential pressure. For example: a non-volatile impurity is present at a level of 0.1% in a methyl fluoride sample. At moderate vapor pressure ($\sim$ 500 torr), the error introduced by the impurity on the absolute pressure is approximately 0.5 torr (according to Eq. (20)). In measuring the differential pressure, an error of 0.5 torr in one isotopic species implies an error as large as 25% in the vapor pressure isotope effect. A similar situation arises for more volatile impurities when measuring vapor pressures. By reducing the concentration of the impurity to less than 50 ppm, the contribution of the impurity to the vapor pressure is reduced to less than 1%. To achieve such a high degree

of chemical purity, a preparative gas chromatography system and a high vacuum gas-solid adsorption system were utilized.

IIIB-2. Preparative Gas Chromatography

For each of the isotopically labelled samples, approximately one liter of gas at one atmosphere and room temperature was purchased or synthesized. Purification of this quantity of material required the use of high-vacuum system with direct access to a preparative gas chromatography system. A schematic of the apparatus is shown in Figure 8. The purification system consists of three principal sections:

1) service vacuum system
2) chromatographic columns
3) effluent collection system

The service vacuum system is constructed of Pyrex glass. An Eck and Krebs two stage diffusion pump provides a vacuum on the order of 10^{-6} torr. Vacuum readings are made using a Veeco (Hot Cathode) Ionization Gauge and Ionization Gauge Controller. The manifold has several ports, each consisting of a high vacuum stopcock and a standard 10/30 taper joint. Pressure readings are measured by a Wallace-Tiernan differential pressure gauge between 0-800 torr. The internal volume of the glass system has been calibrated, and pressure readings can be converted into units of volume.

The chromatographic columns are constructed of 3/8" O.D. copper tubing. They are connected to the chromatographic assembly by Cajon's

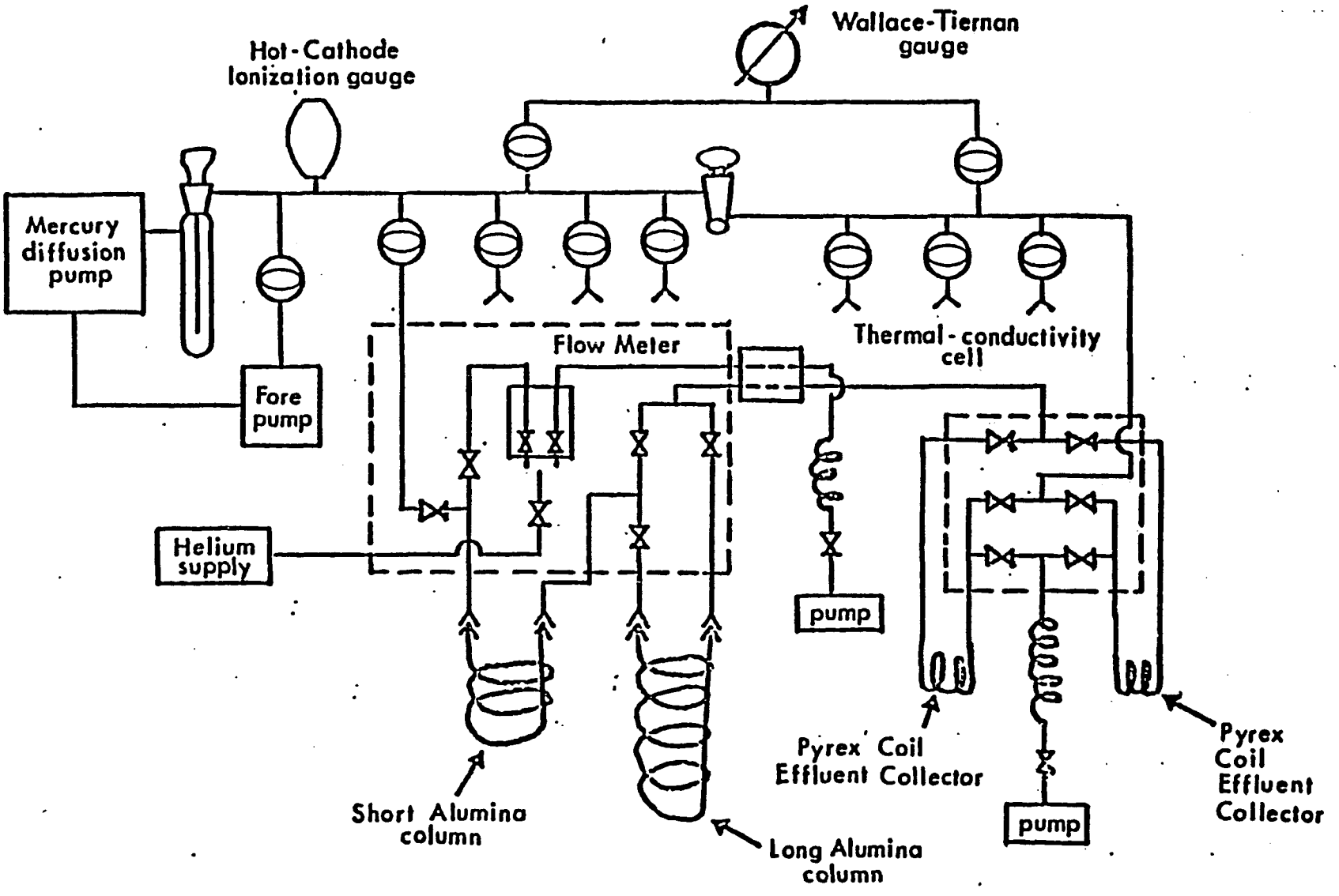

Figure 8. Preparative Gas Chromatograph

high vacuum VCR fittings. The chromatograph column assembly is constructed of stainless steel tubing and Hoke bellows-sealed valves and is connected to the service vacuum system by a glass to metal bellows seal. It incorporates a dual-flow meter-needle valve assembly, which regulates the helium flow rate to the chromatographic columns. The system design is set up to handle both columns in tandem, or allow for the second column to be bypassed.

The effluent collection system is connected directly to the service vacuum system to enable the transfer of gas fractions into sample holders. The effluent collection coils are connected to the chromatographic column assembly through a network of stainless steel tubing, bellows-sealed valves, and Kovar seals. The system is designed with two sets of matching coils and valves to avoid interruption of the gas flow while collecting fractions.

IIIB-3. Gas-Solid Adsorption System

The use of solid supports such as alumina, silica gel, and molecular sieve in the preparative gas chromatograph are effective in reducing high concentrations of impurities to less than 0.01%. To improve on these results, a pair of high vacuum gas-solid adsorption systems were built. A typical set-up is illustrated in Figure 9. The use of solid adsorbents proved highly efficient in removing some of the impurities present at the 1-100 ppm level in a relatively short time. The sample holder was connected to the glass (Pyrex) vacuum system by a standard 10/30 taper joint. A

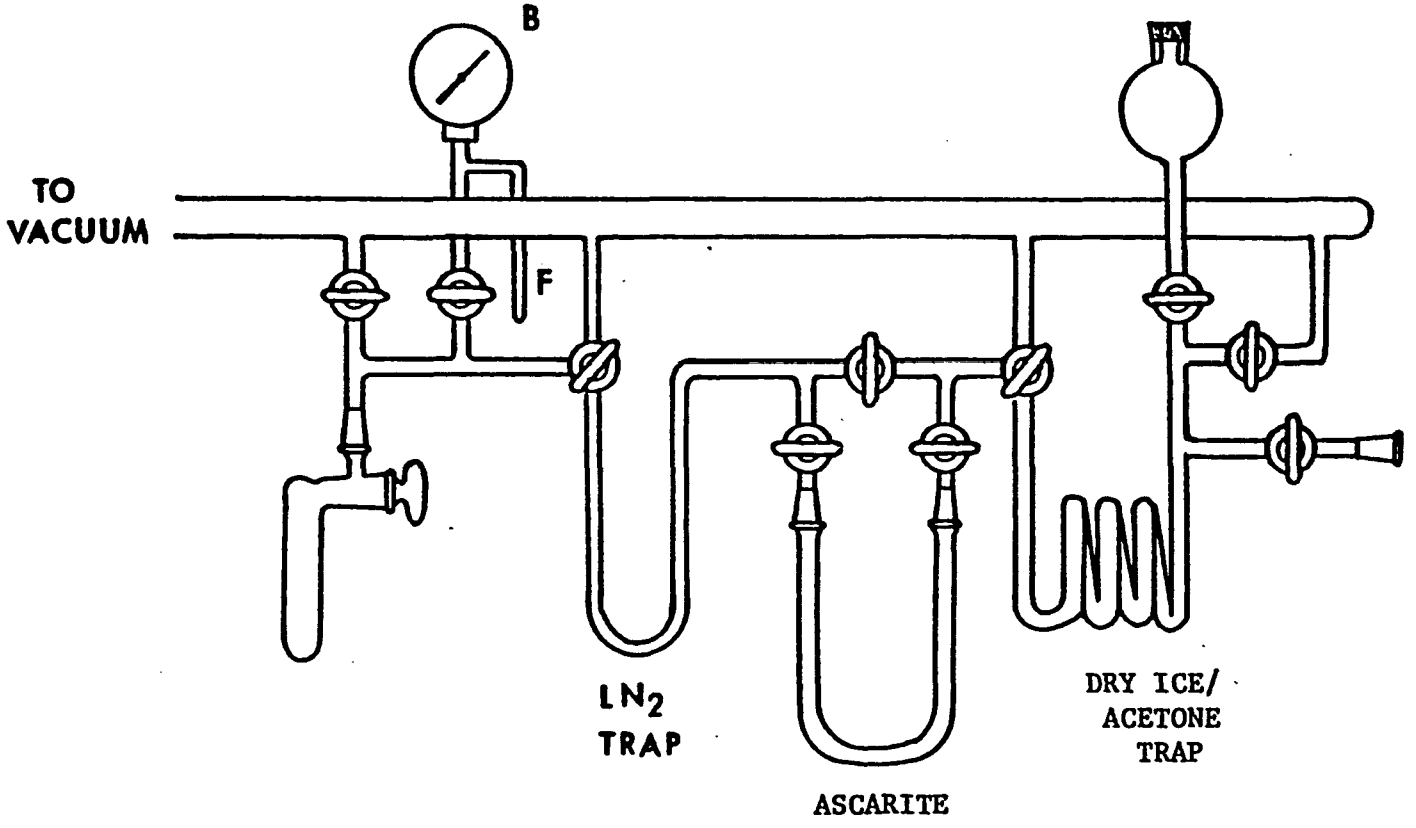

Figure 9. Gas-Solid Adsorption System

large U-tube (15 mm o.d. X 60 cm) was packed with adsorbent and attached to the vacuum system by Cajon O-ring connectors. The gaseous sample was introduced into the system, passed through the solid adsorbent, collected in a cold trap, and analyzed by an analytical gas chromatograph.

IIIB-4. Analytical Gas Chromatography

A Perkin-Elmer model 990 gas chromatograph was used to perform purity analyses on all the gaseous samples. The gas chromatograph (GC) has a modified injection port capable of handling large amounts of gas sample without contamination by air. Gases are loaded into a U-shaped glass sample holder equipped with a 4-way high-vacuum stopcock, solidified, and then degassed (removing air and low boiling impurities). The sample holder is then connected directly into the modified injector port, and the high-vacuum stopcock is opened. The carrier gas purges the glass sample holder, and the sample is carried through the packed column. A silica gel column was most effective in producing the best overall separation of methyl fluoride from its impurities. A thermal conductivity detector with a current of 225 mA at 250°C was used to detect the main component and its impurities. The detection limit of the gas chromatographic system is on the order of one ppm.

IV. EXPERIMENTAL PROCEDURE

IVA. Chemical Purification

IVA-1. Isotopic Methyl Fluorides

The preparative gas chromatograph described in Section IIIB-2 was used to purify approximately one liter of each of the isotopic methyl fluorides. Both short (∿ 1 1/2 meters) and long (∿ 6 meters) columns were packed with silica gel. The short column was submerged in a liquid nitrogen trap, and the sample was condensed into the coil through the service vacuum system. The short column was quickly warmed to room temperature by replacing the cold trap with a warm water bath. A heating mantle was placed over the short column, while the longer column is thermostatted by its own heater at ∿ 60°C. The helium carrier gas flow was established at 20 cm^3/min and maintained for the duration of the experiment. A Tesla coil was used to periodically test the gas stream as it passed through the effluent collection system. The isotopic methyl fluorides can be readily recognized by their deep purple color when ionized as compared to the light pink color for helium. When the main component began to elute, fractions were collected by condensing the gas in a liquid nitrogen trap. The use of a dual-coil collector system

enables one to trap the gaseous sample in one coil while transferring the last-trapped fraction from the other coil to a sample holder. Fractions were collected very quickly at the peak of CH_3F, and then more leisurely as the rate of elution tailed off. Approximately 20-25 fractions were collected and analyzed on the Perkin-Elmer GC.

The impurities were qualitatively and quantitatively determined by running chromatograms of known compounds and comparing retention times with the isotopic samples. Retention times were obtained using a 6' X 1/8" o.d. stainless steel column filled with 5.5 g of silica gel at 85°C and a helium flow rate of 60 cc/min. The purest fractions were recombined in a one liter bulb and tested again for chemical purity.

The presence of high levels of carbon dioxide (above 200 ppm) after preparative GC necessitated the development of a secondary technique which would be effective in the reducing impurity levels to about one ppm. The introduction of a gas-solid adsorption system (cf. Section IIIB-3) fulfilled this requirement. Adsorbents such as Ascarite (a sodium hydroxide coated asbestos pellet) and Chromosorb 102 proved exceptionally effective in removing carbon dioxide, water and methyl chloride from the isotopic methyl fluorides. A large U-tube (cf. Figure 9) was packed with adsorbent, evacuated on a high-vacuum system, wrapped with heating tape and baked at high temperature to desorb any traces of gases in the adsorbent. The sample was slowly passed through the column ($\sim$ 10-15 cc/min), then collected and analyzed. A significant improvement in the level of

impurities was noted, and the procedure was repeated several times until a satisfactory result was attained. Figure 10 shows the level of impurities in the original sample of methyl fluoride-d_3, and Figure 11 illustrates the impurity levels in the final, purified product.

Both chromatographs were run on a 6' X 1/8" o.d. stainless steel column packed with silica gel at 85°C. The helium flow rate was set at approximately 60 cc/min, and the recorder chart speed fixed at 1/2 inch/min. The order of elution was air, carbon dioxide, water, an 'unknown' impurity, methyl fluoride-d_3, and methyl chloride-d_3. After the elution of methyl chloride-d_3, the temperature was increased at a rate of 3°C/min by the temperature-programming mode of the GC. A maximum temperature of 180°C was imposed on the silica gel column to prevent the destruction of the SiO_2-H_2O network. The temperature was maintained at the maximum imposed value for over 30 minutes, and there were no traces of additional impurities. The other isotopic species, carbon-12 and carbon-13 methyl fluoride, contained similar impurities and an analogous procedure was followed. A summary of the chemical analyses of the isotopic methyl fluorides is given in Table 1. In each case, the final, purified product attained a purity level exceeding 99.996%. None of the impurities were present at a level above 15 ppm, and almost all had values measured below 10 ppm.

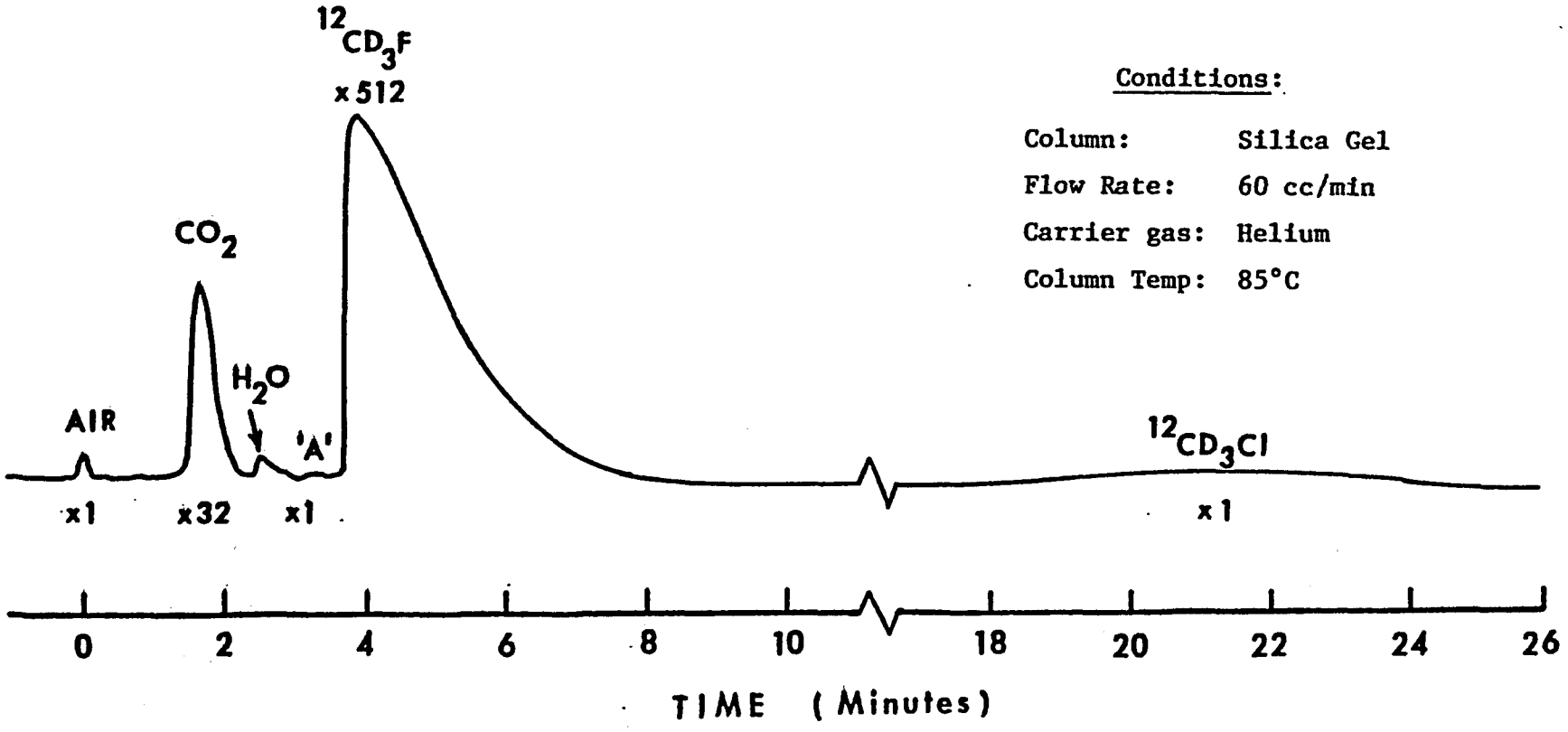

Figure 10. Gas-chromatogram of methyl fluoride-d_3 supplied by the manufacturer.

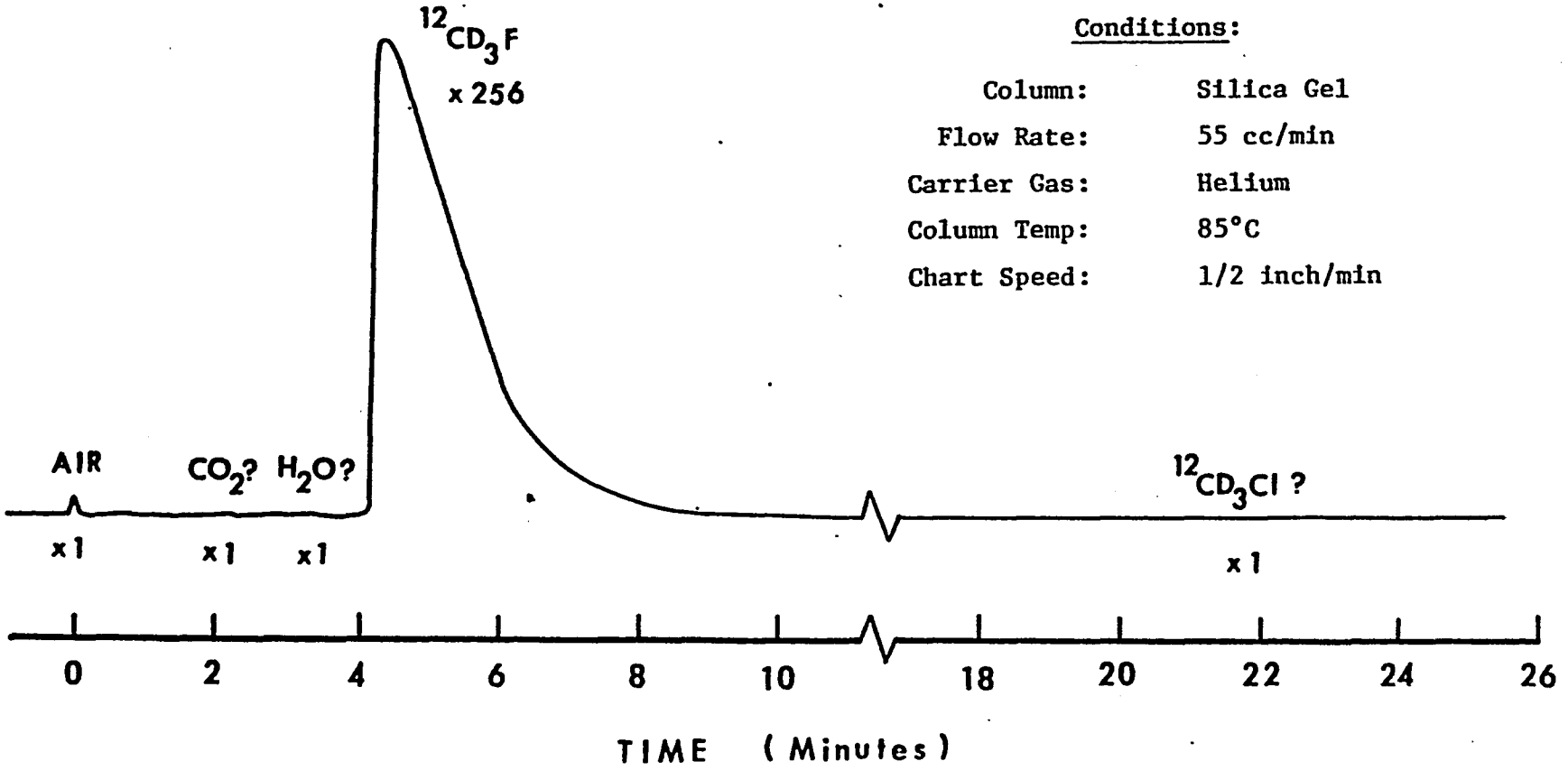

Figure 11. Gas-chromatogram of final purified fraction of methyl fluoride-d_3

Table 1. Chemical Analysis of the Methyl Fluorides

Principle Component	Impurities	Initial Composition	Final Composition
$^{13}CH_3F$[a]	---	97.4%	99.99$_6$%
	$^{13}CO_2$	1.5%	< 10 ppm
	$^{13}CH_3Cl$	1.1%	< 10 ppm
	H_2O	100 ppm	< 5 ppm
	'others'	---	~ 15 ppm
$^{12}CH_3F$[b]	---	97.7%	99.99$_6$%
	'others'	0.2%	< 10 ppm
	$^{12}CO_2$	500 ppm	< 5 ppm
	$^{12}CH_3Cl$	200 ppm	< 10 ppm
	H_2O	100 ppm	< 10 ppm
$^{12}CD_3F$[c]	---	99.4%	99.99$_7$%
	$^{12}CO_2$	0.6%	~ 5 ppm
	$^{12}CD_3Cl$	150 ppm	< 10 ppm
	H_2O	50 ppm	~ 10 ppm
	'others'	10 ppm	< 1 ppm

[a] synthesized using 90.6% $^{13}CH_3OH$

[b] purchased from Linde

[c] purchased from Prochem (98% D)

IVA-2. Ethane and Propane

To facilitate a reliable temperature scale for the vapor pressure measurements, natural abundance samples of ethane and propane were purified, and their vapor pressures were used as a calibration standard.

The ethane sample was purchased from Matheson and purified by means of a preparative gas chromatograph using a 5 meter column (3/8" o.d.) of molecular sieve (13X, 60/80 mesh) at temperatures between 40-60°C. The short column (silica gel) was immersed in liquid nitrogen, and the sample transferred into the coil by the vacuum line. The procedure followed was identical to the one describing methyl fluoride purification. The recombined fractions were passed through the gas-solid adsorption system (packed with Ascarite), collected and analyzed. The purified ethane showed the following impurities: 10 ppm of carbon dioxide, 20 ppm of water, 25 ppm of ethylene, and a trace (< 1 ppm) of propane.

The propane sample was purchased from Phillips Petroleum and purified by preparative GC using an analogous procedure as described for ethane except at slightly elevated temperatures (60-75°C). An analysis of the combined fractions of the purified propane revealed the following impurities: 15 ppm of carbon dioxide, 30 ppm of water, and a trace (< 1 ppm) of ethylene.

IVB. Isotopic Analysis of the Methyl Fluorides

The isotopic composition of the purified methyl fluorides was determined by a Kratos MS30 Dual Beam Mass Spectrometer - DS50 Data Base System (courtesy of Dr. Charles Iden, Mass Spectrometry Laboratory, Departments of Chemistry and Pharmacology, State University of New York at Stony Brook). The data was corrected for relative intensities[30] of each peak, and the results are summarized in Table 2.

IVC. Vapor Pressure Measurements

Purified samples of isotopic methyl fluoride were mounted on the sample inlet system and transferred into the adjacent cold finger. Prior to sample introduction into the cryostat, the inner assemblies were cooled down to temperatures below -150°C. Liquid nitrogen was drawn through the RRS coil and helium gas was added to the inner vacuum jacket. Helium acted as a transfer gas, allowing for a more rapid cool-down of the cryostat. Upon reaching the desired temperature, the helium gas was evacuated and the inner vacuum jacket was pumped down to high vacuum. The LN_2 was siphoned through the RRS coil at a much slower rate. The heat switch was pneumatically actuated and the SH was slowly cooled while the remaining subassemblies (LRS, URS, and ARS) were heated to slightly above the normal freezing point of the sample. The CL were warmed

Table 2. Isotopic Analysis of the Purified Methyl Fluorides

Isotope	Nominal Mass	Component	Composition
$^{12}CH_3F$	34	$^{12}CH_3F$	98.48%
	35	$^{13}CH_3F$	1.52%
$^{13}CH_3F$	34	$^{12}CH_3F$	16.72%
	35	$^{13}CH_3F$	83.28%
$^{12}CD_3F$	34	$^{12}CH_3F$	0.25%
	35	$^{12}CH_2DF$	0.59%*
	36	$^{12}CHD_2F$	1.15%
	37	$^{12}CD_3F$	97.41%
	38	$^{13}CD_3F$	0.60%

*Approximated as the intermediate value between $^{12}CH_3F$ and $^{12}CHD_2F$.

to 10° or 15°K above the freezing point to guard against parasitic condensation when transferring the gas into the sample holder ports. After the isotopic samples were introduced into the cryostat, the system was gradually adjusted to the desired temperature range, always keeping the SH as the coldest inner assembly.

To maintain the temperature of the individual components, heat must be constantly added to the system. A current between 5 ma-dc and 250 ma-dc supplied adequate power for maintaining the temperature of each cryostat component. The RRS, because of its proximity to the LN_2 dewar, always lags behind in temperature, and was the only assembly kept at a lower temperature than the SH. When the temperature of each component approached the desired value, currents were cut back and the temperature levels off. The system was allowed to reach equilibrium very slowly. This procedure was applied to the LRS, URS, ARS, and Cl simultaneously. The SH temperature was then adjusted to a temperature level $\sim$ 0.2°K colder than the other internal assemblies (avoiding parasitic condensation). This procedure is illustrated in Figure 12. Pressure fluctuations were monitored from the SQG, and equilibrium conditions were usually established one hour to ninety minutes after the procedure was initiated. Vapor pressure readings were recorded off the SQG, differential pressures measured on the capacitance gauges, and temperatures obtained from resistance values on the Keithley DVOM. The same procedure was repeated for each consecutive data point.

At the end of a series of data points, the samples were recondensed out of the sample holder and into their respective

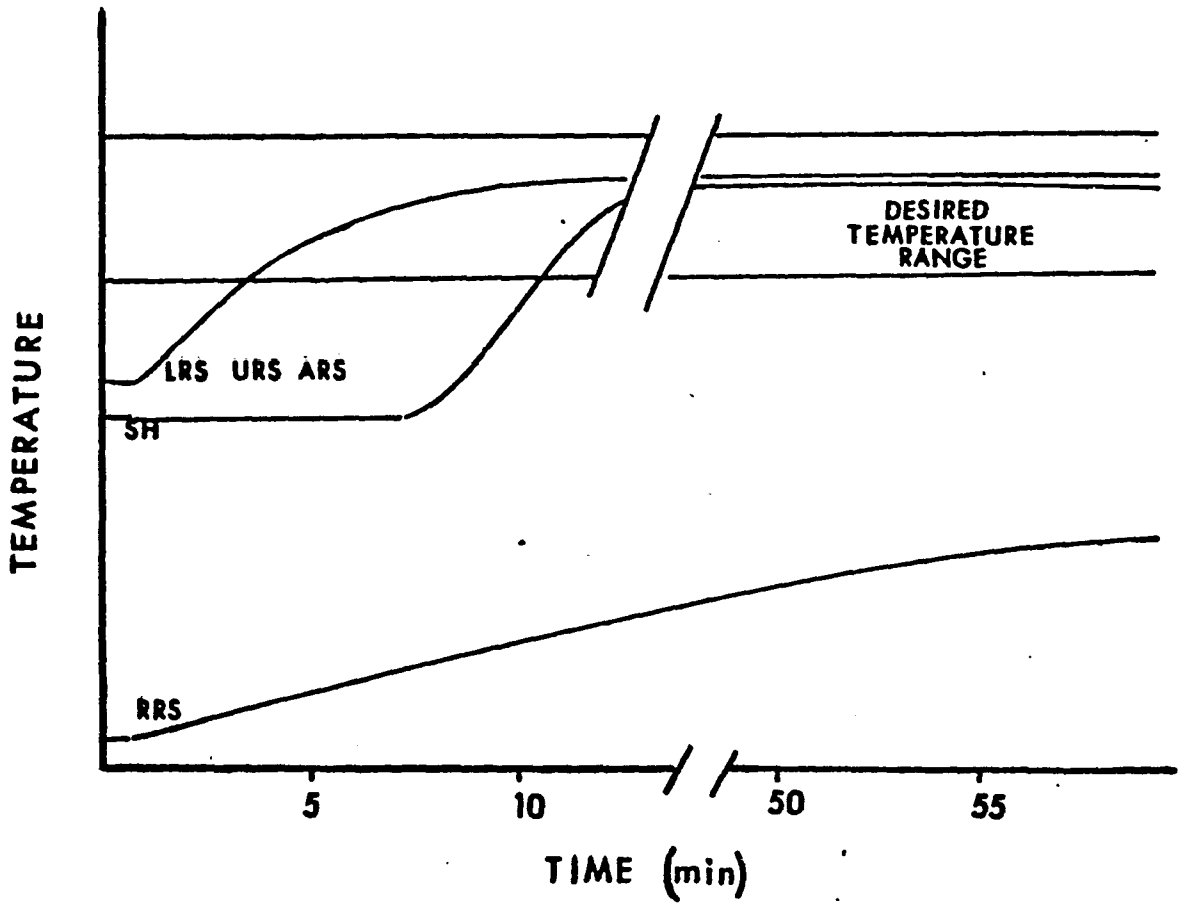

Figure 12. Thermal Control Logic for All Cryostat Components

manifolds in the sample inlet system. This process was hastened by the heating of all the internal assemblies and the capillary lines. The LN_2 in the cryogenic dewar was vaporized, the vacuum service lines thoroughly evacuated and degassed, and the electronic instrumentation (heaters, voltmeters, and recorders) turned off. The system was maintained under high vacuum (10^{-7} torr) at all times and was ready for a new set of isotopic measurements after three days of outgassing.

V. EXPERIMENTAL RESULTS

VA. Experimental Vapor Pressure Data

The vapor pressure isotope effects in $^{12}CH_3F$, $^{13}CH_3F$, and $^{12}CD_3F$ were measured using the precision cryostat. The temperature fluctuation was maintained within one millidegree during the measurement of all the data points. The $^{12}CH_3F$ sample served as a reference gas for the capacitance gauges. Measurements were performed between temperatures of 132.52°K and 213.12°K. The hydrogen/deuterium vapor pressure isotope effect, $^{12}CH_3F/^{12}CD_3F$ is summarized in Figure 13, and the carbon vapor pressure isotope effect, $^{12}CH_3F/^{13}CH_3F$, is illustrated in Figure 14.

VB. Data Reduction

VB-1. Calibration of Temperature Scale

The vapor pressure of ethane and propane were used to calibrate the platinum resistance thermometer (PRT) located in the sample holder block of the cryostat. Absolute pressures were measured using the quartz spiral gauge. The experimentally measured vapor pressure data of Rossini[31] were used as calibration

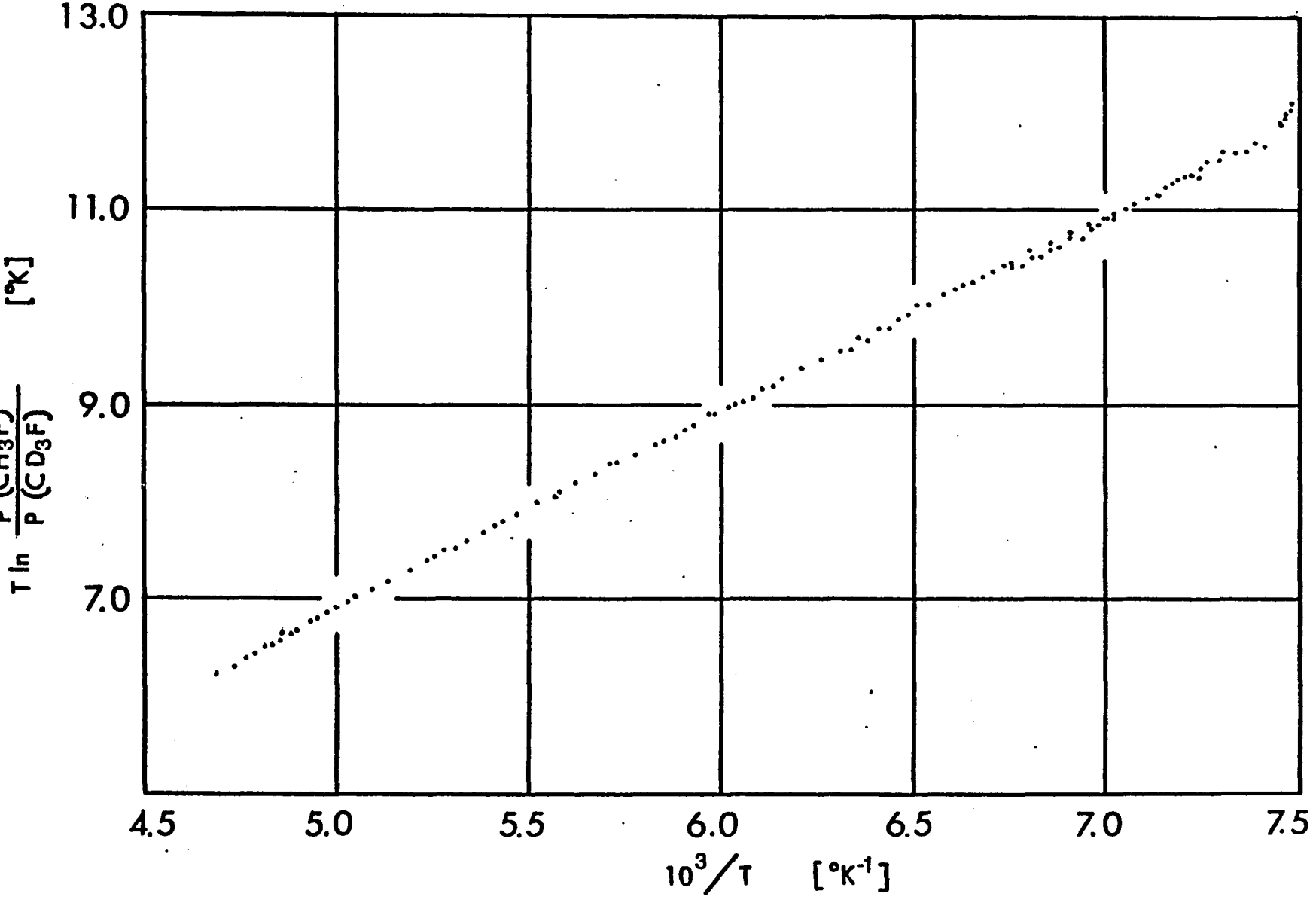

Figure 13. H/D-VPIE in Methyl Fluoride

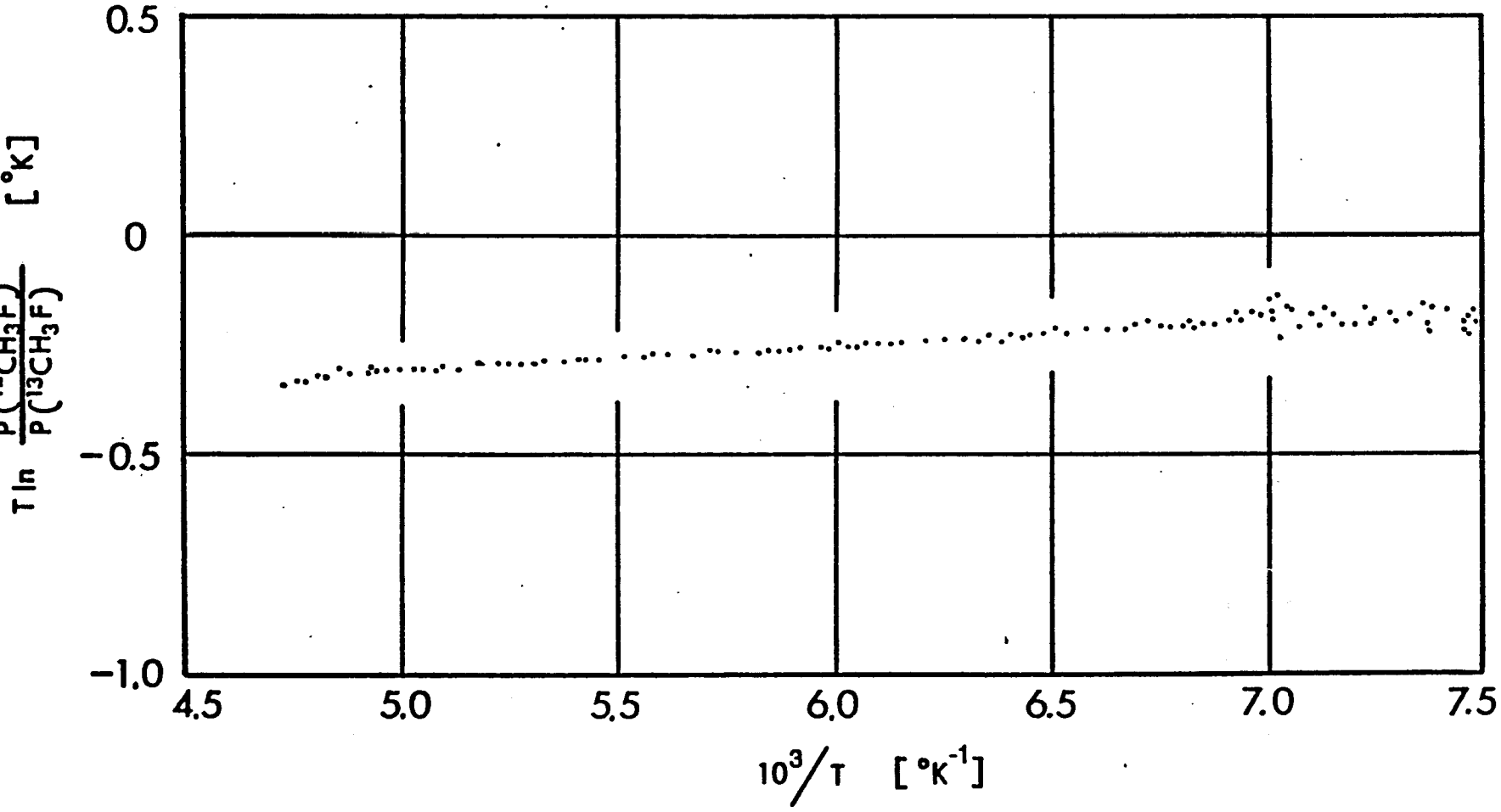

Figure 14. $^{12}C/^{13}C$-VPIE in Methyl Fluoride

standard.

A specimen of ethane purified by the procedure previously described in Section IV was introduced into the cryostat, and its vapor pressure was recorded between 128°K and 199°K. The least-squares fit of 105 data points to the functional form

$$\log_{10} p(\text{torr}) = \frac{a}{b+t'(°C)} + c \qquad (21)$$

resulted in

$$a = -651.71 \pm 0.76 \quad \text{torr °C}$$

$$b = 255.34 \pm 0.10 \quad °C$$

$$c = 6.7892 \pm 0.0026 \quad \text{torr}$$

in which t'(°C) was the temperature of the sample holder read off the PRT. This compares to Rossini's vapor pressure data on ethane

$$\log_{10} p(\text{torr}) = \frac{-656.40}{256.00+t(°C)} + 6.80266 \; . \qquad (22)$$

An analogous series of vapor pressure measurements on propane between 160°K and 242°K were conducted. The 97 experimental calibration points were fit to the form of Eq. (18), and the values for the constants are:

$$a = -807.60 \quad \text{torr °C}$$

$$b = 247.60 \quad °C$$

$$c = 6.8111 \quad \text{torr}$$

Rossini's vapor pressure equation for propane is

$$\log_{10} p(\text{torr}) = \frac{-813.20}{248.00+t(°C)} + 6.8297 \; . \qquad (23)$$

The differences in the temperatures between our PRT readings and Rossini's were computed for both ethane and propane data. Our temperature scale was slightly higher than Rossini's temperatures for ethane and slightly lower than Rossini's temperatures for propane. The calibration for the PRT temperature scale was obtained by averaging the two sets of data over the entire temperature range. Table 3 summarizes the temperature differences for ethane and propane, and the net average temperature correction for the PRT temperature scale. These corrections ranged for -0.04°K at very low temperature (130°K), approximately zero at high temperature (210°K), and on the order of 0.02°K over the intermediate temperature range (170-200°K). These temperature adjustments were applied to all vapor pressure data measurements on methyl fluoride.

VB-2. Corrections for Isotopic Impurities and Non-Ideality

The experimentally observed vapor pressure data of each of the isotopic species have been corrected for isotopic impurities. The isotopic mixtures were treated ideally and Raoult's Law was applied. The pressures of the pure isotopic species are expressed as follows:

$$P_{(^{12}CH_3F)} = \frac{P_{OBS_{(^{12}CH_3F)}} \cdot (1-x_{12}) - P_{OBS_{(^{13}CH_3F)}} \cdot (x_{13})}{1-x_{12}-x_{13}} \qquad (24)$$

$$P_{(^{13}CH_3F)} = \frac{P_{OBS_{(^{13}CH_3F)}} \cdot (1-x_{13}) - P_{OBS_{(^{12}CH_3F)}} \cdot (x_{12})}{1-x_{12}-x_{13}} \qquad (25)$$

Table 3. Corrections to Platinum Resistance Thermometer Temperature Scale

Temperature Reading on PRT (°K)	Difference (vs. Rossini) Ethane ΔT (°K)	Difference (vs. Rossini) Propane ΔT (°K)	Temperature Correction (°K)	Corrected Temperature (°K)
132.00	-0.1088	0.0355	-0.0367	131.96
133.00	-0.1064	0.0375	-0.0345	132.97
134.00	-0.1040	0.0394	-0.0323	133.97
135.00	-0.1016	0.0413	-0.0302	134.97
136.00	-0.0993	0.0432	-0.0281	135.97
137.00	-0.0970	0.0450	-0.0260	136.97
138.00	-0.0948	0.0467	-0.0241	137.98
139.00	-0.0926	0.0484	-0.0221	138.98
140.00	-0.0905	0.0501	-0.0202	139.98
141.00	-0.0884	0.0517	-0.0183	140.98
142.00	-0.0863	0.0533	-0.0165	141.98
143.00	-0.0843	0.0548	-0.0147	142.99
144.00	-0.0823	0.0563	-0.0130	143.99
145.00	-0.0803	0.0577	-0.0113	144.99
146.00	-0.0784	0.0591	-0.0097	145.99
147.00	-0.0766	0.0604	-0.0081	146.99
148.00	-0.0747	0.0617	-0.0065	147.99
149.00	-0.0729	0.0630	-0.0050	149.00
150.00	-0.0712	0.0642	-0.0035	150.00
151.00	-0.0695	0.0653	-0.0021	151.00

[continued]

Temperature Reading on PRT (°K)	Difference (vs. Rossini) Ethane ΔT (°K)	Difference (vs. Rossini) Propane ΔT (°K)	Temperature Correction (°K)	Corrected Temperature (°K)
152.00	-0.0679	0.0664	-0.0007	152.00
153.00	-0.0662	0.0675	0.0006	153.00
154.00	-0.0647	0.0685	0.0019	154.00
155.00	-0.0631	0.0695	0.0032	155.00
156.00	-0.0616	0.0704	0.0044	156.00
157.00	-0.0602	0.0713	0.0056	157.01
158.00	-0.0588	0.0721	0.0067	158.01
159.00	-0.0574	0.0729	0.0078	159.01
160.00	-0.0561	0.0737	0.0088	160.01
161.00	-0.0548	0.0744	0.0098	161.01
162.00	-0.0535	0.0750	0.0107	162.01
163.00	-0.0523	0.0756	0.0116	163.01
164.00	-0.0512	0.0762	0.0125	164.01
165.00	-0.0501	0.0767	0.0133	165.01
166.00	-0.0490	0.0772	0.0141	166.01
167.00	-0.0479	0.0776	0.0148	167.01
168.00	-0.0469	0.0779	0.0155	168.02
169.00	-0.0460	0.0783	0.0161	169.02
170.00	-0.0451	0.0786	0.0167	170.02
171.00	-0.0442	0.0788	0.0173	171.02

[continued]

Temperature Reading on PRT (°K)	Difference (vs. Rossini) Ethane ΔT (°K)	Difference (vs. Rossini) Propane ΔT (°K)	Temperature Correction (°K)	Corrected Temperature (°K)
172.00	-0.0434	0.0790	0.0178	172.02
173.00	-0.0426	0.0791	0.0183	173.02
174.00	-0.0418	0.0792	0.0187	174.02
175.00	-0.0411	0.0793	0.0191	175.02
176.00	-0.0404	0.0793	0.0194	176.02
177.00	-0.0398	0.0792	0.0197	177.02
178.00	-0.0392	0.0792	0.0200	178.02
179.00	-0.0387	0.0790	0.0202	179.02
180.00	-0.0382	0.0788	0.0203	180.02
181.00	-0.0377	0.0786	0.0204	181.02
182.00	-0.0373	0.0784	0.0205	182.02
183.00	-0.0369	0.0780	0.0206	183.02
184.00	-0.0366	0.0777	0.0205	184.02
185.00	-0.0363	0.0773	0.0205	185.02
186.00	-0.0360	0.0768	0.0204	186.02
187.00	-0.0358	0.0763	0.0202	187.02
188.00	-0.0356	0.0758	0.0201	188.02
189.00	-0.0355	0.0752	0.0198	189.02
190.00	-0.0354	0.0745	0.0196	190.02
191.00	-0.0354	0.0739	0.0192	191.02

[continued]

Temperature Reading on PRT (°K)	Difference (vs. Rossini) Ethane ΔT (°K)	Difference (vs. Rossini) Propane ΔT (°K)	Temperature Correction (°K)	Corrected Temperature (°K)
192.00	-0.0354	0.0731	0.0189	192.02
193.00	-0.0354	0.0723	0.0185	193.02
194.00	-0.0355	0.0715	0.0180	194.02
195.00	-0.0356	0.0707	0.0175	195.02
196.00	-0.0357	0.0697	0.0170	196.02
197.00	-0.0359	0.0688	0.0164	197.02
198.00	-0.0362	0.0678	0.0158	198.02
199.00	-0.0365	0.0667	0.0151	199.02
200.00	-0.0368	0.0656	0.0144	200.01
201.00	-0.0371	0.0645	0.0137	201.01
202.00	-0.0375	0.0633	0.0129	202.01
203.00	-0.0380	0.0621	0.0120	203.01
204.00	-0.0385	0.0608	0.0112	204.01
205.00	-0.0390	0.0595	0.0102	205.01
206.00	-0.0396	0.0581	0.0093	206.01
207.00	-0.0402	0.0567	0.0083	207.01
208.00	-0.0408	0.0552	0.0072	208.01
209.00	-0.0415	0.0537	0.0061	209.01
210.00	-0.0422	0.0521	0.0050	210.00
211.00	-0.0430	0.0505	0.0038	211.00
212.00	-0.0438	0.0489	0.0025	212.00
213.00	-0.0447	0.0472	0.0013	213.00

$$P_{(^{12}CD_3F)} = [P_{OBS(^{12}CD_3F)} - P_{(^{12}CH_3F)}(x_{12} + \frac{x_2}{3} + \frac{2x_1}{3}) - (P_{(^{13}CH_3F)} + P_{(^{12}CD_3F)} - P_{(^{12}CH_3F)}) \cdot (x_{13}D)]/ x_3 + \frac{2x_2}{3} + \frac{x_1}{3} \quad (26)$$

where P_{OBS} represents the experimentally observed vapor pressure of the isotopic species, and the mole fractions x_1, x_2, x_3 and x_{13D} represent the isotopic species $^{12}CDH_2F$, $^{12}CD_2HF$, $^{12}CD_3F$, and $^{13}CD_3F$, respectively. The notations X_{12} and X_{13} refer to the mole fractions of ^{12}C in the carbon-13 sample and ^{13}C in the carbon-12 sample, respectively. The vapor pressure of $^{12}CD_2HF$ and $^{12}CDH_2F$ have been approximated by the rule of the geometric mean[32] as

$$P(^{12}CDH_2F) = P(^{12}CD_3F)^{1/3} \cdot P(^{12}CH_3F)^{2/3} \quad (27)$$

and

$$P(^{12}CD_2HF) = P(^{12}CD_3F)^{2/3} \cdot P(^{12}CH_3F)^{1/3} \quad (28)$$

Similarly, the vapor pressure of $^{13}CD_3F$ is approximated by

$$P(^{13}CD_3F) = P(^{13}CH_3F) \cdot P(^{12}CD_3F) / P(^{12}CH_3F) \quad (29)$$

The values for each of the mole fraction terms was determined by mass spectrometric analysis (Section IV). The approximations introduced into the calculation of the pure vapor pressure of $^{12}CD_3F$ lead to errors which are fairly small.

To transform the vapor pressure data to the information on the reduced partition function ratio, the data was corrected for gas non-ideality[32] and condensed phase molar volume isotopic differences:[32]

$$\ln\left(\frac{f_c}{f_g}\right) = \ln\left(\frac{P'}{P}\right)\left[1+P\left(B_o - \frac{V_\ell}{RT}\right)\right] \qquad (2)$$

The gas non-ideality correction, B_o, is expressed as[33]

$$B_o(T) = 2V^*[R_1-(1-R_1)(\exp(\bar{u}/kT)-1)-(R_2-1)(\exp(-\bar{u}/kT)-1)$$
$$-(R_3-R_2)(\exp(-0.21\bar{u}/kT)-1)] \quad \text{torr}^{-1} \qquad (30)$$

where R_1, R_2, and R_3 are 0.70, 1.13, and 7.095, respectively. V^* is the molar volume of the liquid at the boiling point (38.08 cm^3 mol^{-1}), T is the temperature in °K, and $\bar{u}/k = -365.3(1+\frac{167.3}{T})$ for methyl fluoride. The condensed phase molar volume, V_ℓ, is given by

$$V_\ell(T) = \frac{1}{D(T)} \times 34.03 \qquad (31)$$

where D(T) is the density of liquid methyl fluoride at a given temperature. The density is represented by[34]

$$D(T) = 1.2084 - 1.299\times10^{-3}T - 1.96\times10^{-6}T^2 \qquad (32)$$

where the density is in g/cm^3 and the temperature is expressed in °K. The final results are compiled in Tables 4 and 5, and the data for the H/D VPIE and $^{12}C/^{13}C$ VPIE are plotted in Figures 15 and 16, respectively.

Table 4. Hydrogen/Deuterium Vapor Pressure Isotope Effects in Methyl Fluoride

No.	T (°K)	$10^3/T$ ($°K^{-1}$)	Vapor Pressure (torr) H	Vapor Pressure (torr) D	T $\ln(P_H/P_D)$ (°K)	T $\ln(f_c/f_g)$ (°K)	Date (1980)
1.	132.48	7.548	3.7117	3.3789	12.445	12.414	10/06
2.	133.22	7.506	4.0851	3.7262	12.249	12.217	10/06
3.	133.60	7.485	4.3138	3.9323	12.370	12.336	10/13
4.	133.60	7.485	4.3275	3.9461	12.325	12.292	10/13
5.	133.84	7.471	4.4601	4.0711	12.215	12.181	10/13
6.	133.85	7.471	4.4586	4.0681	12.267	12.234	10/13
7.	134.00	7.463	4.5287	4.1364	12.141	12.108	10/06
8.	134.03	7.461	4.5653	4.1682	12.197	12.163	10/13
9.	134.78	7.419	4.9876	4.5657	11.911	11.876	10/06
10.	135.30	7.391	5.3229	4.8727	11.956	11.920	10/06
11.	135.71	7.369	5.6080	5.1385	11.866	11.829	10/06
12.	136.23	7.341	5.9876	5.4893	11.835	11.798	10/06
13.	136.82	7.309	6.4586	5.9220	11.867	11.829	10/14
14.	137.03	7.298	6.6050	6.0612	11.772	11.733	10/07
15.	137.67	7.264	7.1736	6.5867	11.751	11.710	10/14
16.	137.95	7.249	7.3915	6.7917	11.676	11.635	10/07
17.	138.04	7.244	7.4920	6.8833	11.699	11.657	09/29
18.	138.06	7.243	7.5089	6.9044	11.588	11.547	10/10
19.	138.14	7.239	7.5683	6.9597	11.581	11.540	10/10
20.	138.25	7.233	7.6781	7.0625	11.554	11.512	10/10

[continued]

No.	T (°K)	$10^3/T$ ($°K^{-1}$)	Vapor Pressure (torr) H	Vapor Pressure (torr) D	T $\ln(P_H/P_D)$ (°K)	T $\ln(f_c/f_g)$ (°K)	Date (1980)
21.	138.42	7.223	7.8459	7.2139	11.624	11.582	10/14
22.	138.42	7.223	7.8504	7.2157	11.669	11.626	10/14
23.	138.82	7.204	8.2010	7.5432	11.607	11.564	10/07
24.	139.11	7.189	8.5027	7.8253	11.548	11.505	09/29
25.	139.35	7.176	8.7330	8.0386	11.546	11.502	10/07
26.	139.73	7.157	9.1582	8.4355	11.485	11.440	09/29
27.	139.96	7.145	9.4083	8.6634	11.545	11.500	10/15
28.	140.11	7.137	9.5880	8.8381	11.411	11.366	09/29
29.	140.34	7.125	9.8337	9.0659	11.409	11.363	10/07
30.	140.72	7.106	10.293	9.4952	11.361	11.314	09/30
31.	141.34	7.075	11.017	10.171	11.300	11.251	10/07
32.	141.72	7.056	11.536	10.655	11.261	11.212	09/30
33.	142.34	7.025	12.309	11.381	11.161	11.111	10/07
34.	142.34	7.025	12.325	11.392	11.209	11.158	10/07
35.	142.62	7.012	12.705	11.749	11.156	11.105	10/07
36.	142.75	7.007	12.873	11.904	11.172	11.121	09/30
37.	143.17	6.985	13.486	12.479	11.111	11.058	10/15
38.	143.63	6.962	14.192	13.140	11.062	11.008	10/07
39.	143.71	6.958	14.349	13.284	11.085	11.031	09/30
40.	144.13	6.938	14.997	13.900	10.948	10.893	10/16

[continued]

No.	T (°K)	$10^3/T$ ($°K^{-1}$)	Vapor Pressure (torr) H	Vapor Pressure (torr) D	T $\ln(P_H/P_D)$ (°K)	T $\ln(f_c/f_g)$ (°K)	Date (1980)
41.	144.25	6.932	15.184	14.075	10.943	10.888	10/16
42.	144.75	6.908	16.009	14.843	10.951	10.894	10/07
43.	144.75	6.908	16.042	14.870	10.977	10.920	09/30
44.	145.34	6.880	17.044	15.818	10.848	10.789	10/16
45.	145.85	6.856	18.014	16.717	10.901	10.841	09/30
46.	145.86	6.856	18.020	16.729	10.845	10.785	10/07
47.	146.40	6.831	19.067	17.717	10.755	10.694	10/16
48.	146.52	6.825	19.282	17.915	10.773	10.712	10/16
49.	146.93	6.805	20.162	18.733	10.803	10.739	09/30
50.	146.95	6.805	20.168	18.746	10.745	10.682	10/07
51.	147.54	6.778	21.463	19.966	10.665	10.601	10/16
52.	148.04	6.755	22.617	21.048	10.646	10.580	10/07
53.	148.04	6.755	22.632	21.055	10.688	10.622	09/30
54.	148.61	6.729	23.981	22.321	10.663	10.594	10/01
55.	149.15	6.705	25.303	23.566	10.607	10.537	09/30
56.	149.72	6.679	26.830	25.006	10.540	10.468	10/01
57.	150.24	6.656	28.225	26.323	10.479	10.405	09/30
58.	150.82	6.630	29.925	27.925	10.431	10.356	10/01
59.	151.37	6.606	31.509	29.417	10.398	10.320	09/30
60.	151.92	6.582	33.268	31.079	10.340	10.260	10/01

[continued]

No.	T (°K)	$10^3/T$ ($°K^{-1}$)	Vapor Pressure (torr) H	Vapor Pressure (torr) D	T $\ln(P_H/P_D)$ (°K)	T $\ln(f_c/f_g)$ (°K)	Date (1980)
61.	153.02	6.535	36.973	34.578	10.245	10.162	10/01
62.	153.57	6.512	38.916	36.405	10.243	10.157	10/01
63.	154.15	6.487	41.080	38.464	10.140	10.052	10/01
64.	154.84	6.458	43.862	41.095	10.088	9.998	10/02
65.	155.44	6.433	46.309	43.422	10.006	9.914	10/08
66.	156.04	6.409	48.941	45.905	9.994	9.899	10/02
67.	156.66	6.383	51.749	48.584	9.887	9.790	10/08
68.	157.25	6.359	54.510	51.184	9.902	9.802	10/02
69.	157.87	6.334	57.583	54.125	9.778	9.677	10/08
70.	158.59	6.306	61.296	57.631	9.778	9.673	10/02
71.	159.85	6.256	68.431	64.411	9.677	9.566	10/02
72.	161.17	6.205	76.593	72.177	9.570	9.453	10/02
73.	162.48	6.155	85.399	80.564	9.469	9.346	10/02
74.	163.13	6.130	90.229	85.176	9.402	9.276	09/23
75.	163.75	6.107	94.953	89.674	9.367	9.237	10/02
76.	164.64	6.074	102.08	96.485	9.292	9.158	09/23
77.	165.17	6.054	106.33	100.55	9.241	9.105	09/24
78.	165.68	6.036	110.71	104.71	9.232	9.093	10/02
79.	166.20	6.017	115.39	109.20	9.171	9.029	09/23
80.	167.16	5.982	124.27	117.69	9.098	8.951	09/24

[continued]

No.	T (°K)	$10^3/T$ ($°K^{-1}$)	Vapor Pressure (torr) H	Vapor Pressure (torr) D	T $\ln(P_H/P_D)$ (°K)	T $\ln(f_c/f_g)$ (°K)	Date (1980)
81.	167.37	5.975	126.33	119.65	9.100	8.952	10/02
82.	168.68	5.928	139.58	132.33	8.994	8.839	09/24
83.	169.47	5.901	148.28	140.68	8.923	8.763	10/08
84.	170.17	5.876	156.33	148.39	8.873	8.709	09/24
85.	170.98	5.849	165.91	157.57	8.820	8.651	10/08
86.	171.67	5.826	174.55	165.86	8.766	8.593	09/24
87.	173.17	5.775	194.54	185.03	8.676	8.494	09/24
88.	174.54	5.729	214.51	204.23	8.575	8.383	09/24
89.	174.88	5.718	219.71	209.21	8.562	8.368	09/24
90.	176.26	5.673	241.77	230.43	8.465	8.262	09/25
91.	177.95	5.620	271.47	259.02	8.355	8.140	09/25
92.	179.19	5.581	294.82	281.50	8.284	8.060	10/02
93.	179.65	5.566	304.04	290.40	8.244	8.016	09/25
94.	181.20	5.519	336.55	321.73	8.156	7.917	10/02
95.	181.37	5.514	340.23	325.30	8.136	7.895	09/25
96.	183.02	5.464	378.14	361.89	8.035	7.782	09/25
97.	184.16	5.430	405.97	388.78	7.965	7.703	09/25
98.	184.79	5.412	422.43	404.70	7.926	7.659	09/25
99.	185.89	5.380	451.82	433.12	7.860	7.584	09/25
100.	187.56	5.332	500.09	479.82	7.761	7.470	09/25

[continued]

No.	T (°K)	$10^3/T$ ($°K^{-1}$)	Vapor Pressure (torr) H	D	T ln(P_H/P_D) (°K)	T ln(f_c/f_g) (°K)	Date (1980)
101.	188.54	5.304	529.75	508.54	7.704	7.406	10/08
102.	189.28	5.283	553.13	531.17	7.667	7.361	09/25
103.	190.24	5.257	585.35	562.41	7.605	7.291	10/09
104.	190.97	5.236	610.23	586.52	7.569	7.249	09/25
105.	192.75	5.188	675.44	649.78	7.464	7.128	09/25
106.	194.85	5.132	759.87	731.77	7.342	6.985	09/25
107.	196.17	5.098	815.83	786.11	7.278	6.909	10/02
108.	196.73	5.083	841.28	810.88	7.243	6.868	09/25
109.	197.97	5.051	898.80	866.79	7.180	6.793	10/02
110.	198.75	5.031	936.54	903.53	7.133	6.738	10/09
111.	199.06	5.024	951.37	918.04	7.099	6.702	09/25
112.	199.95	5.001	998.05	963.38	7.069	6.662	10/02
113.	200.87	4.978	1046.8	1010.8	7.025	6.608	10/03
114.	200.87	4.978	1045.6	1009.7	7.013	6.597	09/25
115.	201.97	4.951	1106.5	1069.0	6.965	6.537	10/03
116.	202.66	4.934	1145.5	1107.0	6.934	6.499	10/09
117.	202.85	4.930	1157.7	1119.0	6.903	6.466	10/03
118.	204.18	4.898	1236.0	1195.3	6.832	6.382	09/26
119.	204.86	4.881	1279.5	1237.6	6.822	6.362	10/03
120.	205.57	4.865	1324.0	1281.0	6.792	6.324	10/09

[continued]

No.	T (°K)	$10^3/T$ ($°K^{-1}$)	Vapor Pressure (torr) H	Vapor Pressure (torr) D	T $\ln(P_H/P_D)$ (°K)	T $\ln(f_c/f_g)$ (°K)	Date (1980)
121.	205.95	4.856	1348.2	1304.9	6.728	6.259	09/26
122.	206.85	4.834	1408.7	1363.8	6.695	6.216	10/03
123.	207.75	4.813	1470.2	1424.0	6.632	6.144	09/26
124.	207.75	4.813	1471.3	1424.9	6.657	6.167	10/09
125.	208.83	4.789	1547.9	1499.8	6.597	6.095	10/03
126.	209.52	4.773	1602.7	1553.5	6.527	6.019	09/26
127.	209.85	4.765	1622.6	1572.8	6.538	6.025	10/09
128.	211.13	4.736	1724.4	1672.4	6.467	5.940	10/03
129.	211.33	4.732	1738.8	1686.6	6.444	5.916	09/26
130.	213.12	4.692	1887.0	1831.5	6.361	5.812	09/26

Table 5. $^{12}C/^{13}C$ Vapor Pressure Isotope Effects in Methyl Fluoride

No.	T (°K)	$10^3/T$ ($°K^{-1}$)	Vapor Pressure (torr) ^{12}C	Vapor Pressure (torr) ^{13}C	T ln(P'/P) (°K)	T $\ln(f_c/f_g)$ (°K)	Date (1980)
1.	132.48	7.548	3.7117	3.7175	-0.2050	-0.2045	10/06
2.	133.22	7.506	4.0851	4.0921	-0.2272	-0.2266	10/06
3.	133.22	7.506	4.0851	4.0928	-0.2510	-0.2504	10/06
4.	133.60	7.485	4.3138	4.3204	-0.2044	-0.2039	10/13
5.	133.60	7.485	4.3275	4.3351	-0.2339	-0.2333	10/13
6.	133.84	7.471	4.4601	4.4692	-0.2750	-0.2742	10/13
7.	133.85	7.471	4.4586	4.4660	-0.2238	-0.2232	10/13
8.	134.00	7.463	4.5287	4.5376	-0.2639	-0.2632	10/06
9.	134.03	7.461	4.5653	4.5736	-0.2440	-0.2433	10/13
10.	134.78	7.419	4.9876	4.9953	-0.2081	-0.2075	10/06
11.	135.30	7.391	5.3229	5.3308	-0.2019	-0.2013	10/06
12.	135.59	7.375	5.5713	5.5817	-0.2528	-0.2520	10/14
13.	135.59	7.375	5.5713	5.5826	-0.2736	-0.2728	10/14
14.	135.71	7.369	5.6080	5.6159	-0.1922	-0.1916	10/06
15.	136.23	7.341	5.9876	5.9972	-0.2197	-0.2190	10/06
16.	137.03	7.298	6.6049	6.6164	-0.2383	-0.2375	10/07
17.	137.30	7.283	6.8381	6.8488	-0.2135	-0.2128	10/15
18.	137.34	7.281	6.8976	6.9083	-0.2117	-0.2110	10/15
19.	137.95	7.249	7.3915	7.4042	-0.2372	-0.2364	10/07
20.	138.06	7.243	7.5089	7.5228	-0.2561	-0.2552	10/10

[continued]

No.	T (°K)	$10^3/T$ ($°K^{-1}$)	Vapor Pressure (torr) ^{12}C	Vapor Pressure (torr) ^{13}C	T ln(P'/P) (°K)	T $\ln(f_c/f_g)$ (°K)	Date (1980)
21.	138.14	7.239	7.5683	7.5820	-0.2498	-0.2489	10/10
22.	138.25	7.233	7.6781	7.6922	-0.2531	-0.2521	10/10
23.	138.42	7.223	7.8458	7.8571	-0.1984	-0.1977	10/14
24.	138.82	7.204	8.2010	8.2159	-0.2524	-0.2514	10/07
25.	139.35	7.176	8.7330	8.7484	-0.2457	-0.2448	10/07
26.	139.82	7.152	9.2620	9.2764	-0.2177	-0.2169	10/15
27.	139.96	7.145	9.4083	9.4222	-0.2073	-0.2065	10/15
28.	140.34	7.125	9.8336	9.8518	-0.2599	-0.2588	10/07
29.	140.84	7.100	10.443	10.459	-0.2143	-0.2134	10/15
30.	141.34	7.075	11.017	11.038	-0.2665	-0.2653	10/07
31.	141.74	7.055	11.554	11.571	-0.2099	-0.2090	10/15
32.	141.89	7.048	11.746	11.763	-0.2067	-0.2058	10/15
33.	142.34	7.025	12.309	12.324	-0.1696	-0.1689	10/07
34.	142.34	7.025	12.325	12.351	-0.2963	-0.2950	10/07
35.	142.43	7.021	12.464	12.485	-0.2374	-0.2363	10/10
36.	142.58	7.014	12.643	12.662	-0.2068	-0.2058	10/10
37.	142.62	7.012	12.705	12.721	-0.1784	-0.1776	10/07
38.	143.17	6.985	13.486	13.506	-0.2076	-0.2066	10/15
39.	143.63	6.962	14.192	14.213	-0.2103	-0.2092	10/07
40.	144.13	6.938	14.997	15.020	-0.2232	-0.2221	10/16

[continued]

No.	T (°K)	$10^3/T$ ($°K^{-1}$)	Vapor Pressure (torr) ^{12}C	Vapor Pressure (torr) ^{13}C	T ln(P'/P) (°K)	T $\ln(f_c/f_g)$ (°K)	Date (1980)
41.	144.25	6.932	15.184	15.207	-0.2206	-0.2195	10/16
42.	144.75	6.908	16.009	16.035	-0.2320	-0.2308	10/07
43.	145.34	6.880	17.044	17.073	-0.2499	-0.2485	10/16
44.	145.86	6.856	18.020	18.049	-0.2373	-0.2360	10/07
45.	146.40	6.831	19.067	19.101	-0.2627	-0.2612	10/16
46.	146.52	6.825	19.282	19.314	-0.2414	-0.2401	10/16
47.	146.95	6.805	20.168	20.203	-0.2583	-0.2568	10/07
48.	147.54	6.778	21.463	21.500	-0.2519	-0.2504	10/16
49.	148.04	6.755	22.617	22.656	-0.2560	-0.2544	10/07
50.	148.61	6.729	23.981	24.020	-0.2423	-0.2408	10/01
51.	149.34	6.696	25.829	25.873	-0.2544	-0.2527	10/16
52.	149.72	6.679	26.830	26.875	-0.2523	-0.2506	10/01
53.	150.82	6.630	29.925	29.977	-0.2648	-0.2629	10/01
54.	151.92	6.582	33.268	33.325	-0.2622	-0.2602	10/01
55.	153.02	6.535	36.973	37.039	-0.2731	-0.2709	10/01
56.	153.57	6.512	38.916	38.983	-0.2652	-0.2630	10/01
57.	154.15	6.487	41.079	41.153	-0.2751	-0.2727	10/01
58.	154.84	6.458	43.861	43.941	-0.2804	-0.2779	10/02
59.	155.44	6.433	46.309	46.392	-0.2789	-0.2764	10/08
60.	156.04	6.409	48.941	49.028	-0.2766	-0.2740	10/02

[continued]

No.	T (°K)	$10^3/T$ ($°K^{-1}$)	Vapor Pressure (torr) ^{12}C	Vapor Pressure (torr) ^{13}C	T ln(P'/P) (°K)	T $\ln(f_c/f_g)$ (°K)	Date (1980)
61.	156.66	6.383	51.749	51.847	-0.2960	-0.2931	10/08
62.	157.25	6.359	54.510	54.605	-0.2750	-0.2722	10/02
63.	157.87	6.334	57.583	57.693	-0.3015	-0.2983	10/08
64.	158.59	6.306	61.296	61.407	-0.2877	-0.2846	10/02
65.	159.85	6.256	68.431	68.554	-0.2883	-0.2850	10/02
66.	161.17	6.205	76.592	76.732	-0.2931	-0.2896	10/02
67.	162.48	6.155	85.398	85.555	-0.2976	-0.2937	10/02
68.	163.13	6.130	90.229	90.395	-0.3005	-0.2964	09/23
69.	163.75	6.107	94.953	95.128	-0.3014	-0.2972	10/02
70.	164.64	6.074	102.08	102.27	-0.2956	-0.2914	09/23
71.	165.17	6.054	106.33	106.53	-0.3037	-0.2992	09/24
72.	165.68	6.036	110.71	110.91	-0.2926	-0.2882	10/02
73.	166.20	6.017	115.39	115.60	-0.2992	-0.2946	09/23
74.	167.16	5.982	124.27	124.50	-0.3123	-0.3073	09/24
75.	167.37	5.975	126.33	126.56	-0.3076	-0.3026	10/02
76.	168.68	5.928	139.58	139.84	-0.3101	-0.3047	09/24
77.	169.47	5.901	148.28	148.56	-0.3212	-0.3154	10/08
78.	170.17	5.876	156.33	156.62	-0.3192	-0.3133	09/24
79.	170.98	5.849	165.91	166.22	-0.3148	-0.3088	10/08
80.	171.67	5.826	174.55	174.88	-0.3245	-0.3181	09/24

[continued]

No.	T (°K)	$10^3/T$ ($°K^{-1}$)	Vapor Pressure (torr) ^{12}C	Vapor Pressure (torr) ^{13}C	T ln(P'/P) (°K)	T $\ln(f_c/f_g)$ (°K)	Date (1980)
81.	173.17	5.775	194.54	194.91	-0.3263	-0.3194	09/24
82.	174.54	5.729	214.51	214.91	-0.3281	-0.3208	09/24
83.	174.88	5.718	219.71	220.12	-0.3307	-0.3232	09/24
84.	176.26	5.673	241.77	242.22	-0.3296	-0.3217	09/25
85.	177.95	5.620	271.47	271.97	-0.3282	-0.3198	09/25
86.	179.19	5.581	294.82	295.37	-0.3342	-0.3251	10/02
87.	179.65	5.566	304.04	304.61	-0.3391	-0.3298	09/25
88.	181.20	5.519	336.54	337.17	-0.3355	-0.3257	10/02
89.	181.37	5.514	340.22	340.87	-0.3451	-0.3349	09/25
90.	183.02	5.464	378.13	378.84	-0.3431	-0.3323	09/25
91.	184.16	5.430	405.96	406.73	-0.3491	-0.3376	09/25
92.	184.79	5.412	422.43	423.23	-0.3473	-0.3356	09/25
93.	185.89	5.380	451.82	452.68	-0.3519	-0.3396	09/25
94.	187.56	5.332	500.09	501.03	-0.3528	-0.3396	09/25
95.	188.54	5.304	529.75	530.74	-0.3523	-0.3386	10/08
96.	189.28	5.283	553.13	554.17	-0.3555	-0.3413	09/25
97.	190.24	5.257	585.35	586.45	-0.3574	-0.3426	10/09
98.	190.97	5.236	610.23	611.38	-0.3595	-0.3442	09/25
99.	192.75	5.188	675.43	676.72	-0.3661	-0.3496	09/25
100.	194.85	5.132	759.86	761.31	-0.3697	-0.3518	09/25

[continued]

No.	T (°K)	$10^3/T$ ($°K^{-1}$)	Vapor Pressure (torr) ^{12}C	Vapor Pressure (torr) ^{13}C	T ln(P'/P) (°K)	T $\ln(f_c/f_g)$ (°K)	Date (1980)
101.	196.17	5.098	815.82	817.33	-0.3614	-0.3430	10/02
102.	196.73	5.083	841.28	842.88	-0.3743	-0.3550	09/25
103.	197.97	5.051	898.80	900.47	-0.3688	-0.3489	10/02
104.	198.75	5.031	936.54	938.28	-0.3683	-0.3479	10/09
105.	199.95	5.001	998.05	999.91	-0.3722	-0.3507	10/02
106.	200.87	4.978	1046.8	1048.8	-0.3751	-0.3528	10/03
107.	201.97	4.951	1106.5	1108.6	-0.3791	-0.3558	10/03
108.	202.66	4.934	1145.5	1147.6	-0.3675	-0.3444	10/09
109.	202.85	4.930	1157.7	1159.9	-0.3853	-0.3610	10/03
110.	204.86	4.881	1279.5	1281.8	-0.3717	-0.3466	10/03
111.	205.57	4.865	1324.0	1326.5	-0.3794	-0.3533	10/09
112.	206.85	4.834	1408.7	1411.4	-0.3948	-0.3665	10/03
113.	207.75	4.813	1471.3	1474.1	-0.3968	-0.3676	10/09
114.	208.83	4.789	1547.9	1550.8	-0.3957	-0.3656	10/03
115.	209.85	4.765	1622.6	1625.8	-0.4109	-0.3787	10/09
116.	211.13	4.736	1724.4	1727.8	-0.4189	-0.3847	10/03

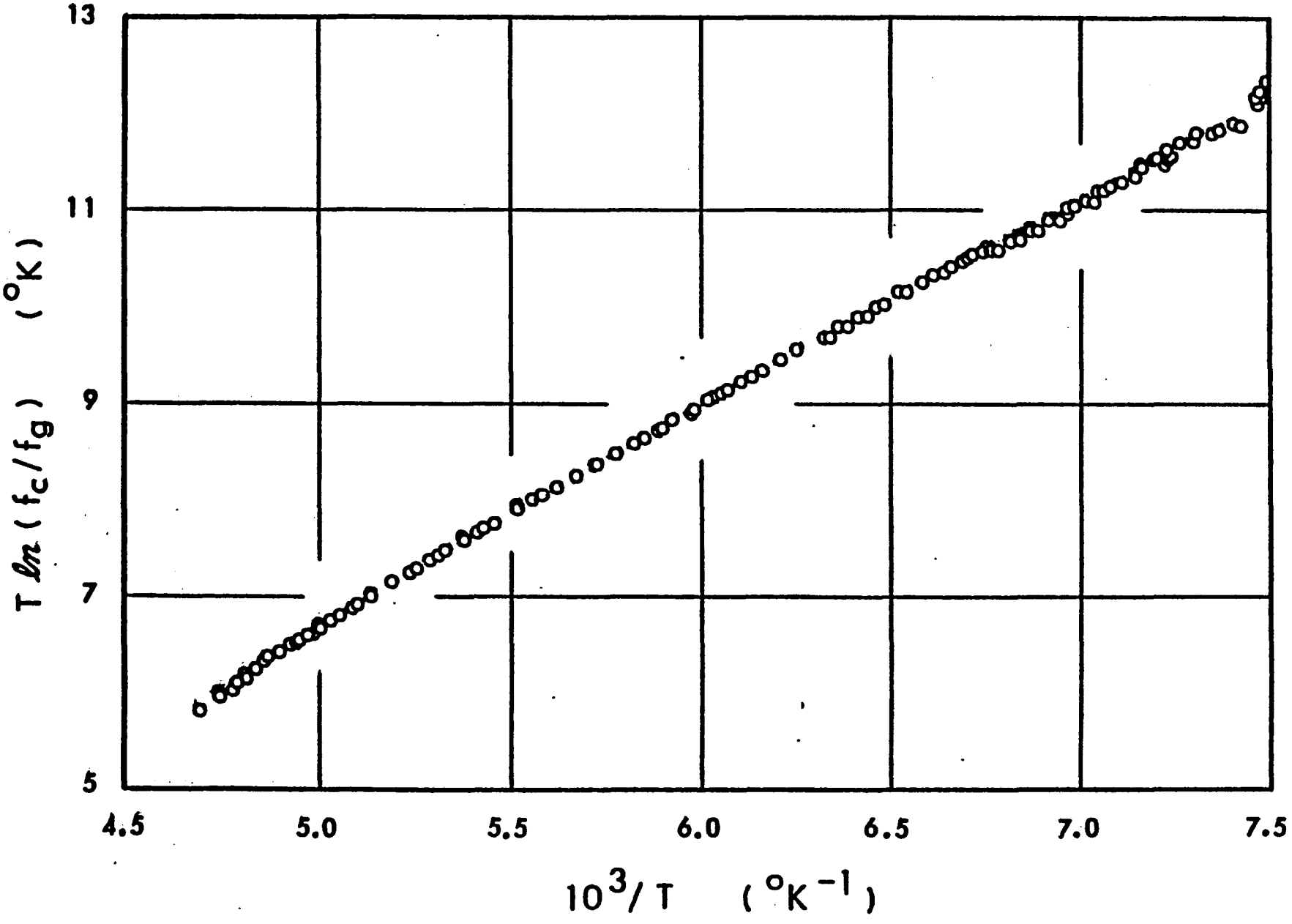

Figure 15. Vapor Pressure Isotope Effect; H/D-Effect: T $\ln(f_c/f_g)$ vs 1/T.

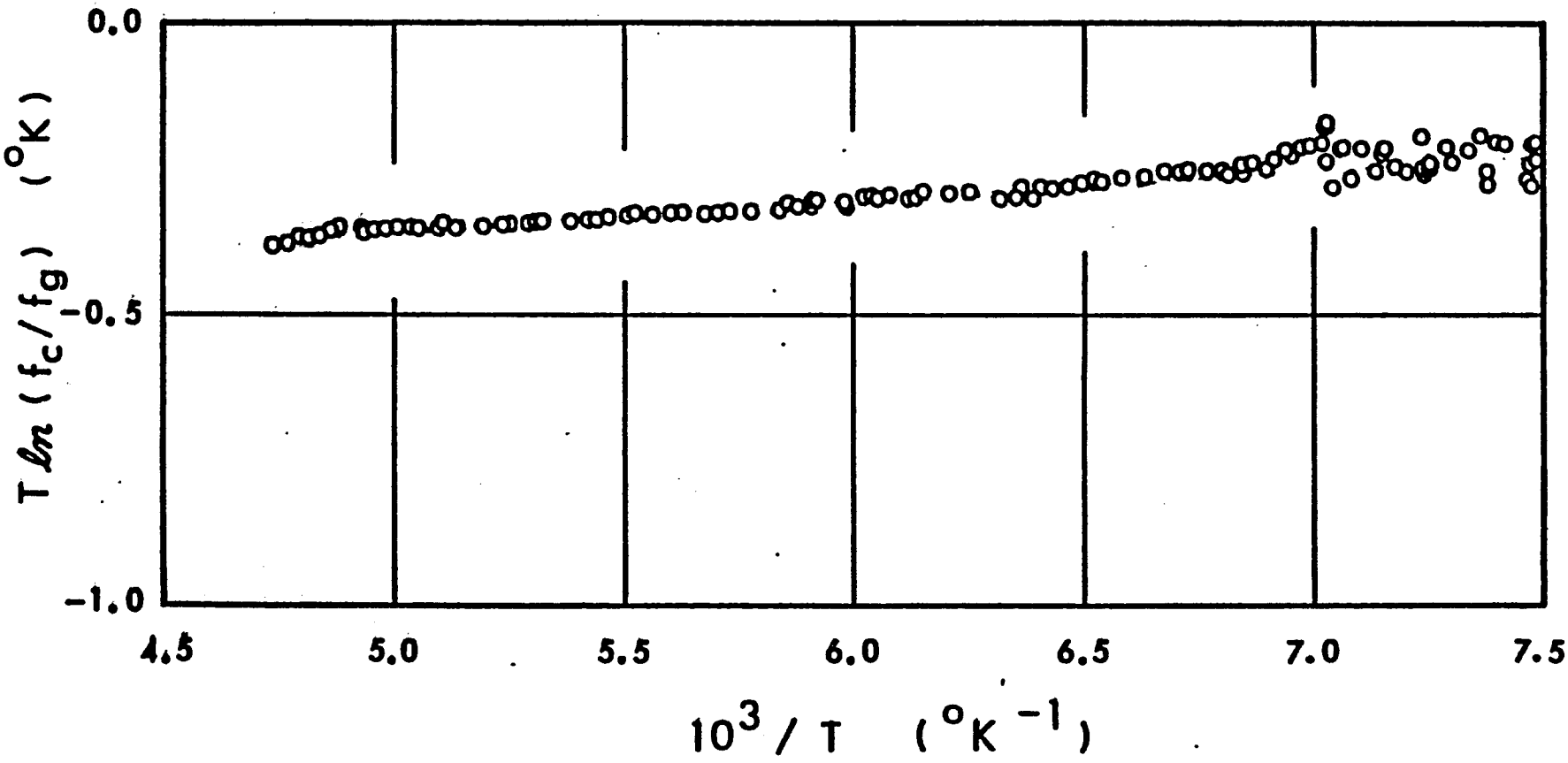

Figure 16. Vapor Pressure Isotope Effect; $^{12}C/^{13}C$-Effect: T $\ln(f_c/f_g)$ vs 1/T.

VI. DISCUSSION

In Chapter V, experimentally observed VPIE data was transformed into the reduced partition function ratio for the isotopic pairs $^{12}CH_3F/^{12}CD_3F$ and $^{12}CH_3F/^{13}CH_3F$.

In this section, a refinement made on Aldous and Mills gaseous $\underset{\sim}{F}$-matrix and construction of a liquid $\underset{\sim}{F}$-matrix which reproduces observed spectroscopic and reduced partition function ratio data will be presented. Analysis of this data reveals specific information relating to molecular structure and intermolecular forces in the liquid state.

VIA. Basis of Vibrational Analysis

The normal frequencies of vibration of any molecule can be obtained by knowing the equilibrium geometry and force field of the compound deduced from the best spectroscopic data available: Using Wilson's $\underset{\sim}{FG}$-matrix method,[35] we can determine the roots of the secular equation, λ_i, and consequently, the fundamental frequencies, ν_i, as $\sqrt{\lambda_i}/2\pi$.

The molecular geometry of methyl fluoride and atomic masses used to calculate the $\underset{\sim}{G}$-matrix are listed in Table 6.

All the published data on the $\underset{\sim}{F}$-matrix of methyl fluoride are

Table 6. Molecular Geometry[38,39] and Atomic Masses* of Methyl Fluoride

$r_{(C-H)} = 1.095$ Å	$\measuredangle_{(HCH)} = 110.33°$
$r_{(C-F)} = 1.386$ Å	$\measuredangle_{(HCF)} = 108.60°$
$m_H = 1.008145$ a.m.u.	$m_{^{12}C} = 12.003844$ a.m.u.
$m_D = 2.014741$ a.m.u.	$m_{^{13}C} = 13.007485$ a.m.u.

$m_F = 19.004444$ a.m.u.

---

*$m_{^{16}O} = 16.000000$ a.m.u.

based on a symmetry coordinate system.[36,37] In Figure 17 these coordinates are defined in terms of a set of internal valence coordinates. These symmetry coordinates were converted into an internal coordinate system (Figure 18) to facilitate the understanding of the interactions occurring in the molecule. The use of an internal valence coordinate system explicitly defines stretching and bending motions occurring between different atoms in a molecule. It gives the typical chemist a clearer picture of the interactions occurring and how they effect the force constants and vibrational frequencies.

VIB. $\underset{\sim}{F}$-Matrix of Gaseous Methyl Fluoride

VIB-1. Conversion of an $\underset{\sim}{F}$-Matrix in Symmetry Coordinates to One in Valence Coordinates

Aldous and Mills constructed an $\underset{\sim}{F}$-matrix for gaseous methyl fluoride in symmetry coordinates using existing vibrational and rotational spectra, vibrational frequencies, Coriolis zeta constants and centrifugal stretching constants. This was chosen as the preliminary $\underset{\sim}{F}$-matrix for this study. Previous work relating to methyl fluoride proved to be scarce and inconsistent. Edgell and Parts[40] used a modified valence force field to formulate the $\underset{\sim}{F}$-matrix of gaseous methyl fluoride, but their data was fitted to the fundamental frequencies of methyl fluoride-d_3 only. Pace[41] used a modified valence force field fitted for all fluoromethanes, resulting in large discrepancies in the calculated gaseous frequencies for methyl fluoride.

Figure 17. Symmetry Coordinates for Methyl Fluoride

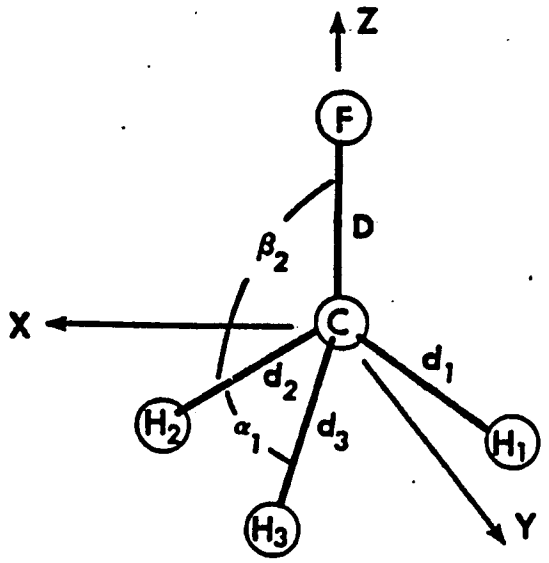

$$S_1 = (\Delta r_1 + \Delta r_2 + \Delta r_3)/\sqrt{3}$$
$$*S_{2a} = (\Delta\alpha_1 + \Delta\alpha_2 + \Delta\alpha_3 - \Delta\beta_1 - \Delta\beta_2 - \Delta\beta_3)/\sqrt{6}$$
$$*S_{2b} = (\Delta\alpha_1 + \Delta\alpha_2 + \Delta\alpha_3 + \Delta\beta_1 + \Delta\beta_2 + \Delta\beta_3)/\sqrt{6}$$
$$S_3 = \Delta R$$
$$S_4 = (2\Delta r_1 - \Delta r_2 - \Delta r_3/\sqrt{6}$$
$$S_5 = (\Delta r_2 - \Delta r_3)/\sqrt{2}$$
$$S_6 = (2\Delta\alpha_1 - \Delta\alpha_2 - \Delta\alpha_3)/\sqrt{6}$$
$$S_7 = (\Delta\alpha_2 - \Delta\alpha_3)/\sqrt{2}$$
$$S_8 = (2\Delta\beta_1 - \Delta\beta_2 - \Delta\beta_3)/\sqrt{6}$$
$$S_9 = (\Delta\beta_2 - \Delta\beta_3)/\sqrt{2}$$

*The redundancy in the A-class symmetry coordinates S_{2a} and S_{2b} may be removed by the orthonormal transformation:

$$S_2 = P \cdot S_{2a} - Q \cdot S_{2b} \text{ , where}$$
$$P = (1 + K)/(2 + 2K^2)^{1/2}$$
$$Q = (1 - K)/(2 + 2K^2)^{1/2}$$
$$K = -3 \sin\beta\cos\beta/\sin\alpha$$

Figure 18. Internal Coordinate Definition for Methyl Fluoride*

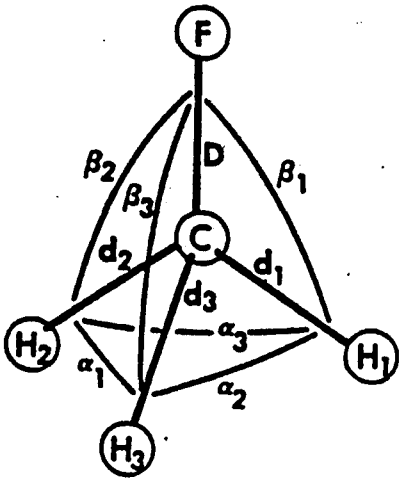

Coordinate Number	Symbol	Description
1	d_1	C-H_1 stretch
2	d_2	C-H_2 stretch
3	d_3	C-H_3 stretch
4	D	C-F stretch
5	$d_e\alpha_1$	d_e(H_2CH_3 bend)
6	$d_e\alpha_2$	d_e(H_1CH_3 bend)
7	$d_e\alpha_3$	d_e(H_1CH_2 bend)
8	$d_e\beta_1$	d_e(H_1CF bend)
9	$d_e\beta_2$	d_e(H_2CF bend)
10	$d_e\beta_3$	d_e(H_3CF bend)

*All bending coordinates are weighted by the equilibrium C-H bend length ($d_e = r_{(C-H)} = 1.095$ Å)

More recent work published by Russell, et al.[42] and Duncan, et al.[43] employed harmonic frequencies in the construction of the gaseous $\underset{\sim}{F}$-matrix. A second $\underset{\sim}{F}$-matrix for gaseous methyl fluoride was formulated by Aldous and Mills[3] using harmonic frequencies. There is considerable disagreement among the three papers due to the poor correlation which exists between the calculated harmonic frequencies. These differences are due in principle to the interpretation of the effects of anharmonicity. Because the molecular spectra of liquid methyl fluoride are discussed only in terms of the fundamentals and not in terms of the harmonic or the zeroeth order frequencies, the gaseous $\underset{\sim}{F}$-matrix of Aldous and Mills[3] based on the observed fundamental frequencies was selected as a starting point. The molecular spectra of gaseous methyl fluoride has been analyzed by several authors,[38,40,43-48] and a set of reproducible, fundamental frequencies has been observed for the molecule.

The gaseous $\underset{\sim}{F}$-matrix of Aldous and Mills[3] is summarized in Table 7 using symmetry coordinates. The calculated frequencies of Aldous and Mills are compared to experimentally observed fundamental frequencies for carbon-12, carbon-13, and deuterated methyl fluoride in Table 8. Although several calculated frequencies correlated well with observed values, large differences are evident in many others.

As a first step in an attempt to improve on the preliminary gaseous $\underset{\sim}{F}$-matrix of Aldous and Mills, the symmetry force constants were converted into an internal coordinate system by means of a transformation matrix. Using matrix algebra, the conversion can be

Table 7. Symmetry Coordinate Force Constants* for Methyl Fluoride[3] Using Observed Frequencies

Notation	Value
F_{11}	4.81
F_{12}	-0.40
F_{13}	+0.72
F_{22}	0.646
F_{23}	-0.622
F_{33}	5.672
F_{44}	4.948
F_{45}	-0.108
F_{46}	0.217
F_{55}	0.470
F_{56}	-0.060
F_{66}	0.722

*Units are (mdyne/Å) throughout, all angle bending coordinates being scaled by the equilibrium C-H bend length.

Table 8. Fundamental Frequencies of Gaseous Methyl Fluoride

Molecule	Mode	Experimental			Calculated
		Duncan[43]	Clark[47]	Andersen[38]	Mills[3]
$^{12}CH_3F$	ν_1	2910.0*	2965.3	2964.4	2924.7*
	ν_2	1460.4	1460.1	(1464)	1469.4
	ν_3	1048.6	1047.9	1046.0	1059.6
	ν_4	3006.2	3006.8	3006.1	3028.4
	ν_5	1467.8	1468.1	1466.6	1468.7
	ν_6	1182.3	1181.9	1180.8	1178.7
$^{12}CD_3F$	ν_1	2110.0*	-	2089.4	2112.8*
	ν_2	1134.8	-	1135.0	1131.5
	ν_3	992.3	-	987.0	994.5
	ν_4	2258.5	-	2258.3	2243.9
	ν_5	1071.3	-	1071.1	1069.9
	ν_6	911.3	-	910.1	901.8
$^{13}CH_3F$	ν_1	2906.0*	2960.0	-	2920.4*
	ν_2	1455.0	1454.4	-	1463.9
	ν_3	1027.5	1026.2	-	1038.2
	ν_4	2995.7	2995.0	-	3017.5
	ν_5	1465.4	1465.0	-	1465.7
	ν_6	1174.5	1173.9	-	1171.0

*ν_1 Fundamental Frequency corrected for Fermi resonance between ν_1 and $2\nu_5$

expressed as

$$\underset{\sim}{F}_1 = \underset{\sim}{T}^T \underset{\sim}{F}_2 \underset{\sim}{T} \qquad (33)$$

where $\underset{\sim}{F}_1$ and $\underset{\sim}{F}_2$ are the $\underset{\sim}{F}$-matrices in internal and symmetry coordinates, respectively, and $\underset{\sim}{T}$ and $\underset{\sim}{T}^T$ are the transformation matrix and its transpose. The transformation matrix, $\underset{\sim}{T}$ is listed in Table 9. The conversions of $\underset{\sim}{F}$-matrix elements from symmetry to internal coordinates are tabulated in Table 10, and the resulting preliminary gaseous $\underset{\sim}{F}$-matrix in internal coordinates is summarized in Table 11.

VIB-2. Corrections of Observed Fundamentals for Fermi Resonance

A Fermi resonance occurs between vibrational eigenstates possessing the same symmetry and approximately equal eigenvalues. In gaseous methyl fluoride a strong Fermi resonance exists between ν_1° and $2\nu_5^\circ$, which results in the observed fundamental frequencies of $\nu_1 = 2964$ cm^{-1} and $2\nu_5 = 2863$ cm^{-1}. According to Aldous and Mills,[3] this corresponds to the unperturbed frequency of $\nu_1^\circ = 2930$ cm^{-1}.

In 1972, Duncan, et al.[43] studied the infra-red spectra of crystalline $^{12}CH_3F$ and $^{13}CH_3F$, which revealed that not only ν_1° and $2\nu_5^\circ$ but also $2\nu_2^\circ$ enter into a Fermi resonance triad. Their observed frequencies were 2965.2, 2908.8 and 2863.2 cm^{-1} for ν_1, $2\nu_2$, and $2\nu_5$, respectively. However, the value of 2908.8 cm^{-1} for $2\nu_2$ was a tentative figure, due to the fact that it was observed in the solid phase only. The frequencies for ν_1 and $2\nu_5$ were identified in the gaseous phase.

Table 9. Transformation Matrix for Methyl Fluoride

$\underset{\sim}{T}$	1 r_1	2 r_2	3 r_3	4 R	5 $r_e\alpha_1$	6 $r_e\alpha_2$	7 $r_e\alpha_3$	8 $r_e\beta_1$	9 $r_e\beta_2$	10 $r_e\beta_3$
S_1	$\frac{1}{\sqrt{3}}$	$\frac{1}{\sqrt{2}}$	$\frac{1}{\sqrt{3}}$							
S_2					A	A	A	B	B	B
S_3				1						
S_{4x}	$\frac{2}{\sqrt{6}}$	$\frac{-1}{\sqrt{6}}$	$\frac{-1}{\sqrt{6}}$							
S_{5x}					$\frac{2}{\sqrt{6}}$	$\frac{-1}{\sqrt{6}}$	$\frac{-1}{\sqrt{6}}$			
S_{6x}								$\frac{2}{\sqrt{6}}$	$\frac{-1}{\sqrt{6}}$	$\frac{-1}{\sqrt{6}}$
S_{4y}		$\frac{1}{\sqrt{2}}$	$\frac{-1}{\sqrt{2}}$							
S_{5y}						$\frac{1}{\sqrt{2}}$	$\frac{-1}{\sqrt{2}}$			
S_{6y}									$\frac{1}{\sqrt{2}}$	$\frac{-1}{\sqrt{2}}$

$$A = \frac{P-Q}{\sqrt{6}(P^2+Q^2)^{\frac{1}{2}}} \; ; \quad B = \frac{-(P+Q)}{\sqrt{6}(P^2+Q^2)^{\frac{1}{2}}} \qquad P = \frac{(1+K)}{(2+2K^2)^{1/2}} \qquad Q = \frac{(1-K)}{(2+2K^2)^{1/2}}$$

$$K = -3 \sin\beta \cos\beta / \sin\alpha$$

Table 10. F-Matrix Elements in Internal Coordinates Expressed in Terms of the Elements in Symmetry Coordinates

$$f_d = \frac{1}{3} F_{11} + \frac{2}{3} F_{44}$$

$$f_{dd} = \frac{1}{3} F_{11} - \frac{1}{3} F_{44}$$

$$f_{dD} = \frac{1}{\sqrt{3}} F_{13}$$

$$f_D = F_{33}$$

$$f_{D\alpha} = AF_{23}$$

$$f_{D\beta} = BF_{23}$$

$$f'_{d\alpha} = \frac{A}{\sqrt{3}} \cdot F_{12} + \frac{2}{3} F_{45}$$

$$f_{d\alpha} = \frac{A}{\sqrt{3}} \cdot F_{12} - \frac{1}{3} F_{45}$$

$$f'_{d\beta} = \frac{B}{\sqrt{3}} \cdot F_{12} + \frac{2}{3} F_{46}$$

$$f_{d\beta} = \frac{B}{\sqrt{3}} \cdot F_{12} - \frac{1}{3} F_{46}$$

$$f_\alpha = A^2 F_{22} + \frac{2}{3} F_{55}$$

$$f'_{\alpha\alpha} = A^2 F_{22} - \frac{1}{3} F_{55}$$

$$f_\beta = B^2 F_{22} + \frac{2}{3} F_{66}$$

$$f'_{\beta\beta} = B^2 F_{22} - \frac{1}{3} F_{66}$$

$$f'_{\alpha\beta} = ABF_{22} + \frac{2}{3} F_{56}$$

$$f_{\alpha\beta} = ABF_{22} - \frac{1}{3} F_{56}$$

Table 11. $\underset{\sim}{F}$-Matrix* of Gaseous Methyl Fluoride Obtained by Conversion of Aldous and Mills' $\underset{\sim}{F}$-Matrix

Diagonals			Off-Diagonals	
Description	Notation	Value (mdyne/Å)	Notation	Value (mdyne/Å)
C-H stretch	f_d	4.902	f_{dd}	-0.046
C-F stretch	f_D	5.672	f_{dD}	0.416
HCH bend	f_α	0.417	$f'_{d\alpha}$	-0.165
HCF bend	f_β	0.593	$f_{d\alpha}$	-0.057
			$f_{D\alpha}$	-0.250
			$f'_{\alpha\alpha}$	-0.053
			$f'_{d\beta}$	0.241
			$f_{d\beta}$	0.024
			$f_{D\beta}$	0.258
			$f'_{\alpha\beta}$	-0.148
			$f_{\alpha\beta}$	-0.088
			$f'_{\beta\beta}$	-0.129

*An $\underset{\sim}{F}$-matrix element with one subscript is a diagonal element, and one with two subscripts is an off-diagonal element. When two off-diagonals are listed for a similar interaction, e.g. $f'_{d\alpha}$ and $f_{d\alpha}$, the one with the prime refers to the interaction between two coordinates not sharing a common C-H bond, and the one without a prime refers to the interaction between two coordinates which share a common C-H bond.

Approximate calculations were performed by Duncan[43] in an attempt to reproduce the gas phase frequencies of the two observed components, ν_1 and $2\nu_5$, and the crystalline $2\nu_2$ frequency. The gas phase frequency for $2\nu_2$ is not known, but is expected to be somewhat higher than the value in the crystalline state. Fairly accurate values are known for the unperturbed vibrational frequencies of $2\nu_2^\circ$ and $2\nu_5^\circ$. The unknowns are the unperturbed vibrational frequency for ν_1°, and the Fermi resonance interaction constants. According to first-order perturbation theory, a 3x3 interaction matrix is given by

$$\begin{array}{ccc} |\nu_5 = 2^\circ\rangle & |\nu_2 = 2\rangle & |\nu_1 = 1\rangle \\ \begin{bmatrix} 2\nu_5^\circ & W_{2255} & W_{155} \\ W_{2255} & 2\nu_2^\circ & W_{122} \\ W_{115} & W_{122} & \nu_1^\circ \end{bmatrix} & & \end{array}$$

where W_{2255} is the second order resonance parameter and W_{155} and W_{122} are the interaction parameters between ν_1 and ν_5, and ν_1 and ν_2, respectively. The overtone bands for $2\nu_5^\circ$ and $2\nu_2^\circ$ are listed as 2920.0 and 2910.0, respectively, according to Duncan's[43] observations. The second order resonance parameter, W_{2255}, was constrained to a value of zero by Duncan as a first order approximation. His calculations on W_{155} and W_{122} produced values of 45 and 25 cm^{-1}, respectively. These values were used in the 3x3 interaction matrix to solve for the only remaining unknown, ν_1°. Table 12 lists the interaction matrix for $^{12}CH_3F$ and gives a comparison of the experimentally observed fundamental frequencies against the frequencies calculated by using the 3x3 secular determinant. The calculated frequencies agree very

Table 12. Reproduction of Perturbed Frequencies for ν_1, $2\nu_2$, and $2\nu_5$ due to Fermi Resonance for Gaseous $^{12}CH_3F^{43}$

Interaction Matrix

$\lvert\nu_5 = 2^e\rangle$	$\lvert\nu_2 = 2\rangle$	$\lvert\nu_1 = 1\rangle$
2920.0	0.0	45.0
0.0	2910.0	25.0
45.0	25.0	2910.0

	Perturbed Frequencies (cm^{-1})		
	$\nu_{OBSERVED}$	$\nu_{CALCULATED}$	$\Delta\nu$ ($\nu_{OBS}-\nu_{CALC}$)
ν_1	2965.2	2965.8	-0.6
$2\nu_2$	2908.8*	2912.0	-3.2
$2\nu_5$	2863.2	2862.2	1.0

*$2\nu_2$ observed in the solid phase only.

well with the observed fundamentals, and the value of 2910.0 cm^{-1} is predicted for the unperturbed ν_1° frequency. Duncan's[43] value for the unperturbed ν_1° (2910.0 cm^{-1}) is considerably different from the previously accepted value of 2930.0 cm^{-1} (Aldous and Mills[3]), but his work in the crystalline phase (on $2\nu_2$) has been confirmed by Blanchard[47] and Chao[4] in recent years. An identical procedure was followed by Duncan in determining the unperturbed ν_1° frequency in $^{13}CH_3F$. The unperturbed frequencies for $2\nu_2^\circ$ and $2\nu_5^\circ$ have been deduced, and Fermi resonance interaction parameters were calculated. Table 13 shows the interaction matrix for $^{13}CH_3F$, and Duncan predicts an unperturbed ν_1° frequency of 2906.0 cm^{-1}.

Following a procedure analogous to that of Duncan's, an interaction matrix was set up for $^{12}CD_3F$ by this investigator. No evidence was found linking a third peak into a Fermi resonance triad, so a 2x2 secular determinant was solved. The fundamental frequency, ν_5, has an

$$\begin{array}{cc} |\nu_5 = 2^\circ\rangle & |\nu_1 = 1\rangle \\ \begin{bmatrix} 2\nu_5^\circ & W_{155} \\ W_{155} & \nu_1^\circ \end{bmatrix} & \end{array}$$

observed value of 1071 cm^{-1}. The $2\nu_5^\circ$ overtone band would be expected to have a value between 2125 and 2135 cm^{-1}, accounting for a small anharmonicity effect. Aldous and Mills[3] assigned a value of 2110 cm^{-1} for the unperturbed ν_1° frequency.

Substitution of these values into the 2x2 interaction matrix predicted an exact value of 2131.0 cm^{-1} for the unperturbed $2\nu_5^\circ$ and a value of 27.5 cm^{-1} for the Fermi resonance interaction parameter W_{155}.

Table 13. Reproduction of Perturbed Frequencies for ν_1, $2\nu_2$, and $2\nu_5$ due to Fermi Resonance for Gaseous $^{13}CH_3F^{43}$

Interaction Matrix

	$\lvert\nu_5 = 2^e\rangle$	$\lvert\nu_2 = 2\rangle$	$\lvert\nu_1 = 1\rangle$
	2915.0	0.0	43.5
	0.0	2900.0	25.0
	43.5	25.0	2906.0

	Perturbed Frequencies (cm^{-1})		
	$\nu_{OBSERVED}$	$\nu_{CALCULATED}$	$\Delta\nu$ ($\nu_{OBS}-\nu_{CALC}$)
ν_1	2958.4	2959.5	-1.1
$2\nu_2$	2900.9*	2903.4	-2.5
$2\nu_5$	2859.0	2858.3	0.7

*$2\nu_2$ observed in the solid phase only.

The calculated frequencies produced by the interaction matrix from this study were within ±0.5 cm^{-1} of previously published experimental data.[4]

The preliminary $\underset{\sim}{F}$-matrix for gaseous methyl fluoride was based upon Aldous and Mills'[3] value of ν_1° = 2930 cm^{-1}. In light of Duncan's[43] recent work, modifications and refinements were performed to improve upon the existing preliminary gaseous force constants.

VIB-3. Refinement of Gaseous $\underset{\sim}{F}$-Matrix in Valence Coordinates

To facilitate modifications on Aldous and Mills'[3] preliminary $\underset{\sim}{F}$-matrix, a computer program called 9042D (obtained as a modification of the Schachtschneider-Snyder[50] programs) was used. This program enables the user to calculate the difference in frequencies after applying a specific change to any individual $\underset{\sim}{F}$-matrix element. Any $\underset{\sim}{F}$-matrix element can be varied by 0.001, 0.01, or 0.1 mdyne/Å, or by units of 0.1 or 1%. These modifications can be applied in any combination to any $\underset{\sim}{F}$-matrix element. For convenience, the effect of a 1% change on each $\underset{\sim}{F}$-matrix elements was chosen as an initial starting point. The computer program (9042D) lists the initial frequencies ($\nu_1 \sim \nu_6$), and then computes the effect of a 1% modification on each $\underset{\sim}{F}$-matrix element, printing a second series of modified, $\nu_1 \sim \nu_6$ frequencies. A first derivative table was calculated for each of 16 elements contained in the $\underset{\sim}{F}$-matrix of methyl fluoride, and is summarized in Table 14. For each $\underset{\sim}{F}$-matrix element, the initial force constant value is listed along with a pair of differential changes

Table 14. Differential Effects of +1% Change in f_{ij} in Mills' $\underset{\sim}{F}$-Matrix for Gaseous Methyl Fluoride

Notation	Initial Value (mdyn/Å)	Molecule	Differentials (cm^{-1}) ν_1	ν_2	ν_3	ν_4	ν_5	ν_6
f_d	4.902	$^{12}CH_3F$	[-14.02]	-0.82	-0.03	[-15.12]	0.00	-0.04
		$^{12}CD_3F$	[-9.86]	-0.51	-0.26	[-11.26]	0.00	-0.01
f_D	5.672	$^{12}CH_3F$	-0.04	[-0.20]	[-5.78]	0.00	0.00	0.00
		$^{12}CD_3F$	-0.15	[-2.95]	[-2.90]	0.00	0.00	0.00
f_α	0.417	$^{12}CH_3F$	-0.08	[-2.56]	-0.04	-0.02	[-6.50]	-0.07
		$^{12}CD_3F$	-0.11	[-1.61]	-0.33	-0.08	[-4.72]	-0.04
f_β	0.593	$^{12}CH_3F$	-0.11	[-3.89]	-0.06	-0.02	-0.28	[-4.71]
		$^{12}CD_3F$	-0.17	[-2.45]	-0.50	-0.06	0.00	[-3.76]
f_{dd}	-0.046	$^{12}CH_3F$	0.26	0.02	0.00	-0.14	0.00	0.00
		$^{12}CD_3F$	0.19	0.01	0.01	-0.11	0.00	0.00
f_{dD}	0.416	$^{12}CH_3F$	0.21	-0.11	0.12	0.00	0.00	0.00
		$^{12}CD_3F$	0.33	-0.34	0.24	0.00	0.00	0.00
$f'_{d\alpha}$	-0.165	$^{12}CH_3F$	-0.24	0.34	-0.01	0.14	0.02	0.01
		$^{12}CD_3F$	-0.24	0.21	0.07	0.22	-0.03	0.02
$f_{d\alpha}$	-0.057	$^{12}CH_3F$	-0.16	0.23	-0.01	-0.05	-0.01	0.00
		$^{12}CD_3F$	-0.17	0.15	0.05	-0.08	0.01	0.00

[continued]

[Table 14; continued]

Notation	Initial Value (mdyn/Å)	Molecule	Differentials (cm^{-1}) ν_1	ν_2	ν_3	ν_4	ν_5	ν_6
$f_{D\alpha}$	-0.250	$^{12}CH_3F$	0.03	[0.40	[0.28	0.00	0.00	0.00
		$^{12}CD_3F$	0.07	1.22]	-0.56]	0.00	0.00	0.00
$f'_{\alpha\alpha}$	-0.053	$^{12}CH_3F$	0.02	0.65	0.01	0.00	-0.83	-0.01
		$^{12}CD_3F$	0.03	0.41	0.09	-0.01	-0.60	-0.01
$f'_{d\beta}$	0.241	$^{12}CH_3F$	-0.36	0.51	-0.01	0.13	0.00	0.12
		$^{12}CD_3F$	-0.37	0.32	0.10	0.23	0.00	0.04
$f_{d\beta}$	0.024	$^{12}CH_3F$	-0.07	0.10	0.00	-0.01	0.00	-0.01
		$^{12}CD_3F$	-0.07	0.06	0.02	-0.02	0.00	0.00
$f_{D\beta}$	0.258	$^{12}CH_3F$	0.03	0.42	0.30	0.00	0.00	0.00
		$^{12}CD_3F$	0.08	1.30	-0.60	0.00	0.00	0.00
$f'_{\alpha\beta}$	-0.148	$^{12}CH_3F$	-0.06	[-1.88	-0.03	-0.01	0.79	[-0.33
		$^{12}CD_3F$	-0.08	-1.18]	-0.24	-0.04	0.00	0.25]
$f_{\alpha\beta}$	-0.088	$^{12}CH_3F$	-0.07	[-2.24	-0.04	0.01	-0.48	0.21
		$^{12}CD_3F$	-0.10	-1.41]	-0.29	0.02	-0.01	-0.14
$f'_{\beta\beta}$	-0.129	$^{12}CH_3F$	0.05	[1.70	0.03	0.00	-0.06	[-1.03
		$^{12}CD_3F$	0.07	1.06]	0.22	-0.01	0.00	-0.82]

in frequency, corresponding to the changes in $^{12}CH_3F$ and $^{12}CD_3F$. The blocked off areas are the frequencies most directly affected by a 1% change in the particular $\underset{\sim}{F}$-matrix element, and this visually makes it easier to perform modifications on the existing $\underset{\sim}{F}$-matrix.

After a series of extensive modifications to Aldous and Mills' $\underset{\sim}{F}$-matrix,[3] a newly formulated gaseous $\underset{\sim}{F}$-matrix was produced. The final $\underset{\sim}{F}$-matrix for gaseous methyl fluoride is summarized in Table 15. The fundamental frequencies calculated from the final $\underset{\sim}{F}$-matrix are compared to the calculated results of the preliminary $\underset{\sim}{F}$-matrix and the best set of observed frequencies. These results are tabulated in Table 16. A significant improvement can be seen in the calculated frequencies from the final $\underset{\sim}{F}$-matrix of gaseous methyl fluoride. The ν_1 frequency corrected for Fermi resonance compares very well with experimental data for all these isotopic species. The last column lists the calculated frequencies to three decimal places in order to provide reproducibility in isotope effect calculations to the appropriate precision.

VIC. $\underset{\sim}{F}$-Matrix for Liquid Methyl Fluoride

VIC-1. Initial Liquid $\underset{\sim}{F}$-Matrix

The fundamental frequencies of liquid $^{12}CH_3F$ and $^{12}CD_3F$ were studied using Raman spectroscopy by Chao and Eggers,[4] and some additional unpublished work was performed by Griffiths[5] on $^{12}CH_3F$. A preliminary liquid $\underset{\sim}{F}$-matrix was constructed by modifying the

Table 15. Final F-Matrix of Gaseous Methyl Fluoride*

Diagonals			Off-Diagonals	
Description	Notation	Value (mdyne/Å)	Notation	Value (mdyne/Å)
C-H stretch	f_d	4.685	f_{dd}	-0.035
C-F stretch	f_D	5.582	f_{dD}	0.502
HCH bend	f_α	0.401	$f'_{d\alpha}$	-0.125
HCF bend	f_β	0.619	$f_{d\alpha}$	-0.225
			$f_{D\alpha}$	-0.250
			$f'_{\alpha\alpha}$	-0.054
			$f'_{d\beta}$	0.015
			$f_{d\beta}$	0.118
			$f_{D\beta}$	0.258
			$f'_{\alpha\beta}$	-0.143
			$f_{\alpha\beta}$	-0.119
			$f'_{\beta\beta}$	-0.144

*See footnote of Table 11 for internal coordinate definitions.

Table 16. Comparison of Fundamental Frequencies of Gaseous Methyl Fluoride

Molecule	Mode	Experimental (cm^{-1}) (Observed)[a]	Calculated (cm^{-1}) (Mills)[3]	Calculated (cm^{-1}) (This work)[b]
$^{12}CH_3F$	ν_1 (A_1)	2910.0*	2924.7*	2909.988*
	ν_2 (A_1)	1460	1469.4	1460.825
	ν_3 (A_1)	1049	1059.6	1049.301
	ν_4 (E)	3006	3028.4	3005.984
	ν_5 (E)	1467	1468.7	1469.574
	ν_6 (E)	1182	1178.7	1183.309
$^{12}CD_3F$	ν_1 (A_1)	2110.0*	2112.8*	2112.089*
	ν_2 (A_1)	1135	1131.5	1129.361
	ν_3 (A_1)	992	994.5	976.358
	ν_4 (E)	2259	2243.9	2258.268
	ν_5 (E)	1071	1069.9	1050.116
	ν_6 (E)	911	901.8	910.281
$^{13}CH_3F$	ν_1 (A_1)	2906.0*	2920.4*	2904.768*
	ν_2 (A_1)	1455	1463.9	1454.922
	ν_3 (A_1)	1027	1038.2	1028.757
	ν_4 (E)	2995	3017.5	2991.625
	ν_5 (E)	1465	1465.7	1468.666
	ν_6 (E)	1174	1171.0	1175.346

*ν_1 corrected for Fermi resonance.

(a) consensus of best values from several authors[38,40,43-48]

(b) calculated by using F-matrix of Table 15

existing final gaseous $\underset{\sim}{F}$-matrix and introducing very small translational and rotational force constants for the lattice oscillations. The preliminary liquid $\underset{\sim}{F}$-matrix is listed in Table 17.

This newly formulated liquid $\underset{\sim}{F}$-matrix required considerable modification because it does not account for the Fermi resonance corrections on the ν_1 fundamental frequency. The observed fundamental frequencies of Chao and Eggers[4] were used, and a 2x2 interaction matrix analogous to gaseous $^{12}CD_3F$ was solved. Although a Fermi resonance triad between ν_1, $2\nu_2$, and $2\nu_5$ is expected, no experimental data could confirm its existence. The 2x2 determinant was used in order to reduce the number of unknown parameters. Table 18 illustrates the 2x2 interaction matrix and compares the experimentally observed frequencies with those calculated by this investigator using the determinant. In the case of liquid $^{12}CH_3F$, the observed value of the $2\nu_5$ overtone band remained unchanged from the observed gaseous frequency. The unperturbed $2\nu_5^\circ$ frequency (for the liquid) was therefore given a value of 2920.0 cm^{-1}. The observed ν_1 frequency was shifted up approximately by 7 cm^{-1} upon condensation,[4] and a similar change was anticipated for the unperturbed ν_1° frequency in the liquid. The Fermi resonance interaction constant, W_{155}, was calculated in the gaseous state (by Duncan[43]) and found to have a value of 45.0 cm^{-1}. Because no calculations have been previously performed in the condensed state, this value was used as a first approximation in the 2x2 interaction matrix for liquid methyl fluoride. Substitution of this data into the 2x2 determinant produced an unperturbed ν_1° frequency of 2915.0 cm^{-1} for this study. The Fermi resonance interaction parameter, W_{155}, had a value of

Table 17. Preliminary $\underset{\sim}{F}$-Matrix of Liquid Methyl Fluoride*

Diagonals[(a)]			Off-Diagonals	
Description	Notation	Value (mdyne/Å)	Notation	Value (mdyne/Å)
C-H stretch	f_d	4.788	f_{dd}	-0.035
C-F stretch	f_D	5.072	f_{Dd}	0.512
HCH bend	f_α	0.417	$f'_{d\alpha}$	-0.125
HCF bend	f_β	0.603	$f_{d\alpha}$	-0.185
			$f_{D\alpha}$	-0.250
			$f'_{\alpha\alpha}$	-0.056
Translation	f_{T_x}	0.01	$f'_{d\beta}$	0.021
	f_{T_y}	0.01	$f_{d\beta}$	0.094
	f_{T_z}	0.01	$f_{D\beta}$	0.258
Rotation	f_{R_x}[(b)]	0.01	$f'_{\alpha\beta}$	-0.138
	f_{R_y}	0.01	$f_{\alpha\beta}$	-0.111
	f_{R_z}	0.01	$f'_{\beta\beta}$	-0.144

*This work

(a) For definition of internal coordinates, see Figure 18 and footnote of Table 11.

(b) All $\underset{\sim}{F}$-matrix elements are in units of mdyne/Å, except f_R, which are in units of mdyne Å.

Table 18. Reproduction of Perturbed Frequencies for ν_1 and $2\nu_5$ due to Fermi Resonance (Liquid Phase)

Interaction Matrix

$$\begin{array}{cc} |\nu_5 = 2^\circ\rangle & |\nu_1 = 1\rangle \\ \begin{bmatrix} 2\nu_5^\circ & W_{155} \\ W_{155} & \nu_1^\circ \end{bmatrix} & \end{array}$$

	$^{12}CH_3F$ (cm^{-1})				$^{12}CD_3F$ (cm^{-1})		
	$\nu^\circ_{unperturbed}$ *	$\nu_{observed}$ [4]	$\nu_{calculated}$ *		$\nu^\circ_{unperturbed}$ *	$\nu_{observed}$ [4]	$\nu_{calculated}$ *
ν_1	2915.0	2971	2971.1	ν_1	2107.0	2145	2145.0
$2\nu_5$	2920.0	2864	2863.9	$2\nu_5$	2126.5	2088	2088.5

*This work

43.5 cm^{-1} after refinement. The observed frequencies[4] compared very well with this study's calculated results from the 2x2 interaction matrix.

The same procedure was followed for $^{12}CD_3F$, and the unperturbed frequency, ν_1°, found was 2107.0 cm^{-1}. Once again, experimental[4] and calculated results compared very well. At present, no experimental data exists for liquid $^{13}CH_3F$.

The fundamental frequencies calculated from the preliminary liquid $\underset{\sim}{F}$-matrix of Table 17 are summarized and compared with the experimental liquid frequencies in Table 19. The agreement between the calculated and experimental frequencies is fair, but a further refinement without taking into account the VPIE data is unwarranted.

VIC-2. Refinement of Liquid $\underset{\sim}{F}$-Matrix.

In the gaseous $\underset{\sim}{F}$-matrix, refinements were implemented by modifying the values of the internal force constants until the calculated frequencies agreed with the experimentally observed frequencies. In the case of the liquid $\underset{\sim}{F}$-matrix, similar steps were performed. The solution for the liquid $\underset{\sim}{F}$-matrix, however, is far more complicated. In addition to the six fundamental liquid frequencies, a pair of translational and a pair of rotational frequencies are introduced. There is only a limited amount of information available on the external frequencies,[51] and these results are presented in the solid phase only. The liquid $\underset{\sim}{F}$-matrix presented in Table 17 is only a zeroeth order approximation of the liquid force constants. At this

Table 19. Fundamental Frequencies of Liquid Methyl Fluorides

Molecule	Mode	Experimental (cm^{-1}) Chao	Experimental (cm^{-1}) Griffiths	Calculated (cm^{-1}) (This work)
$^{12}CH_3F$	ν_1 (A_1)	2915*	2912*	2916*
	ν_2 (A_1)	-	1456	1466
	ν_3 (A_1)	990	993.1	995
	ν_4 (E)	3030	3021.3	3030
	ν_5 (E)	1468	1491 (?)	1493
	ν_6 (E)	1180	1179	1181
$^{12}CD_3F$	ν_1 (A_1)	2107*		2109*
	ν_2 (A_1)	1112		1111
	ν_3 (A_1)	959		948
	ν_4 (E)	2272		2271
	ν_5 (E)	1073		1071
	ν_6 (E)	909		910
$^{13}CH_3F$	ν_1 (A_1)			2911*
	ν_2 (A_1)			1461
	ν_3 (A_1)			975
	ν_4 (E)			3016
	ν_5 (E)			1492
	ν_6 (E)			1173

*ν_1 frequency corrected for Fermi resonance

time, no attempt has been made to correlate the external frequencies calculated from this liquid $\underset{\sim}{F}$-matrix to experimentally observed external frequency data. Before attempting this aspect of the study, the ratio of the reduced partition functions computed from the final gas $\underset{\sim}{F}$-matrix of Table 14 and the preliminary liquid $\underset{\sim}{F}$-matrix (Table 16) were compared to the experimental data described in Chapter V. In Figures 19 and 20, the ratios of the reduced partition function, f_c/f_g, are given for the pairs $^{12}CH_3F/^{12}CD_3F$ and $^{12}CH_3F/^{13}CH_3F$. The calculated values for the reduced partition function show very little temperature dependence for both isotopic pairs over the entire temperature range, and their magnitudes are significantly different from those of the experimental results. Modifications on the internal force constants produced no significant improvements. In an effort to alleviate this problem, refinements were instituted on the external force constants.

VIC-2-a. Effects of Diagonal $\underset{\sim}{F}$-Matrix Elements for External Motions

The preliminary liquid $\underset{\sim}{F}$-matrix for methyl fluoride used small values for the translational and rotational force constants. These values were varied over a wide range to study the effect on the reduced partition function ratio for $^{12}CH_3F/^{12}CD_3F$ (H/D effect) and $^{12}CH_3F/^{13}CH_3F$ ($^{12}C/^{13}C$ effect). The results are calculated at three different temperatures (representing the liquid range) in Table 20. Both the translational force constant and the rotational force constant

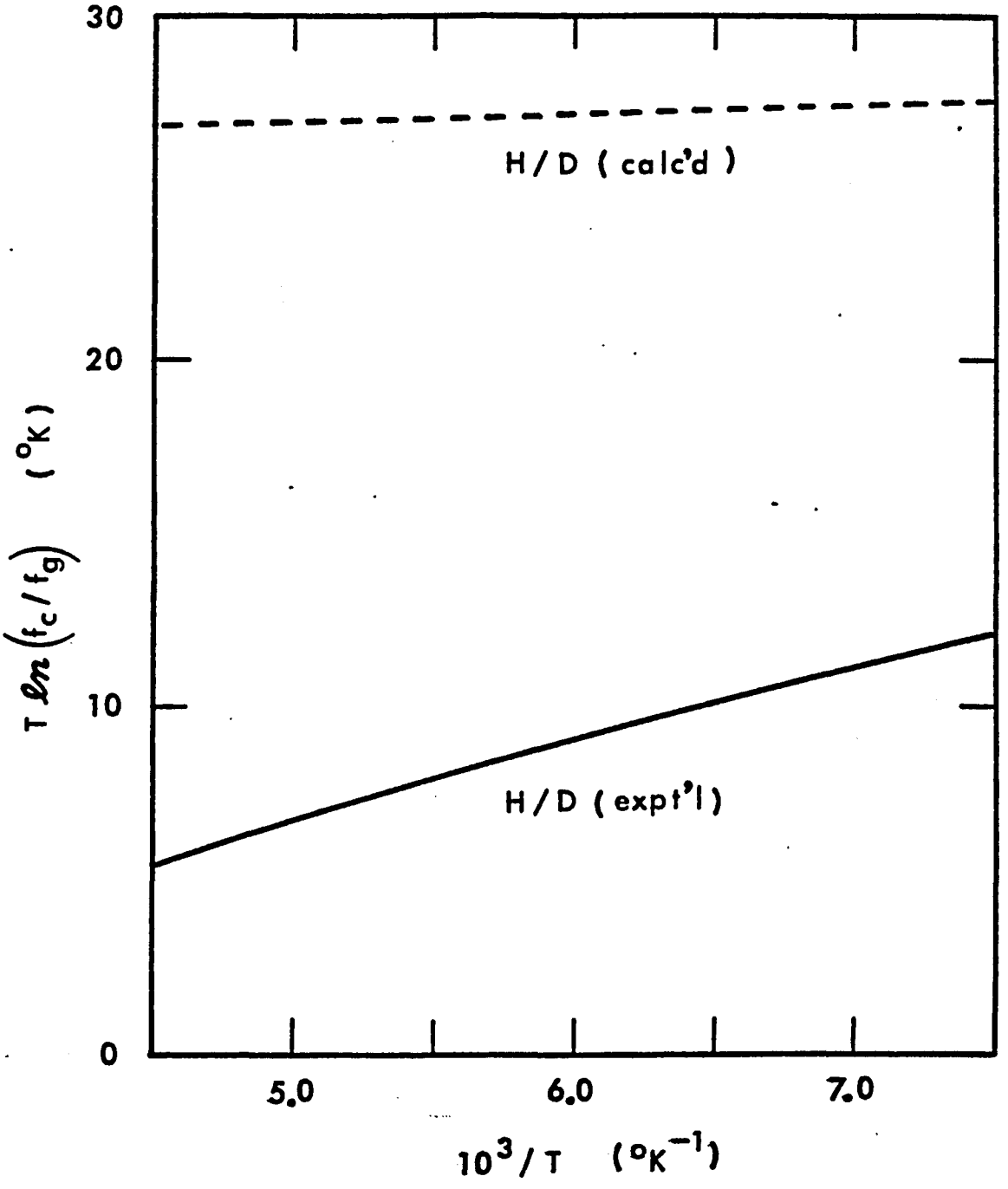

Figure 19. Comparison of experimental T $\ln(f_c/f_g)$ with the values calculated using the preliminary liquid $\underset{\sim}{F}$-matrix of Table 17: H/D-Effect.

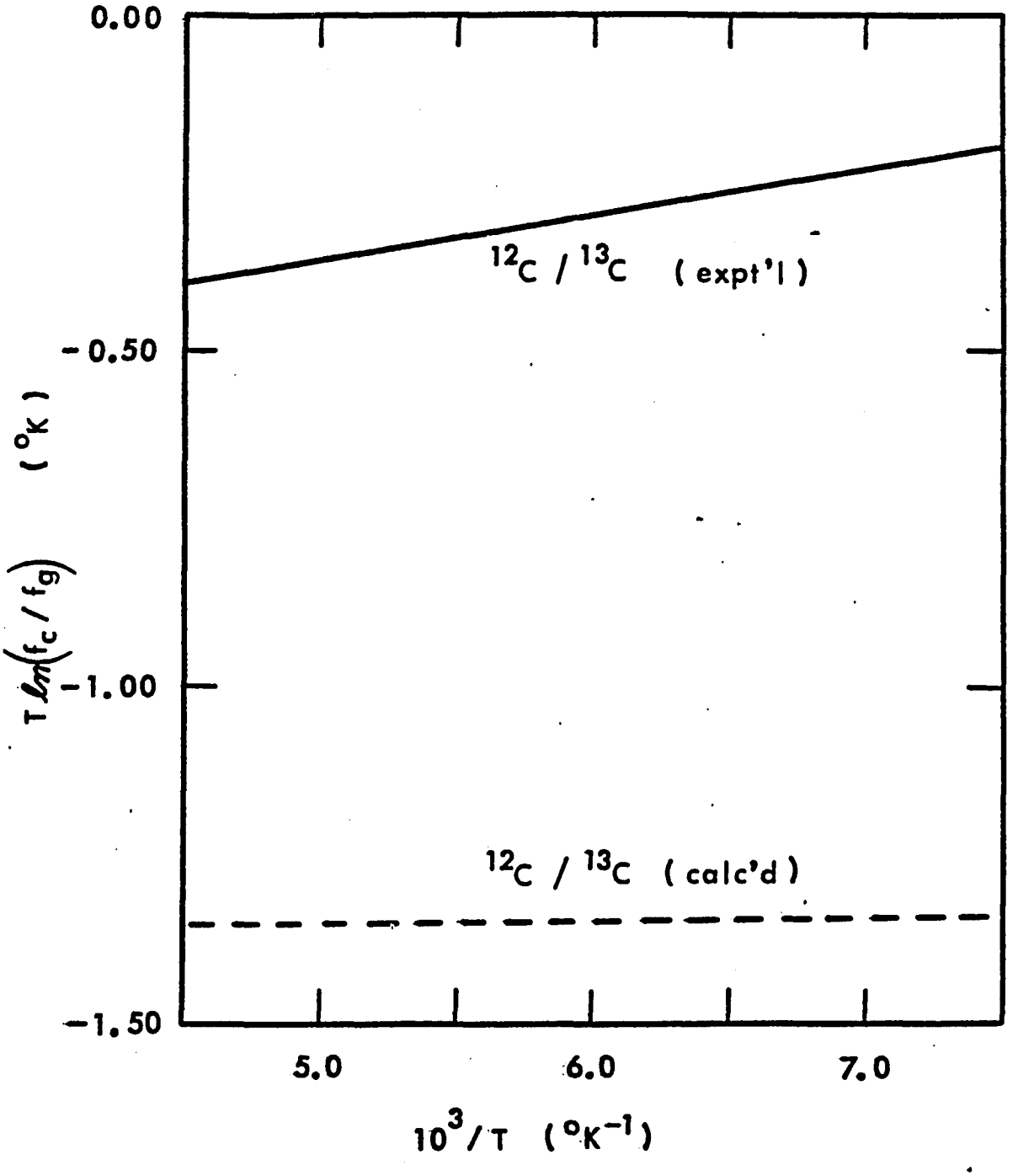

Figure 20. Comparison of experimental T $\ln(f_c/f_g)$ with the values calculated using the preliminary liquid F-matrix of Table 17: $^{12}C/^{13}C$-Effect.

were varied over a physically feasible range. Three independent frequencies representing translational and rotational motions in the X, Y, and Z directions are listed. The reduced partition function ratio for the H/D effect and the $^{12}C/^{13}C$ effect are given at three temperatures. Two important facts emerge from the study of this table. The first concerns the H/D effect, which was found to increase in magnitude by increasing the rotational force constants. The second deals with the $^{12}C/^{13}C$ effect, which is strongly dependent on the translational force constants above 0.10 mdyne/Å. The experimentally calculated reduced partition function ratio has a sharp positive slope for the H/D effect. Increasing the rotational force constants sharpens the slope of the calculated H/D effect, but increases the magnitude substantially and in the wrong direction. Decreasing the rotational force constants to approximately zero flattens the calculated slope, and the magnitude of the curve is still excessively high. In contrast, increasing the translational force constants brings about a sharper, more positive slope possessing the correct order of magnitude for the $^{12}C/^{13}C$ effect. Altering the rotational force constants shifts the magnitude of the $^{12}C/^{13}C$ effect, but the sharper, positive slope is essentially unchanged. Therefore, the translational force constants were fixed at a higher value to improve upon the reduced partition function ratio for the $^{12}C/^{13}C$ effect. The rotational force constants were constrained to smaller values to limit the magnitude of the reduced partition function ratio for the H/D effect.

Table 20. Effects of Varying the Translational(f_T) and Rotational(f_R) Force Constants on T $\ln(f_c/f_g)$[a]

Translational		Rotational			T $\ln(f_c/f_g)$	
f_T	Frequency (cm^{-1})	f_R	Frequency (cm^{-1})	Temperature (°K)	H/D	$^{12}C/^{13}C$
	15.80		20.75	140°	26.4	-1.37
0.005	15.80	0.005	20.75	165°	26.2	-1.37
	15.80		51.06	200°	26.1	-1.37
	15.80		29.35	140°	27.2	-1.36
0.005	15.80	0.01	29.35	165°	27.0	-1.36
	15.80		72.20	200°	26.7	-1.36
	15.80		65.62	140°	34.1	-1.25
0.005	15.80	0.05	65.62	165°	32.9	-1.27
	15.80		161.45	200°	31.6	-1.28
	15.80		92.80	140°	42.3	-1.11
0.005	15.80	0.10	92.80	165°	39.9	-1.15
	15.80		92.80	200°	37.5	-1.19
	22.34		20.75	140°	26.4	-1.36
0.1	22.34	0.005	20.75	165°	26.2	-1.36
	22.34		51.06	200°	26.1	-1.36
	22.34		29.35	140°	27.2	-1.36
0.1	22.34	0.01	29.35	165°	27.0	-1.36
	22.34		72.20	200°	26.7	-1.36

[continued]

[Table 20; continued]

Translational		Rotational			T ln(f_c/f_g)	
f_T	Frequency (cm^{-1})	f_R	Frequency (cm^{-1})	Temperature (°K)	H/D	$^{12}C/^{13}C$
	22.34		65.62	140°	34.2	-1.23
0.01	22.34	0.05	65.62	165°	32.9	-1.26
	22.34		161.45	200°	31.6	-1.28
	22.34		92.80	140°	42.3	-1.10
0.01	22.34	0.10	92.80	165°	40.0	-1.14
	22.34		228.33	200°	37.5	-1.18
	49.95		20.75	140°	26.6	-1.26
0.05	49.95	0.005	20.75	165°	26.4	-1.28
	49.95		51.06	200°	26.2	-1.29
	49.95		29.35	140°	27.5	-1.24
0.05	49.95	0.01	29.35	165°	27.2	-1.26
	49.95		72.20	200°	26.9	-1.28
	49.95		65.62	140°	34.4	-1.13
0.05	49.95	0.05	65.62	165°	33.1	-1.17
	49.95		161.45	200°	31.7	-1.20
	49.95		92.80	140°	42.6	-0.99
0.05	49.95	0.10	92.80	165°	40.2	-1.05
	49.95		228.33	200°	37.7	-1.11

[continued]

[Table 20; continued]

Translational		Rotational			T ln(f_c/f_g)	
f_T	Frequency (cm^{-1})	f_R	Frequency (cm^{-1})	Temperature (°K)	H/D	$^{12}C/^{13}C$
	70.64		20.75	140°	26.9	-1.13
0.10	70.64	0.005	20.75	165°	26.7	-1.17
	70.64		5.06	200°	26.4	-1.20
	70.64		29.35	140°	27.8	-1.12
0.10	70.64	0.10	29.35	165°	27.4	-1.16
	70.64		72.20	200°	27.1	-1.19
	70.64		65.62	140°	34.7	-1.00
0.10	70.64	0.05	65.62	165°	33.3	-1.06
	70.64		161.45	200°	31.9	-1.11
	70.64		92.80	140°	42.9	-0.87
0.10	70.64	0.10	92.80	165°	40.4	-0.95
	70.64		228.33	200°	37.9	-1.02
	157.96		20.75	140°	29.2	-0.155
0.50	157.96	0.005	20.75	165°	28.6	-0.332
	157.96		51.06	200°	28.0	-0.506
	157.96		29.35	140°	30.0	-0.141
0.50	157.96	0.01	29.35	165°	29.3	-0.320
	157.96		72.20	200°	28.6	-0.496

[continued]

[Table 20; continued]

Translational		Rotational			T ln(f_c/f_g)	
f_T	Frequency (cm^{-1})	f_R	Frequency (cm^{-1})	Temperature (°K)	H/D	$^{12}C/^{13}C$
	157.96		65.62	140°	36.9	-0.028
0.50	157.96	0.05	65.62	165°	35.2	-0.226
	157.96		161.45	200°	33.5	-0.416
	157.96		92.80	140°	45.1	+0.107
0.50	157.96	0.10	92.80	165°	42.3	-0.109
	157.96		228.33	200°	39.4	-0.322
	157.96			140°	28.4	-0.168
0.50	157.96	0.0005		165°	27.9	-0.342
	157.96			200°	27.4	-0.515
	157.96			140°	28.3	-0.169
0.50	157.96	0.000001		165°	27.8	-0.344
	157.96			200°	27.3	-0.516

(a) The frequencies and T ln (f_c/f_g) were calculated by using $\underset{\sim}{F}$-matrices of Tables 15 and 17, except for f_T and f_R whose values are varied as shown in the present table.

VIC-2-b. Contributions of Individual Normal Motions to T $\ln(f_c/f_g)$

The ratio of the isotopic reduced partition function ratios may be written as

$$\ln(f_c/f_g) = \sum_{c}^{ext} \delta \ln b(u_j) + \left[\sum_{c}^{int} \delta \ln b(u_i) - \sum_{g}^{int} \delta \ln b(u_i) \right] ,$$

where $\ln b(u) = u/2 - \ln u + \ln (1-e^{-u})$,

$$\delta \ln b(u_i) = \ln b(u_i') - \ln b(u_i) ,$$

and the first, second, and third summations are taken over the external modes in the condensed phase, the internal modes in the condensed phase, and the internal modes in the gas phase, respectively. Therefore, contribution of an internal normal mode, i, to $\ln(f_c/f_g)$ is represented by $\delta \ln b(u_i)_c - \delta \ln b(u_i)_g$, and contribution of an external mode, j, to $\ln(f_c/f_g)$ may be expressed as $\delta \ln b(u_j)_c$. These contributions are plotted against the inverse temperature for the H/D effect in Figure 21. Description of this study will now focus on the H/D effect, because the calculated values (slope and magnitude) for the $^{12}C/^{13}C$ effect can be refined and correlated with the experimental results fairly well without much trouble. The contribution of each individual frequency is illustrated in Figure 21, and the six external frequencies are represented as the sum of all translational and rotational modes. From the diagram it is clear that the slope of the experimentally determined T $\ln(f_c/f_g)$ is far sharper than the slope of

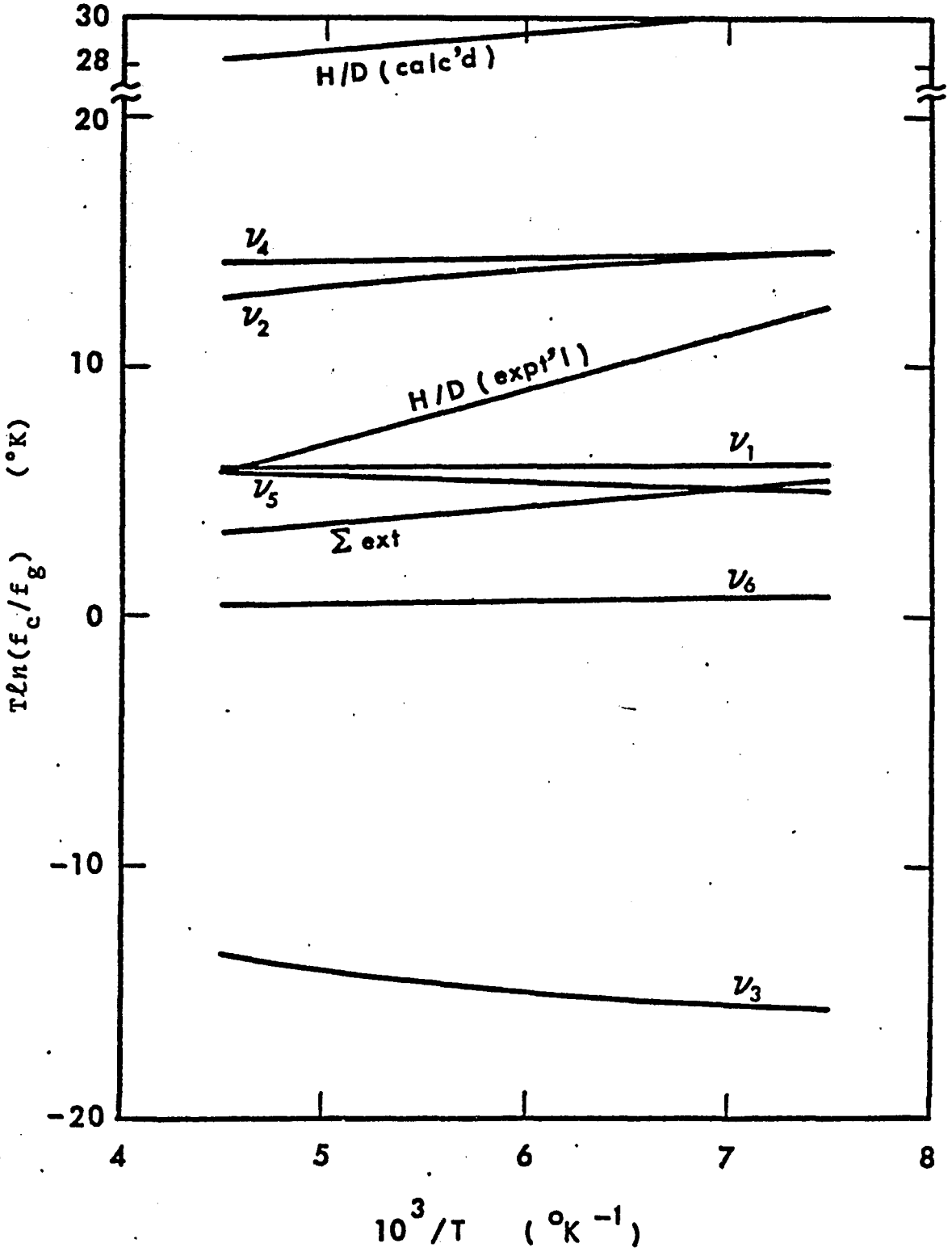

Figure 21. Contributions of the internal and external frequencies to T $\ln(f_c/f_g)$(H/D): The calculations were made using the preliminary liquid F-matrix of Table 17.

any of the six internal modes or the sum of the effect of the external modes. By increasing the external frequencies, we can modify the H/D effect and make it highly temperature-dependent, but the magnitude of the term T ln (f_c/f_g) would then be 10 times too large. Minimizing the external frequencies has little effect on the reduced partition function ratio for the H/D effect. Decreasing the ν_2 and ν_3 contributions would improve upon the magnitude of the calculated H/D effect, but the slope would remain flat. Changes in ν_1, ν_4, and ν_6 in either direction do little to improve the flat slope of the calculated reduced partition function ratio. An attempt to match the slope of the H/D effect by adjusting the internal liquid force constant matrix was the next step in the liquid $\underset{\sim}{F}$-matrix refinement process.

VIC-2-c. Effects of $\underset{\sim}{F}$-Matrix Elements for Internal Motions

The sixteen (four diagonal and twelve off-diagonal) $\underset{\sim}{F}$-matrix elements were modified by using a program P9042D (previously discussed). Each internal force constant was increased by 1% while keeping all other f_{ij} unchanged, and using $T_x=T_y=0.48$ mdyn/Å, $T_z=0.53$ mdyn/Å, and $R_x=R_y=R_z=0.01$ mdyn Å. The results are summarized in Figure 22. In several cases, the magnitude of the H/D effect is significantly changed. By decreasing some of the internal force constants (f_d, f_α, f_β, etc.), the experimentally observed magnitude for the H/D effect at any given temperature could be matched. The problem still remaining is to produce a more highly temperature-dependent slope, as in the experimentally determined H/D effect. Not one of the internal force constants sharpens

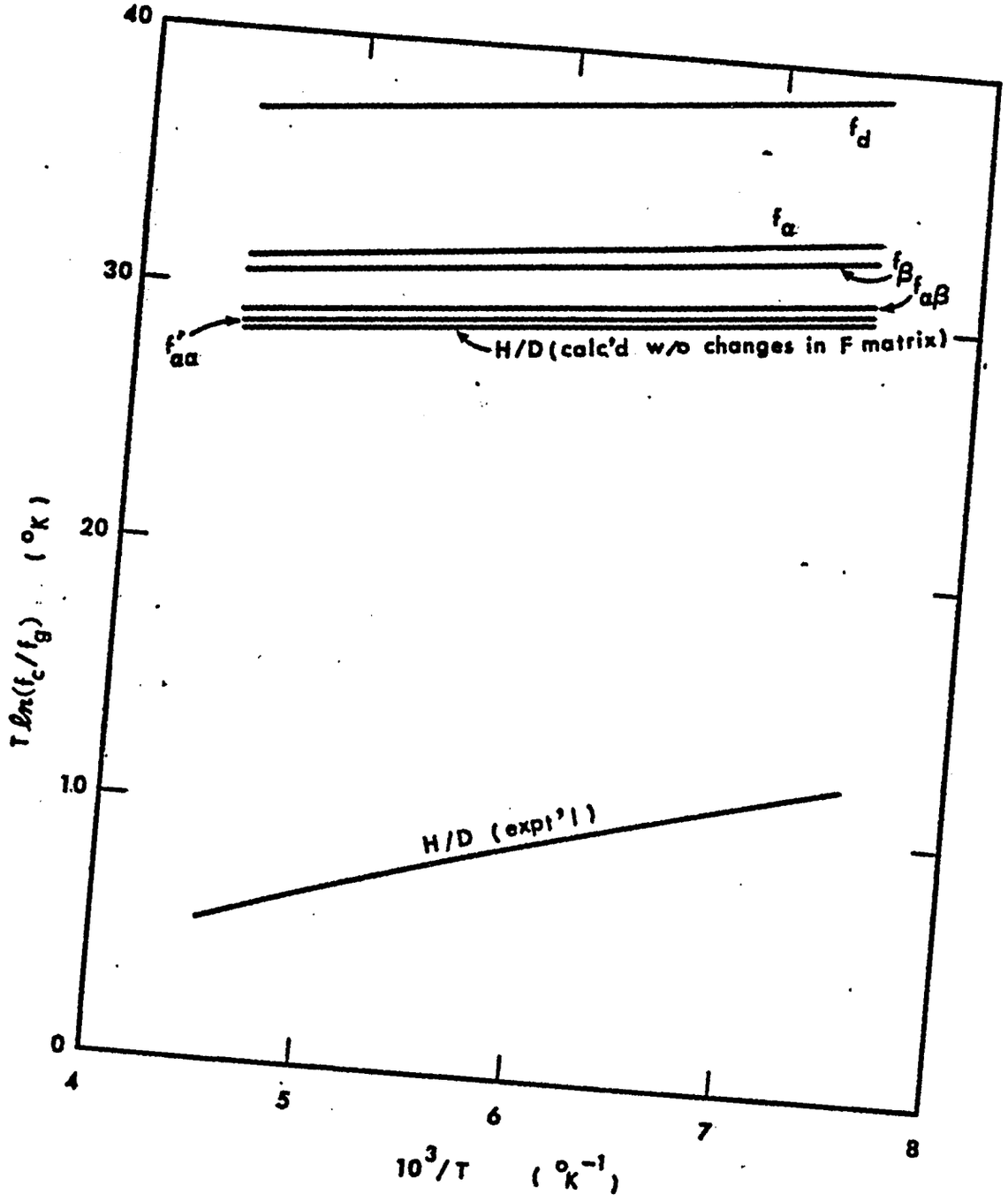

Figure 22. Effects of 1% changes in f_{ij}'s on $T \ln(f_c/f_g)$: H/D-Effect.

the slope when it is increased or decreased. Adjustment of the internal force constants does effect the $^{12}C/^{13}C$ reduced partition function ratio. The magnitude of the $^{12}C/^{13}C$ effect is affected to a small extent by the changes in the four diagonal elements, but the slope remains at about the same value. Changes in the remaining twelve off-diagonal force constants for the internal motions have a negligible effect on the slope and magnitude of the $^{12}C/^{13}C$ effect.

VIC-2-d. Effects of External-Internal Interaction Force Constants - Case of Temperature-Independent Forces

The modifications on the preliminary liquid $\underset{\sim}{F}$-matrix have encompassed changes in the internal and external force constants. The use of large translational force constants has produced a reduced partition function ratio for the $^{12}C/^{13}C$ effect which compares fairly well with the experimentally determined reduced partition function ratio. However, refinements on the internal and external force constants have not yielded a reduced partition function ratio for the H/D effect with any significant temperature-dependence. Despite being able to match the relative magnitude of the experimental H/D effect, all modifications produce a basically flat line for T ln (f_c/f_g) vs. 1/T.

Internal-external interaction force constants were implemented in the liquid $\underset{\sim}{F}$-matrix in an attempt to match both the slope and magnitude for the reduced partition function ratio for both pairs ($^{12}C/^{13}C$ and H/D) of isotopic methyl fluorides. The internal-external interaction force constant results from the translation, T_z, along the C-F axis and

its interaction with various internal coordinates. These include the C-F stretch (f_{DT_z}), the C-H stretch (f_{dT_z}), the HCH bend ($f_{\alpha T_z}$), and the HCF bend ($f_{\beta T_z}$). A large internal-external interaction was applied to f_{DT_z}, f_{dT_z}, $f_{\alpha T_z}$, and $f_{\beta T_z}$, and its effect on the calculated reduced partition function ratio for the H/D and $^{12}C/^{13}C$ effects was analyzed. In Figure 23 the effect of a large internal-external interaction is plotted for f_{DT_z} and f_{dT_z}, using $T_x=T_y=0.48$ mdyne/Å, $T_z=0.53$ mdyne/Å and $R_x=R_y=R_z=0.01$ mdyne Å. The magnitude of the internal-external interaction is 0.5 mdyne/Å for both cases. The net result on the reduced partition function for the H/D effect using either f_{DT_z} or f_{dT_z} is relatively small. Using f_{DT_z} (-0.50 mdyne/Å) increases the reduced partition function ratio slightly, and f_{dT_z} (+0.50 mdyne/Å) raises the value of T ln (f_c/f_g) a fraction more. A huge internal-external interaction of the opposite sign would be required to decrease the calculated reduced partition function ratio to a level similar to the experimentally determined reduced partition function ratio. The magnitudes of the internal-external interactions required for this procedure are so large that they are out of the commonly accepted range. In addition, the slope of the calculated H/D effect is still relatively flat, and does not reproduce the experimentally observed reduced partition function ratio.

Large internal-external force constants were instituted for $f_{\alpha T_z}$ and $f_{\beta T_z}$ in the liquid $\underset{\sim}{F}$-matrix, and their effect on the calculated reduced partition function ratio is depicted in Figure 24. The liquid $\underset{\sim}{F}$-matrix utilizes the best fit rotational and translational force constants ($R_x=R_y=R_z=0.01$ mdyne Å, $T_x=T_y=0.48$ mdyne/Å, and

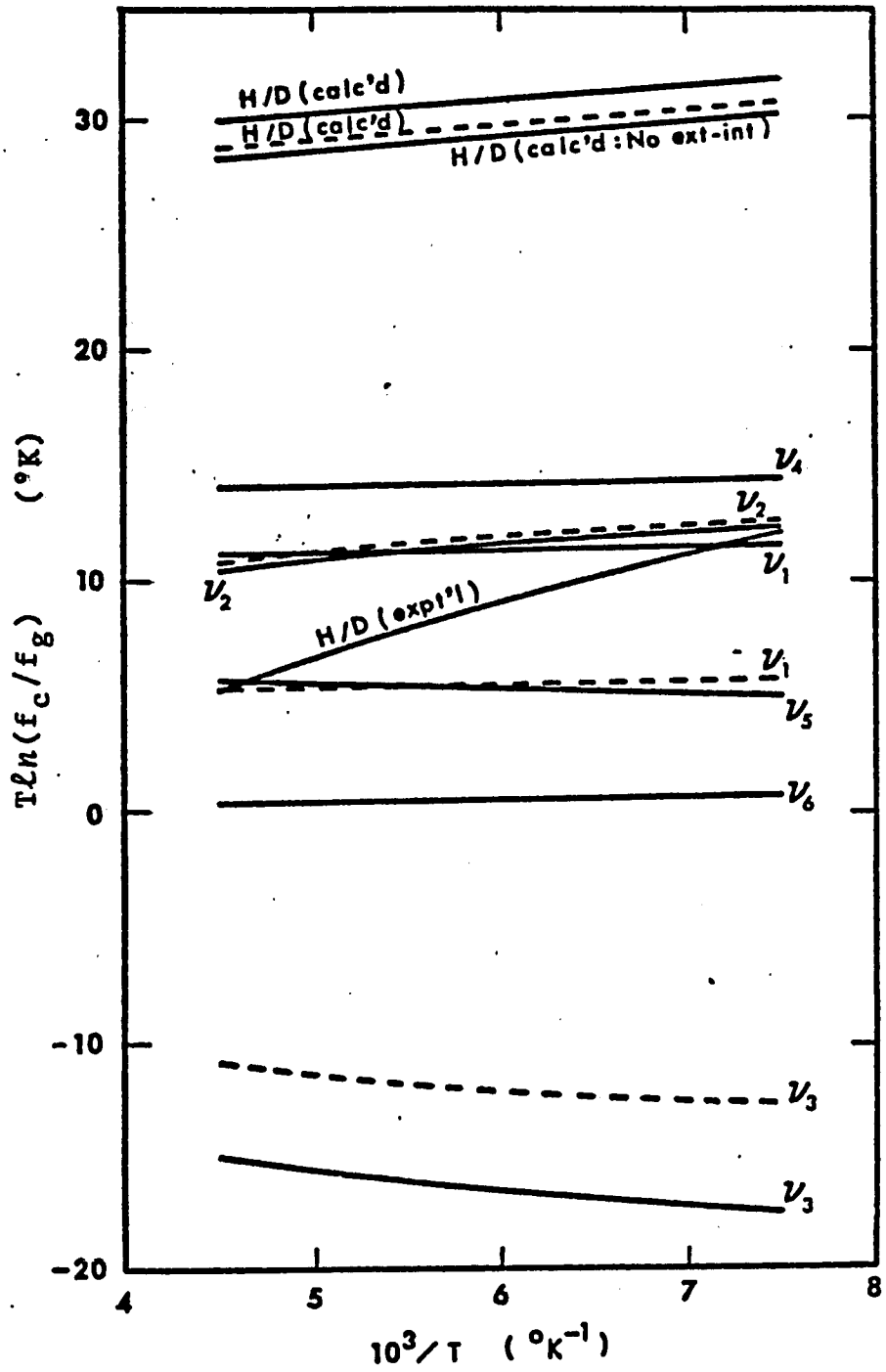

Figure 23. Effect of Internal-External Interactions on T $\ln(f_c/f_g)$ and contributions: Effects of f_{DT_z} and f_{dT_z} on the H/D-Effect. The dotted lines are calculated using f_{DT_z}=-0.50 mdyn/Å. The solid lines are calculated using f_{dT_z}=+0.50 mdyn/Å. The frequencies for which only a solid line is plotted are affected in the same way by these interactions. The basis F-matrix for liquid is that of Table 17.

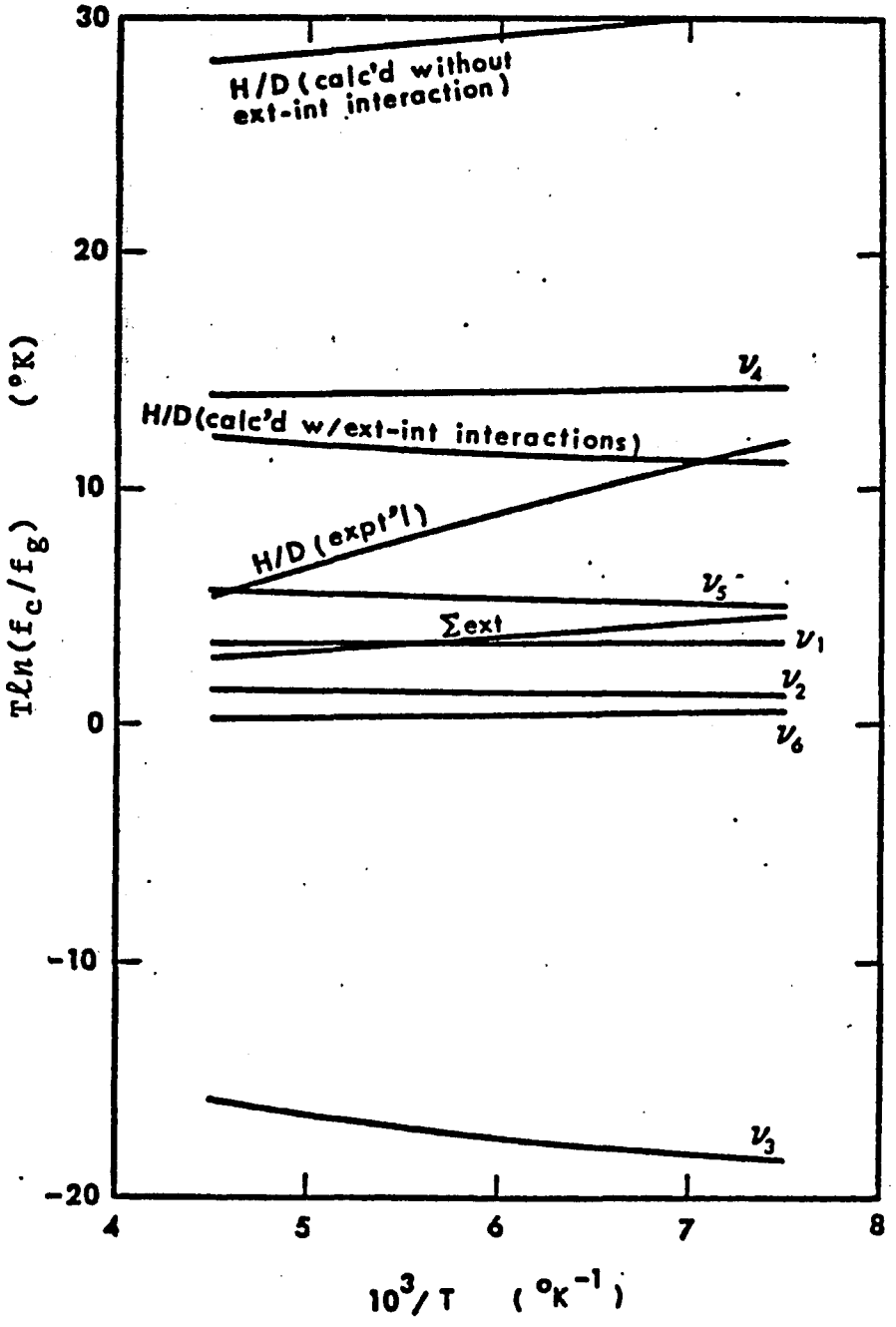

Figure 24. Effect of Internal-External Interactions on T $\ln(f_c/f_g)$ and contributions: Effects of $f_{\alpha T_z}$ and $f_{\beta T_z}$ on the H/D-Effect. The $\underset{\sim}{F}$-matrix for liquid was constructed by adding $f_{\alpha T_z}$ = -0.50 mdyn/Å or $f_{\beta T_z}$ = +0.50 mdyn/Å, one at a time, to the matrix of Table 17. Both interactions have indistinguishably similar effects on all frequencies.

T_z=0.53 mdyne/Å), and values for $f_{\alpha T_z}$ and $f_{\beta T_z}$ of -0.50 mdyne/Å and +0.50 mdyne/Å, respectively. Both internal-external interactions produce the same net effect on the reduced partition function ratio. The calculated value of T ln (f_c/f_g) is shifted sharply downward, and the magnitude correlates well with the experimentally observed data at low temperature. The problem is the slope, which has changed from slightly positive to slightly negative after implementing the $f_{\alpha T_z}$ or $f_{\beta T_z}$ internal-external interaction. Adjusting the values of $f_{\alpha T_z}$ and $f_{\beta T_z}$ cannot improve the calculated slope. Analysis of the contributions to T ln (f_c/f_g) of the individual internal and external frequencies fails to produce a sharply positive slope for any of the contribution plots. Therefore, the use of temperature-independent internal-external force constants (f_{DT_z}, f_{dT_z}, $f_{\alpha T_z}$, and $f_{\beta T_z}$) cannot reproduce the sharp positive slope for the H/D experimental data.

In addition to examining the H/D effect, studies were conducted on the reduced partition function ratio for the $^{12}C/^{13}C$ effect after instituting temperature-independent internal-external interactions. In Figure 25, large changes are evident in the magnitude and slope for each effect (f_{DT_z}, f_{dT_z}, $f_{\alpha T_z}$ and $f_{\beta T_z}$). Due to the inability of producing a highly temperature-dependent slope for the H/D effect, further refinements on the $^{12}C/^{13}C$ effect were not attempted at this time.

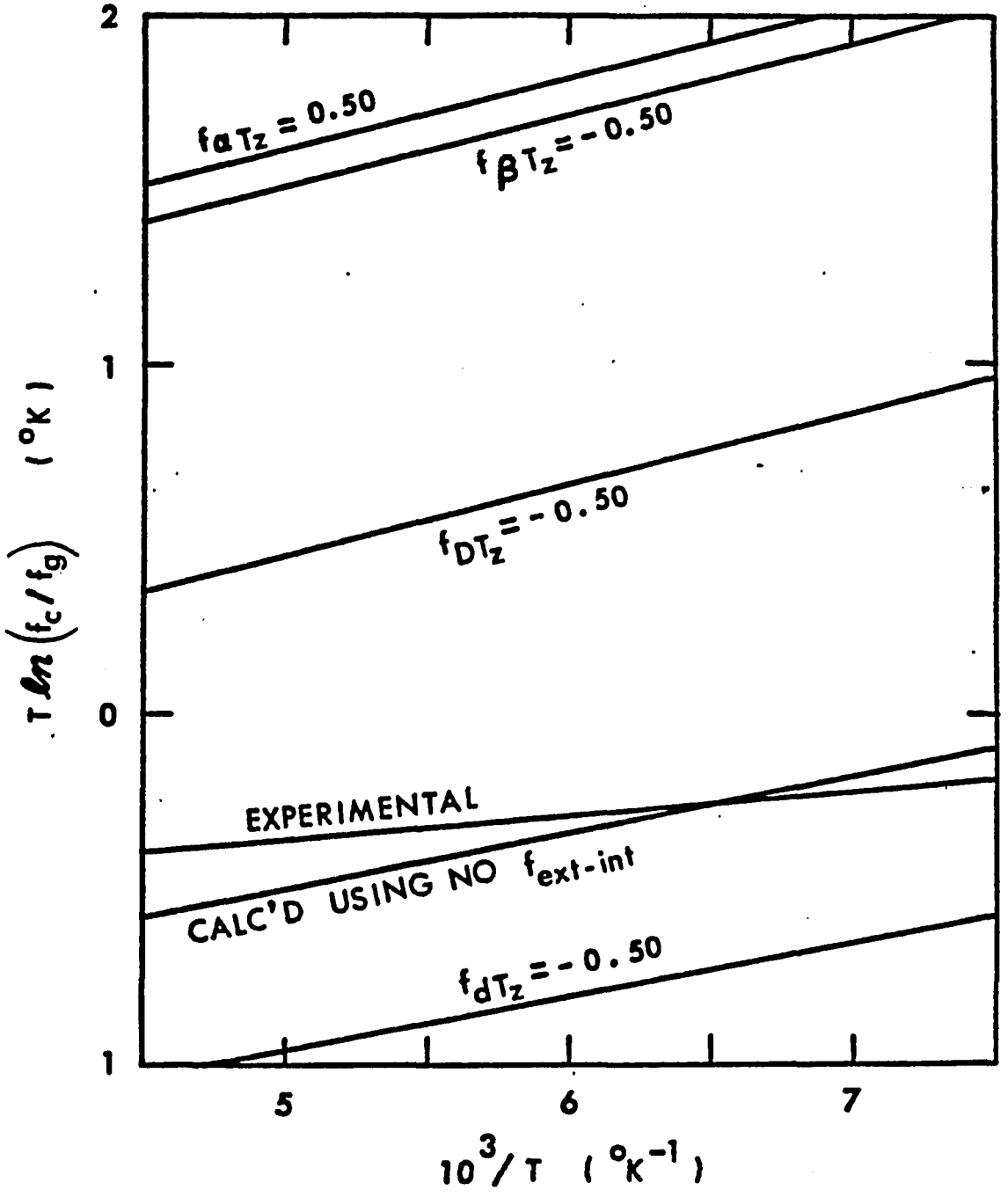

Figure 25. Effects of Internal-External Interactions of T $\ln(f_c/f_g)$: $^{12}C/^{13}C$-Effect. The basis $\underset{\sim}{F}$-matrix for liquid is that of Table 17. The indicated external-internal interaction constants (in units of mdyn/Å) are added to it, one at a time.

VIC-2-e. Effects of External-Internal Interaction Force Constants - Case of Temperature-Dependent Forces

Attempts at refining the preliminary liquid $\underset{\sim}{F}$-matrix by modifying the internal force constants and introducing external and internal-external (temperature-independent) interactions on the liquid $\underset{\sim}{F}$-matrix have met with limited success. The magnitude of the reduced partition function ratio can be matched at any given temperature for both the H/D and $^{12}C/^{13}C$ effects by performing adjustments on the liquid $\underset{\sim}{F}$-matrix. However, at different temperatures, the same liquid $\underset{\sim}{F}$-matrix produces values for the reduced partition function ratio which do not match up with the experimentally observed data. There is a sharp contrast between the calculated slope and the experimental data. Griffiths[5] studied the temperature dependence of several of the fundamental frequencies, and observed significant changes occurring within the liquid temperature range. In a similar manner, it was decided to study the liquid $\underset{\sim}{F}$-matrix as a function of temperature. The preliminary liquid $\underset{\sim}{F}$-matrix was used as a starting point, and internal-external interactions were introduced and varied over the experimentally studied range as a function of temperature. The temperature-dependent liquid $\underset{\sim}{F}$-matrix was calculated by formulating six individual liquid $\underset{\sim}{F}$-matrices at six different temperatures; 210°K, 200°K, 180°K, 165°K, 153°K, and 140°K. For each liquid $\underset{\sim}{F}$-matrix calculated at a different temperature, the internal and external force constants were not varied. The internal-external interactions were refined at each temperature to reproduce the experimentally observed reduced partition function ratio. In

Table 21, the temperature dependent liquid $\underset{\sim}{F}$-matrix at 153°K is listed. Only the internal-external force constants (listed at 153°K in this case) are varied over the entire liquid temperature range. The functional form of the internal-external interactions will be discussed at a later time. The internal and external force constants listed in Table 21 retain the same values at every temperature in the liquid region. The calculated frequencies produced by the temperature-dependent liquid $\underset{\sim}{F}$-matrix at 153°K are listed in Table 22. This temperature was chosen as a means of comparing the calculated data to Chao and Eggers[12] liquid frequency data, also measured at 153°K. The calculated frequencies compare fairly well with observed frequencies (cf. Table 19). The calculated translational and rotational frequencies suggest four distinct peaks. Barnes, et al.[51] studied the far infra-red spectrum of solid fluoromethane and observed two strong bands at 125 and 101 cm^{-1}, while the other halogenomethanes show only one band in this region. At the same time, the band center observed at about 40 cm^{-1} for other halogenomethanes was absent for fluoromethane. The far infra-red spectrum appeared to reveal additional peaks below 100 cm^{-1}, but the authors did not elaborate on these observations. The translational frequency of 120.5 cm^{-1} for $^{12}CH_3F$ presented in Table 22 is in good agreement with Barnes' experimental result obtained for the crystal.

The temperature-dependent liquid $\underset{\sim}{F}$-matrix is a function of the internal-external force constants. The values of these constants obtained at the six temperatures have been fit to the functional form,

$$f_{ij} = A(T-153)^2 + B(T-153) + C \ , \qquad (34)$$

Table 21. The Liquid $\underset{\sim}{F}$-Matrix of Methyl Fluoride at 153°K

Description	Diagonals Notation[a]	Diagonals Value (mdyne/Å)	Off-diagonals Notation[a]	Off-diagonals Value (mdyne/Å)
C-H stretch	f_d	4.788	f_{dd}	-0.035
C-F stretch	f_D	5.072	f_{Dd}	0.515
HCH bend	f_α	0.403	$f'_{d\alpha}$	-0.125
HCF bend	f_β	0.602	$f_{d\alpha}$	-0.185
			$f_{D\alpha}$	-0.260
			$f'_{\alpha\alpha}$	-0.053
			$f'_{d\beta}$	0.021
			$f_{d\beta}$	0.094
			$f_{D\beta}$	0.260
Translation	f_{T_x}	0.010	$f'_{\alpha\beta}$	-0.138
	f_{T_y}	0.010	$f_{\alpha\beta}$	-0.111
	f_{T_z}	0.400	$f'_{\beta\beta}$	-0.147
			Internal-External	
Rotation	f_{R_x}[b]	0.009	f_{DT_z}	-0.142
	f_{R_y}	0.009	$f_{\alpha T_z}$	-0.091
	f_{R_z}	0.009	$f_{\beta T_z}$	+0.092

(a) For definition of internal coordinates, see Figure 18 and footnote of Table 11.

(b) All $\underset{\sim}{F}$-matrix elements are in units of mdyne/Å, except f_R, which are in units of mdyne Å.

Table 22. Calculated Frequencies for Liquid Methyl Fluoride at 153°K

Mode	Frequency (cm^{-1})		
	$^{12}CH_3F$	$^{12}CD_3F$	$^{13}CH_3F$
ν_1 (A_1)	2914.223*	2107.835*	2909.777*
ν_2 (A_1)	1457.217	1111.384	1451.175
ν_3 (A_1)	992.643	948.523	971.441
ν_4 (E)	3029.269	2270.843	3015.359
ν_5 (E)	1468.968	1052.420	1467.762
ν_6 (E)	1180.082	907.423	1172.163
Translation	22.338	21.083	22.001
	22.338	21.083	22.001
	120.463	114.353	118.922
Rotation	27.839	25.281	27.486
	27.839	25.281	27.486
	68.498	48.454	68.498

*ν_1 frequency corrected for Fermi resonance.

where f_{ij} is the internal-external force constant in mdyne/Å, T is in K, and A, B, and C are constants. Two sets of the interaction constants were studied: The first consisted of f_{DT_z}, $f_{\alpha T_z}$ and $f_{\beta T_z}$, and the second consisted of f_{DT_z}, f_{dT_z}, $f_{\alpha T_z}$, and $f_{\beta T_z}$.

(1) Temperature-Dependent Set: f_{DT_z}, $f_{\alpha T_z}$, $f_{\beta T_z}$.

The first temperature-dependent liquid $\underset{\sim}{F}$-matrix obtained utilizes only three of the four internal-external interactions. In Table 23, the least square coefficients (A, B and C) are listed for the internal-external interactions. The reduced partition function ratios for the H/D and $^{12}C/^{13}C$ effects were calculated at six different temperatures using the least square coefficients for f_{DT_z}, $f_{\alpha T_z}$, and $f_{\beta T_z}$ of Table 23 and the internal and external force constants in Table 21. The values for T ln (f_c/f_g) calculated as a function of temperature have been summarized in Table 24. These calculated results are compared with the experimental values in Figure 26 for the H/D effect and in Figure 27 for the $^{12}C/^{13}C$ effect. The results calculated from the temperature-dependent liquid $\underset{\sim}{F}$-matrix are in excellent agreement with the experimentally obtained reduced partition function ratios. The discussion thus far has demonstrated the fact that such an agreement is possible only by the use of the liquid $\underset{\sim}{F}$-matrix which contains the temperature-dependent interaction force constants between the internal and external motions.

(2) Temperature-Dependent Set: f_{DT_z}, f_{dT_z}, $f_{\alpha T_z}$, $f_{\beta T_z}$.

A second temperature-dependent liquid $\underset{\sim}{F}$-matrix was constructed using all four internal-external force constants (f_{DT_z}, f_{dT_z}, $f_{\alpha T_z}$, and $f_{\beta T_z}$).

Table 23. Least Square Coefficients* for f_{DT_z}, $f_{\alpha T_z}$, and $f_{\beta T_z}$ of the form

$$f_{ij} = A(T-153)^2 + B(T-153) + C$$

(ij)	$A(°K^{-2})$	$B(°K^{-1})$	C
DT_z	0.12859×10^{-5}	-0.10667×10^{-2}	-0.91119×10^{-1}
αT_z	-0.48363×10^{-6}	0.10314×10^{-2}	0.91680×10^{-1}
βT_z	-0.99083×10^{-6}	0.38449×10^{-2}	-0.14157×10^{0}

*f_{ij} is in mdyne/Å and T is in °K.

Table 24. Calculated Values of the Reduced Partition Function Ratio at Various Temperatures Using the Temperature-Dependent Liquid $\underset{\sim}{F}$-Matrix of Tables 21 and 23

Temperature (°K)	$T \ln(f_c/f_g)$, (°K)	
	H/D	$^{12}C/^{13}C$
210°	6.038	-0.3758
200°	6.659	-0.3604
180°	8.033	-0.3256
165°	9.189	-0.2962
153°	10.190	-0.2697
140°	11.363	-0.2384

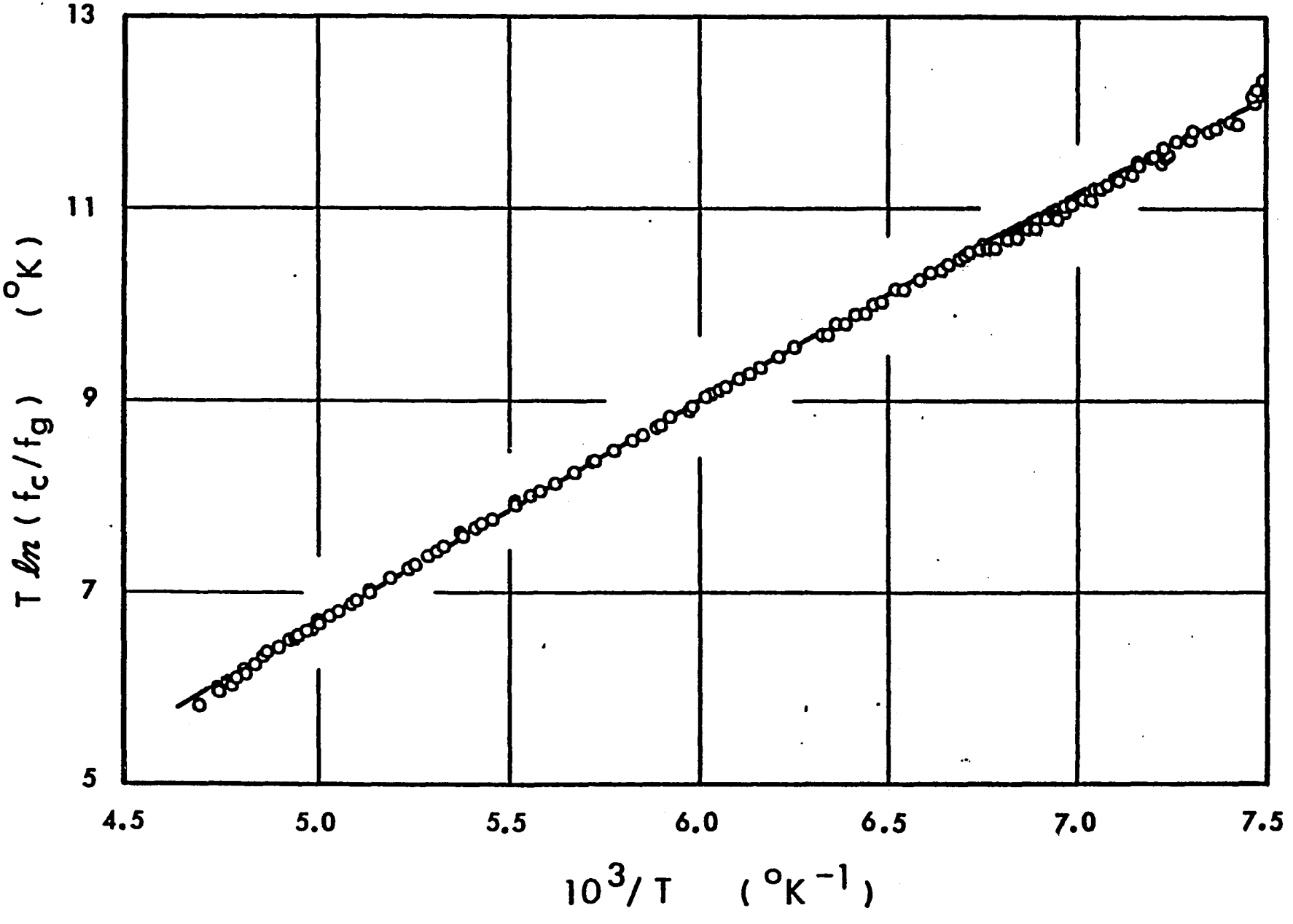

Figure 26. Comparison of experimental and calculated values of T $\ln(f_c/f_g)$: H/D-Effect.

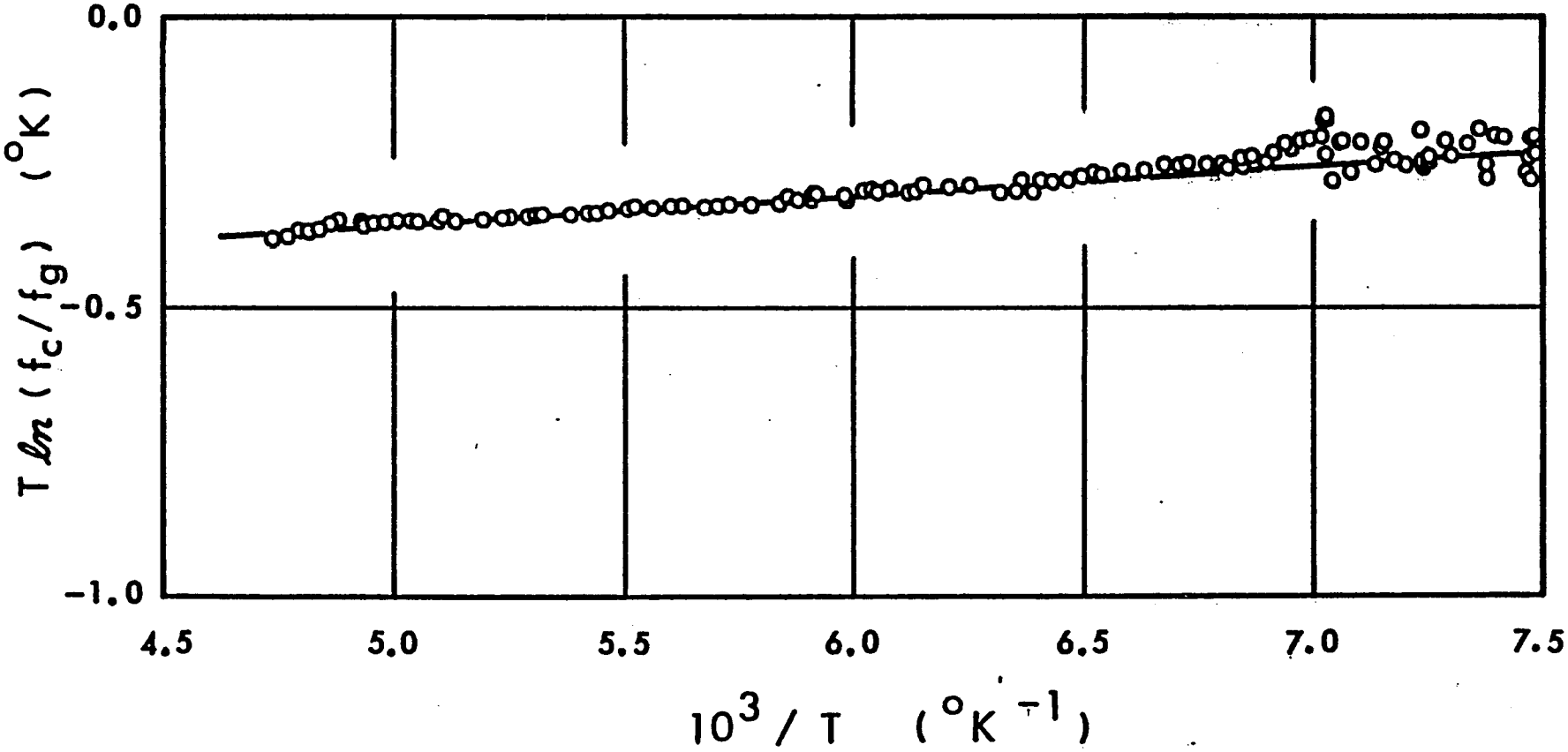

Figure 27. Comparison of experimental and calculated values of T $\ln(f_c/f_g)$: $^{12}C/^{13}C$-Effect.

The least square coefficients obtained by fitting the f_{ij} data at the six temperatures to the form Eq. (34) are listed for each internal-external interaction in Table 25. The second temperature-dependent liquid $\underset{\sim}{F}$-matrix utilizes the identical internal and external force constants as those found in Table 21. A comparison of the calculated frequencies for both temperature-dependent liquid $\underset{\sim}{F}$-matrices is presented in Table 26. The calculated frequencies are in good agreement with one another, with the greatest disparity being approximately 2 cm^{-1} for the translational frequency in the z-direction (f_{T_z}). The remaining internal and external frequencies are all within ± 0.25 cm^{-1} of each other. The results for the reduced partition function ratio for both temperature-dependent liquid $\underset{\sim}{F}$-matrices calculated at six different temperatures are summarized in Table 27. For each $\underset{\sim}{F}$-matrix, the values of $T \ln (f_c/f_g)$ are listed for the H/D and $^{12}C/^{13}C$ effect. The calculated values of $\underset{\sim}{F}(1)$ and $\underset{\sim}{F}(2)$ reproduce the experimental data equally well. The introduction of f_{dT_z} to the second liquid $\underset{\sim}{F}$-matrix does not improve or significantly effect the results obtained without it. In both temperature-dependent liquid $\underset{\sim}{F}$-matrices, the use of internal-external interaction force constants results in a very good agreement between the calculated and experimentally observed reduced partition function ratio.

Both Tables 23 and 25 clearly show that f_{DT_z} is the largest external-internal interaction constant and that f_{DT_z} has by far the strongest temperature-dependence. This off-diagonal constant represents the interaction between the C-F stretching motion and the translational oscillation of the whole molecule in the direction of

Table 25. Least Square Coefficients* for f_{DT_z}, f_{dT_z}, $f_{\alpha T_z}$, and $f_{\beta T_z}$ of the form

$$f_{ij} = A(T-153)^2 + B(T-153) + C$$

(ij)	$A(°K^{-2})$	$B(°K^{-1})$	C
DT_z	-0.23980×10^{-5}	0.36897×10^{-2}	-0.13335×10^{0}
dT_z	0.12065×10^{-5}	-0.12429×10^{-2}	0.44122×10^{-1}
αT_z	0.12859×10^{-5}	0.10667×10^{-2}	-0.91119×10^{-1}
βT_z	-0.48363×10^{-6}	0.10314×10^{-2}	-0.91690×10^{-1}

*f_{ij} is in mdyne/Å and T is in °K.

Table 26. Comparison of Calculated Frequencies[a] of $^{12}CH_3F$ Using Two Temperature-Dependent Liquid $\underset{\sim}{F}$-Matrices at 153°K

Mode	$\underset{\sim}{F}$-Matrix (1)[b]	$\underset{\sim}{F}$-Matrix (2)[b]
ν_1 (A_1)	2914.223[c]	2914.258[c]
ν_2 (A_1)	1457.217	1456.985
ν_3 (A_1)	992.643	992.636
ν_4 (E)	3029.269	3029.269
ν_5 (E)	1468.968	1468.968
ν_6 (E)	1180.082	1180.082
Translation	22.338	22.338
	22.338	22.338
	120.463	122.456
Rotation	27.839	27.839
	27.839	27.839
	68.498	68.498

(a) Frequencies in cm^{-1}.

(b) Liquid $\underset{\sim}{F}$-matrix (1) is given by Tables 21 and 23. Liquid $\underset{\sim}{F}$-matrix (2) is given by Tables 21 and 25. For $\underset{\sim}{F}$-matrix (1), $f_{dT_z} = 0$ at 153°K. For $\underset{\sim}{F}$-matrix (2), $f_{dT_z} = 0.044$ at 153°K.

(c) ν_1 frequency corrected for Fermi resonance.

Table 27. Comparison of the Calculated Values of the Reduced Partition Function Ratio for the Two Temperature-Dependent Liquid $\underset{\sim}{F}$-Matrices

Temperature (°K)	$\underset{\sim}{F}$-Matrix (1)		$\underset{\sim}{F}$-Matrix (2)	
	H/D	$^{12}C/^{13}C$	H/D	$^{12}C/^{13}C$
210°	6.038	-0.3758	6.040	-0.3756
200°	6.659	-0.3604	6.655	-0.3605
180°	8.033	-0.3256	8.027	-0.3262
165°	9.189	-0.2962	9.185	-0.2966
153°	10.190	-0.2697	10.202	-0.2709
140°	11.363	-0.2384	11.393	-0.2402

its figure axis. The fact that it is negative suggests that it is energetically more likely for the CF bond to be stretched while the molecule translates in the positive z direction, i.e., the direction from C to F (cf: Figure 18) and that it is more likely for the CF bond to be compressed while the molecule translates in the negative z-direction, i.e., the direction from F to C. It is also interesting to note in Table 21 that $f_{\alpha T_z}$ is negative while $f_{\beta T_z}$ is positive. These signs of the external-internal force constants mean that it is energetically more probable for the umbrella of CH_3 to open while the molecule translates in the positive z-direction and to close while the molecule translates in the negative z-direction. This is the nature of the combined external and internal motion that has emerged as a result of this study of vapor pressure isotope effect.

VII. CONCLUSION

The study of VPIE has produced new information relating to molecular forces in the condensed phase of methyl fluoride. A new liquid force field has been constructed for methyl fluoride based on the data obtained in this study and solid evidence has been found for the presence of very non-isotropic internal-external interactions in the liquid state. The two temperature-dependent liquid $\underset{\sim}{F}$-matrices produced almost identical results, with one set using three internal-external interactions (f_{DT_z}, $f_{\alpha T_z}$ and $f_{\beta T_z}$) and the other using four (f_{DT_z}, f_{dT_z}, $f_{\alpha T_z}$, and $f_{\beta T_z}$). The f_{DT_z} interaction constant is strongly temperature-dependent for both liquid $\underset{\sim}{F}$-matrices.

VIII. RECOMMENDATION

This study has elucidated the nature and source of the intermolecular forces that produced the temperature-dependent internal-external interaction force constants. It has been clearly shown that f_{DT_z} is the largest interaction force constant and is strongly temperature-dependent. A molecular orbital study on the bimolecular, termolecular, and higher conglomerates of methyl fluoride would provide more definitive evidence on the nature of the forces in the condensed states. Recent work on fluoroform has revealed a hydrogen-bond like interaction with a stabilization energy of ∿0.7 kcal/mole dimer.[52] This is about 1/10 the bond energy expected for a bona-fide hydrogen bond. In the case of methyl fluoride, the symmetry considerations are the same, but there are distinct differences between the two molecules. Fluorine can act as an electron donor for more than one electron pair, and there are three hydrogen atoms acting as acceptors per molecule of CH_3F. For CHF_3, there is only one hydrogen atom which can act as an acceptor, and therefore only one hydrogen-bond type interaction per molecule can be found in any conglomerate of fluoroform. The associated fluoroform is linear in general (only one ring structure per conglomerate), whereas methyl fluoride has a potential for forming many branching chains in the associated state. Further studies will

prove to be very useful for increasing our knowledge of the condensed state and understanding intermolecular forces in the liquid.

IX. REFERENCES

1. J. Bigeleisen, F. P. Brooks, T. Ishida, and S. V. Ribnikar, Rev. Sci. Instrum. 39, 353 (1968).

2. A. Popowicz, thesis dissertation.

3. J. Aldous and I. M. Mills, Spectrochim. Acta 18, 1073 (1962).

4. T. H. Chao and D. F. Eggers, Jr., J. Chem. Phys. 66(3), 970 (1977).

5. James E. Griffiths, private communication.

6. M. J. Stern, W. A. Van Hook and M. Wolfsberg, J. Chem. Phys. 39, 3179 (1963).

7. J. Bigeleisen, J. Chem. Phys. 34, 1485 (1961).

8. J. Bigeleisen and M. G. Mayer, J. Chem. Phys. 15, 261 (1947).

9. M. Wolfsberg, J. Chim. Phys. Phisicochim. Biol. 60, 15 (1963).

10. W. A. Van Hook, J. Chem. Phys. 44, 234 (1966).

11. J. Bigeleisen, C. B. Cragg, and M. Jeevanandam, J. Chem. Phys. 47, 4335 (1967).

12. J. Bigeleisen, S. V. Ribnikar, and W. A. Van Hook, J. Amer. Chem. Soc. 83, 2956 (1961).

13. J. Bigeleisen, S. V. Ribnikar, and W. A. Van Hook, J. Chem. Phys. 38, 489 (1963).

14. J. Bigeleisen, M. J. Stern, and W. A. Van Hook, J. Chem. Phys. 38, 497 (1963).

15. T. Ishida and J. Bigeleisen, J. Chem. Phys. 49, 5498 (1968).

16. J. Bigeleisen and S. V. Ribnikar, J. Chem. Phys. 35, 1297 (1961).

17. Y. Yato, M. W. Lee, and J. Bigeleisen, J. Chem. Phys. 63, 1555 (1975).

18. M. Benedict and T. H. Pigford, Nuclear Chemical Engineering, McGraw-Hill, New York, 1957.

19. H. Wieck and T. Ishida, ERDA Report No. COO-3127-11.

20. L. Borodinsky and T. Ishida, ERDA Report No. COO-3127-14.

21. I. Kiss, G. Jakli, and H. Illy, Acta. Chim. Hang. 47, 379 (1966).

22. L. Matus, I. Kiss, and J. Valyi Nagy, Kozp. Fiz. Kut. Int. Kozl. 10, 77 (1962).

23. H. G. East and H. Kuhn, J. Sci. Instrum. 23, 185 (1946).

24. E. W. Becker and O. Stehl, Z. Angew. Phys. 4, 20 (1952).

25. K. W. Lamers, Report UCRL-11218, Part I, 1964; P. R. Rony, Part II, 1965.

26. A. Eucken, Phys. Z. 10, 586 (1909); W. Nernst, Ann. Phys. 36, 395 (1911).

27. W. F. Giauque and C. J. Egan, J. Chem. Phys. 5, 45 (1937).

28. H. L. Johnston, J. T. Clarke, E. B. Rifkin, and E. C. Kerr, J. Amer. Chem. Soc. 72, 3933 (1950).

29. J. Bigeleisen and E. G. Roth, J. Chem. Phys. 35, 68 (1961).

30. Mass Spectral Data, Amer. Pet. Inst. Res. Project 44, Carnegie Institute of Tech., Pittsburgh, Pa., 1953.

31. Rossini, Selected Values of Physical and Thermodynamic Properties of Hydrocarbons.

32. J. Bigeleisen, J. Chem. Phys. 23, 2264 (1955).

33. B. J. Zwolinski, "Selected Values of Properties of Chemical Compounds", American Petroleum Institute of Research Project 44, Thermodynamics Research Center, Texas A&M University, College Station, Texas (1974).

34. A. V. Grosse, R. C. Wackher, and C. B. Linn, J. Chem. Phys. 44, 275 (1940).

35. E. B. Wilson, J. C. Decius, and P. Cross, Molecular Vibrations, McGraw-Hill, New York (1955).

36. J. M. Dowling, R. Gold, and A. G. Meister, J. Mol. Spectrosc. 1, 265 (1957).

37. J. M. Dowling, R. Gold, and A. G. Meister, J. Mol. Spectrosc. 2, 411 (1958).

38. F. A. Andersen, B. Bak, and S. Broderson, J. Chem. Phys. 24(5), 989 (1956).

39. L. E. Sutton, Interatomic Distances, Chemical Society Special Pub. No. 11, Chem. Society, London, 1958.

40. W. F. Edgell and L. Parts, J. Am. Chem. Soc. 78, 2358 (1956).

41. E. L. Pace, J. Chem. Phys. 18, 881 (1950).

42. J. W. Russell, C. D. Needham, and J. Overend, J. Chem. Phys. 45, 3383 (1966).

43. J. L. Duncan, D. C. McKean, and G. K. Speirs, Molecular Phys. 24(3), 553 (1972).

44. J. Pickworth and H. W. Thompson, Proc. Roy. Soc. London A222, 443 (1954).

45. C. diLauro and I. M. Mills, J. Mol. Spectrosc. 21, 386 (1963).

46. W. L. Smith and I. M. Mills, J. Mol. Spectrosc. 11, 11 (1963).

47. R. J. H. Clark, O. H. Ellestad and R. Escribano, Molecular Phys. 31(1), 65 (1976).

48. E. W. Jones, R. J. L. Popplewell, and H. W. Thompson, Proc. Roy. Soc. London A290, 490 (1966).

49. J. Blanchard, L. C. Brunel, and M. Peyron, Chem. Phys. Letters 14(4), 481 (1972).

50. J. H. Schachtschneider and R. G. Snyder, Spectrochim. Acta 19, 117 (1963).

51. A. J. Barnes, H. E. Hallam, J. D. R. Howells and G. F. Scrinsham, J. Chem. Soc., Far. Trans. II, 69(5), 738 (1973).

52. A. Popowicz and T. Ishida, Chem. Phys. Letters (accepted).